Computational fluid dynamics modelling of multi-phase flow transition in presence of solid particles.

ALAITA, D.A.

2021

CFD MODELLING OF MULTI-PHASE FLOW TRANSITION IN PRESENCE OF SOLID PARTICLES

DAVID AJIRIOGHENE ALAITA

PhD   2021

CFD MODELLING OF MULTI-PHASE FLOW TRANSITION IN PRESENCE OF SOLID PARTICLES

DAVID AJIRIOGHENE ALAITA

A thesis submitted in partial fulfilment of the

requirements of

Robert Gordon University

for the degree of Doctor of Philosophy

October 2021

ABSTRACT

Multi-phase flow is the type of flow common in the oil & gas industry as oil reservoirs contain mixtures of oil, gas and water with sand particles from sandstone reservoirs. Accurate design of oil & gas production equipment greatly depends on detailed understanding of this flow phenomena. Previously, multi-phase studies relied upon empirical correlation and mechanistic equations developed from experimental data, but these approaches have limitations because of limited experimental data and underlying simplified assumptions. Thus, these methods cannot be used for complex flow situations often encountered in mature oil & gas fields. Hence, the lack of scalability of the existing classical empirical correlations and mechanistic models has called for high fidelity modelling method.

In this research, a computational fluid dynamics (CFD) method is used to investigate gas-liquid and gas-liquid-solid multi-phase flow in vertical pipe. A hybrid model, the multi-fluid Euler-Euler and Euler-Euler-Euler model with interfacial area transport equation (IATE) were used to simulate the flow regime spectrum in a large diameter vertical pipe. The hybrid model could simulate the mean gas volume fractions and bubble size changes as a function of fluid rate. The predicted gas volume fractions were benchmarked against experimented data set and were in agreement. Changes in the gas flow rates were seen to generate flow transitions from bubble to annular flow which compared favourably with appropriate literature across the vertical flow regime spectrum.

However, sand particle inclusion in the flow scheme were seen to change the flow dynamics and the flow dynamics was greatly dependent on the particle concentration. Solid particle concentrations were seen as the major deposition influencer. The results of this research elucidate the regime transition in a three phase gas-liquid-solid flow scheme of as typical production well and is viable for well production optimisation and completion design in large diameter vertical pipes.

DEDICATION

I would like dedicate this thesis to God almighty who gave me life and strength to successfully complete this research.

And to my late mother, Mrs Beatrice Aziakpoawhowho Alaita, who passed unto Glory on the 21st of September 2020. I wish she had lived longer to see this stage of my life.

ACKNOWLEDGEMENTS

"It always seems impossible until it is done" – Nelson Mandela. But, it could not have been done without the sound academic support and encouragement given to me by the right people around me. I want to appreciate my principal supervisor, Dr. Mamdud Hossain for his educational and intellectual advice that saw me through the course of this research. And other supervisory team members, Dr Nadimul Faisal, Dr Gbenga Adeyemi, and Dr Sheikh Islam for their support. Dr Faisal was particularly inspirational to the completion of this work.

I also want to acknowledge the support from the school of engineering staff, the head of school, Professor Ian Steel, and the administrative team. I am also thankful to the IT support team who were always there to address all IT issues.

Finally, I appreciate the most important person in my life, my spouse, Mrs Blessing Eloho Alaita in whom I have received exceptional support through the high and low moments. I cannot imagine how this journey would have been completed without her in my life. And to my children, Kome, Joshua and Maro; I am truly grateful for their patience and understanding through out the period of this research.

Now, I am lifted higher by everyone of you! Thank you all and God bless.

David Ajirioghene Alaita

July 2021

CONTENTS

LIST OF FIGURES

LIST OF TABLES

LIST OF SYMBOLS

Greek Letters

λ Bulk viscosity

ρ Density

Θ Granular temperature

Notation

$\bar{\bar{\tau}}$ stress tensor

τ_p Particulate relaxation time

$\vec{F}$ Interphase force vector term, N

$\vec{F}_q$ External force

$\vec{n}_w$ Wall lubrication coefficient

$\vec{R}_{pq}$ Interaction force between phases p and q

A_i, X_p Interfacial Area Concentration

C_l lift coefficient

C_{vm} virtual mass coefficient

C_{wl} Wall lubrication coefficient

e coefficient of restitution

f drag function

F_D Drag Force

F_{int} Interphase momentum force

F_{vm}	Virtual mass force
g	Gravitational constant
g_0	Radial distribution function
I	Identity matrix
$k_{sl,ls}$	Momentum exchange coefficient
m	Mass
p	Pressure
R_e	Reynolds number
R_{es}	Reynolds number
v	velocity

Subscripts and Superscripts

g, l, s	gas, liquid, solid phase
int	Interface
$k,$	Phase
$lift$	Lift
m	Mixture
n	Number of phases
p	particulate (secondary) phase
q	continuous (primary) phase
td	Turbulent dispersion
vm	Virtual mass
wl	Wall lubrication

INTRODUCTION

1.1 Overview of Multi-phase Flow

Multi-phase flow is the flow of more than one fluid phase in a single flow stream. The term would refer to any flow of two or more phases. This type of flow is common in the petroleum industry as well as geothermal, nuclear energy, petrochemical and food & drink industries. Possible combination of phases are gas-liquid, gas-solid, liquid-solid and gas-liquid-solid flow. multi-phase flow takes place in condensers, and evaporators of cooling devices, distillation and extractive columns, reactors and pipelines in the petrochemical industries (Pietrzak et al., 2017). Hydrocarbon production involves the flow of gas, oil, water and solids emerging from the reservoir simultaneously. While multi-phase flow may have advantageous effect in the petrochemical and nuclear industries, it increases complexity in the oil & gas industries due to deposition of solids, erosion and increased pressure losses. Such problems are prominent with fluid flow from sandstone reservoirs, aged reservoir and deeper offshore exploration and production. This has led to various multi-phase flow challenges in the oil & gas industry. However, due to increasing demand for oil and gas, the petroleum industry is saddled with the responsibility to find solutions to the challenges of multi-phase flow that affect the current production efficiency.

Fluid flow system in the petroleum industry is complex and challenging due to inevitable sand production from most reservoirs. Brill et al. (1987) stated that the fluids involved are multi-phase mixtures whose phase behaviour is extremely complex. Typical oil & gas production and processing architectures are complex and contain deep vertical sections and long horizontal sections (Figure 1.1). The challenges of phase transitions in the piping system is one of the issues to combat in multi-phase flow in the petroleum

industry (Figure 1.2).
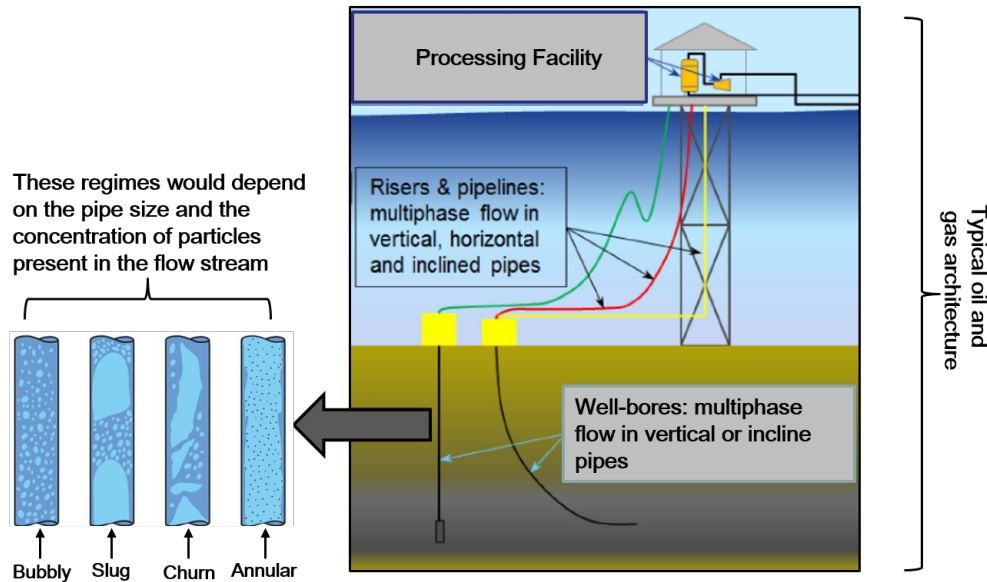
Figure 1.1: Typical Offshore Production Piping System (Adapted: Gharaibah et al. 2015)

Pioneering researchers (Hewitt and Roberts, 1969; Taitel et al., 1980) that studied the phase distribution of multi-phase flow had recognised different flow configurations (Figure 1.2). At the early prolific era, wells were capable of flowing at high rate, hence homogeneity assumptions were used to describe the mixture. The mixture pressure balance formulation was used to evaluate pressure drops in vertical wells (Duns Jr et al., 1963; Hagedorn et al., 1965; Orkiszewski et al., 1967; Aziz et al., 1972; Beggs et al., 1973). However, this was only convenient due to the homogeneity of the flow stream (Brill et al., 1987) which sees the gas and liquid flowing at the same velocity due to high rate of flow. But as the prolific reservoirs began to deplete, slip conditions which created complexities of different phase configurations (flow pattern) became prominent. The description of these flow patterns was clouded with subjectivity, measurement technique and the environmental condition of the experimental set up. Nonetheless, most school of thoughts agreed to the most acceptable flow patterns which are bubbly, slug, churn and annular flows. These configurations are depicted in Figure 1.2.
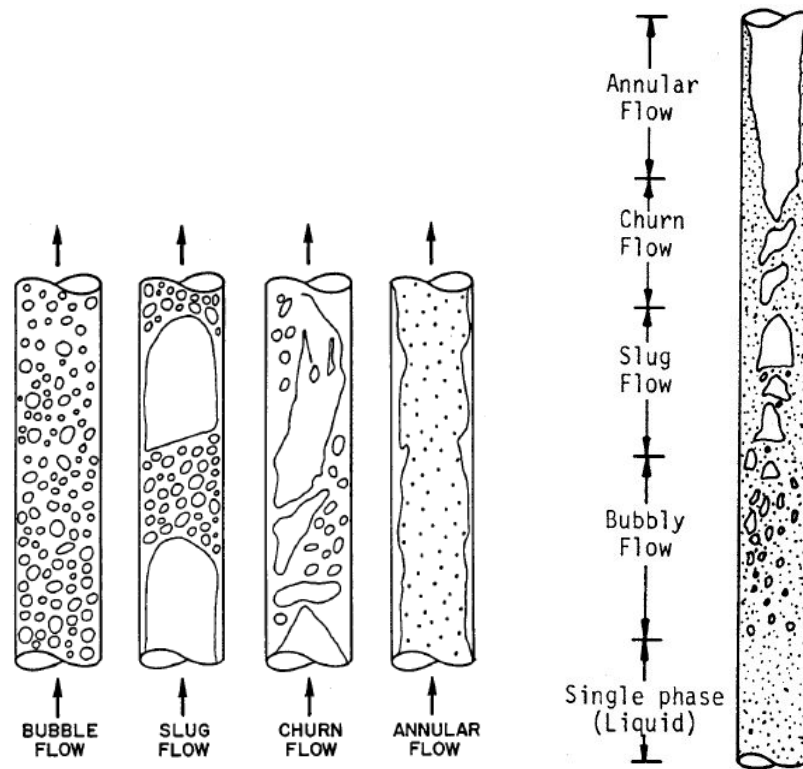
(a) Vertical flow (Brill 1987)

(b) vertical flow (Hassan & Kabir 1988)

Figure 1.2: Flow Regimes in Vertical Pipe

1.2 Challenges of Multi-phase Flow in Pipelines

According to the Oil & Gas Authority 2019/2020 overview, the UK government forecast shows that oil and gas will remain an important part of our energy mix for the foreseeable future and maximising economic recovery is still vital to meet our energy demands. The demand for energy to support the growing population and the current energy need of consumer industries will continue to increase. As the prolific reservoirs deplete and exploration & production moves to the marginal and deeper reservoirs, the dynamics of the challenges in the petroleum industry increased. Slip phenomenon and particle production from depleted sandstone reservoirs become pronounced. Therefore, previous correlations and mechanistic models developed are incapable to accurately predict flow regimes transitions and subsequent pressure drop due to sand production (Adeyanju et al., 2012). This is because past investigators did not considered the impact of sand particle in the flow pattern transition and pressure drop calculations done or estimated with

those correlations did not account for the impact of sand particles in the hydrodynamics parameters.

In the past five decades, researchers have carried out various studies, both analytical and experimental to understand multi-phase flow hydrodynamic changes. The complexity of resolving the interface forces and momentum transfer terms have led researchers to develop mechanistic models to predict multi-phase flow hydrodynamic parameters. However, these approaches could not yield conclusive and exhaustive results due to wide range of flow conditions and the complex interaction of the phases. Some correlations produced error margins of up to average of 20 percent (Brill 1987, Ruiz e tal 2014). Predicting multi-phase flow hydrodynamics in an oil and gas production system are further complicated by complex heat transfer that occurs as fluids flow through the piping system and the mass transfer that takes place within the hydrocarbon fluids due to changes in pressure and temperature. These phenomena are governed by conservation of mass, momentum and energy, coupled with fundamental thermodynamics and heat transfer (Brill et al., 2010).

The complication in the oil & gas production is further aggravated due to long vertical sections in the piping system of a typical offshore production from deeper reservoirs. Produced hydrocarbon fluids that contain mixtures of liquid-phase (oil & water), vapour phase natural gas and sand particles need to be transported efficiently from the wellbore to the process facility. Such typical offshore architecture is shown in Figure 1.1. Further complexity arises from the fact that the flow regime transitions can occur spanning all flow patterns in the single pipe before the fluid gets to the production platform (Figure 1.2b). Flow structure configuration also depends on the transporting pipe shape, size and orientations as well as the flow parameters, material properties and phase fractions (Jayanti and Hewitt, 1992a; Ohnuki and Akimoto, 2000; Omebere-Iyari et al., 2007a,b; Gharaibah et al., 2015).

According to Johansen et al. (2015), these flow regime transitions cannot be properly accounted for with the existing correlations and mechanistic models. Johansen et al. (2015) further stated that the dynamic evolution of mean bubble (and drop) sizes is an important process that influences the evolution of flow regimes and their transitions in a vertical pipe. Another complexity of three-phase flow is the effect of fine particles and

surfactant that could affect the interface merging and coalescence which may, in some cases significantly change the flow regime, phase slip and pressure drop (Johansen et al., 2015). Besides, Lakehal (2013), and Gharaibah et al. (2015) asserted that the complexity of multi-phase flow in vertical pipe increases with the presence of sand particles.

In addition, due to the increased demand for energy from the nuclear and oil & gas industries, the necessity to migrate toward larger diameter pipes for development became essential (Ali Farman and Yeung, 2015). However, researchers in the past (Jayanti and Hewitt, 1992a; Taitel et al., 1980) had used smaller diameter pipe of up to 75mm in their experiments and had recognised four flow patterns and the results from such small diameter pipes have been extrapolated for large pipe design. Although Ali Farman and Yeung (2015) stated that such extrapolations result in significant errors because of the complexity arising from the interaction of the phases. This has resulted in lack of detailed knowledge of the flow behaviour in large diameter vertical pipes. Recent experimental work carried out in larger diameter pipes by Ohnuki and Akimoto (2000), Omebere-Iyari et al. (2007b), Ali and Yeung (2014b) and others proved that the flow patterns encounter in large diameter pipe are different from those encountered in small diameter pipe by previous researchers. In particular, slug flow is not seen in large diameter pipe flow. Besides, the phase distribution mechanism in larger diameter pipe is expected to be different from that of smaller round diameter pipe (Shen et al., 2004, 2005).

While the application of tools and correlation for large diameter pipes are different from small diameter pipes, it will be inaccurate to upscale models and correlations developed for small pipe flow to be used for design and analysis of larger diameter pipe. Moreover, these models developed for small diameter pipes did not include sand particles in the first instance. Whereas a typical multi-phase flow in the oil & gas sector would contain gas-liquid-solid flows in the flow stream. Therefore, detailed multi-dimensional models for three phase gas-liquid-solid flow are needed to understand the complex flow dynamics that occurs in vertical large diameter pipes. (Johansen et al., 2015).

1.3 Multi-phase Flow Modelling Techniques

In search of development tools to assist engineers in predicting multi-phase flow behaviours in piping systems, researchers have developed models to predict the interactions between the different phases in the flow stream (Brill et al., 2010). The first attempt to study multi-phase flow was through theoretical analysis developed by Versluys et al. (1930), but no solutions was found to correlate all the various factors involved to fit the wider scenarios. This was followed by semi empirical approach developed by Poettman et al. (1952) using the energy balance equation but it was only applicable to low flow rate wells at the time. The complexity of the energy balance equation at the time was due to lack of means to know the energy exchange between the phases. Hence the simplified version of the equation was used for prediction but, this was limited to smaller diameter pipes. Due to the complexity of these equations and its unfitness for practical application, simplified pressure gradient curves were developed by Gilbert et al. (1954) from empirical data to predict the pressure drop in vertical wells. However, such pressure gradient curves were also of limited application within the parameters and field data used. The following subsections describe the available methods applied for the investigation of multi-phase flow hydrodynamic parameters.

1.3.1 Homogeneous Mixture Model

In the early days of oil & gas production, most wells had high rate flow with high turbulence and all the phases were transported at the same velocity. The flow field at the time was homogeneous with no slip between the gas and liquid phase. Researchers such as Fancher Jr et al. (1962) and Baxendell et al. (1961), developed the pressure balance equation from Poettman et al. (1952) correlation using the homogeneous mixture model. This was based on no-slip phenomenon where the gas and oil were assumed to be moving with the same velocity. Such pressure balance analysis of multi-phase flow consists of the static gradient, the wall friction gradient and the acceleration gradient. Although, the acceleration pressure gradient was omitted by both authors and Poettman et al. (1952) computation because it was thought to be insignificant. However, the prolific era of

homogeneity did not last long and were soon over which left researchers grasping for new solutions to multi-phase flow analysis. This gave rise to new approaches to multi-phase flow modelling.

1.3.2 Empirical Correlations

At some time, the homogeneous mixture model was no longer fit for purpose. Researchers used a pool of larger experimental data to developed empirical relationship to predict the flow dynamics. The introduction of slippage to the flow stream led to the geometrical arrangement of the phases which in turn led to different flow patterns as shown in Figure 1.2. Duns Jr et al. (1963) developed the first ever dimensional analysis of multi-phase flow from large pool of experimental data. However, empirical correlations do not represent the physics of the flow mechanism but do give accurate result, nonetheless. But the method is also limited to the data set and conditions used and cannot be upscaled for different parametric study. This is the major setback of empirical correlations.

1.3.3 Mechanistic Models

The complexity of multi-phase flow arises from the slippage where the gas and liquid flow with different velocities thereby, creating spatial geometrical configurations in the flow conduit. A mechanistic modelling is the means to mathematically model the physical mechanism governing the multi-phase flow behaviour in the conduit (Brill et al., 1987). To develop a mechanistic model, a pre-knowledge of the flow pattern is a prerequisite requirement to the modelling in order to capture the fundamental mechanism of the flow. Mechanistic model incorporates the effect of the operational parameters, geometrical parameters and the physical properties of the fluids. Thus, the mechanistic model is expected to be more reliable for wider range of flow conditions such as flow rates, pipe diameter and fluid properties (Shoham, 2005). However, because multi-phase flow in pipe is transitional along the pipe (Figure 1.2b), it is not possible to capture such transitions with mechanistic models where the pre-knowledge of the flow pattern is not available. Therefore, a new approach such as numerical simulation using computational fluid dynamics (CFD) method is required.

1.3.4 Numerical Simulation Model

One of the shortcomings of the mechanistic modelling method is the need to have the pre-knowledge of the flow patterns before the model is developed. A numerical modelling approach solves the energy balance equations without prior knowledge of the flow patterns and produces reliable prediction of the hydrodynamic variables and energy loss, unlike the mechanistic modelling method. CFD simulation of multi-phase flow from fundamental governing equations and physics have received wide acceptance as the technique needed to understand the complex flow phenomena of multi-phase flow. CFD is the science of predicting fluid flow, heat and mass transfer, chemical reactions and related phenomena by numerically solving the sets of governing mathematical equations of the conservation of mass, momentum and energy with the constitutive equations of the turbulence parameters and the interfacial transfer terms. In this research, CFD methodology is applied to investigate the multi-phase flow of gas-liquid and gas-liquid-solids flow through a large diameter pipe.

1.4 Research Aim and Objectives

Based on the foregoing introduction and shortcomings in the works done by researchers in the past four decades in the field of multi-phase flow, this research is designed to investigate the issues of multi-phase flow in the current scenario. The aim and objectives of this research are as follows:

1.4.1 Research Aim

The aim of this research is to investigate and predict the gas-liquid and gas-liquid-solid flow hydrodynamics and flow pattern transitions with the effect of solid particles in the flow field in a large diameter vertical pipe using computational fluid dynamics method.

1.4.2 Research Objectives

In order to achieve the aim of this research, the following objectives are to be met:

1. Investigate the flow dynamics of gas-liquid flow scheme in a large diameter vertical pipe using a CFD approach in the Eulerian framework in order to establish flow pattern transitions of two-phase flows in large diameter pipes.

2. Investigate the impact of solid concentration in a three-phase gas-liquid-solid flow using CFD method, in order to establish the flow dynamics in three-phase flow.

3. Investigate the variables responsible for sand transportation and deposition phenomenon in large diameter vertical pipe in order to establish the effects of sand concentrations on the sand carrying capacity in large diameter pipes.

1.5   Outline of Thesis

The presentation of the work of this research is structured coherently and explicitly into the following chapters:

chapter 1 presents the overview of multi-phase flow in an oil & gas installations. It includes the challenges and different modelling techniques that has been adopted in the past to tackle these challenges. Also included are the reasons why it is now time to change the modelling technique to CFD computations and the advantages of this approach.

chapter 2 reviews and acknowledges the works of past researchers with the objective of establishing the gap in knowledge and the technologies that have not been fully utilised. The discrepancies between small and large diameter pipes are discussed. The limitations of the current database for large diameter and three-phase gas-liquid-solid flow are also made bare.

chapter 3 discusses the available CFD techniques, models and formulations that are applicable to two-phase flow and three-phase flow simulations.

chapter 4 deals with the solution technique adopted for this investigation. It includes the validation of the models used for the two-phase and three-phase computation with experimental data sets.

chapter 5 presents CFD computation of two-phase gas-liquid and validation. It also includes the analysis of the results and investigation of changes in the field variables applicable to production system analysis in the oil & gas industry.

chapter 6 presents the three-phase flow investigated in this research. It includes the validation, qualitative and quantitative analysis of the impact of sand particles on the hydrodynamic of gas-liquid-solid flow scheme. Also included in this chapter are the sand transportation and deposition studies in the pipe bore. The study considers three cases of sand concentration inflows into the flow field and the impact of these variabilities.

chapter 7 provides the overall conclusion and recommendation of this research. The aims and objectives, the novelty of the outcome of the research work and look ahead are also discussed.

References presents all the citations and references where relevant information was taken for educational, informative and experimental validation of the CFD results.

LITERATURE REVIEW

2.1 Overview

The quest for energy requirements to sustain the ever increasing demand for more energy has been very challenging due to inherent multi-phase flow problems mainly resulting from sandstone reservoir depletion, exploration and production from deeper wells in harsh environment. Over the years, researchers in the petroleum industry have dedicated ample time and resources in trying to understand multi-phase flow behaviours and to provide suitable correlations and models for efficient pipeline design and production operations. Initial approach to understand multi-phase flow hydrodynamics were through experimental observations and empirical correlations. Further on, the modelling approach was used to develop mechanistic models that better represent the multi-phase flow dynamics. However, there were still unresolved uncertainties in the outcome of modelling results due to the complexities of interface exchange between the phases. Besides, empirical corrections are not suitable for wide range outside the experimental conditions in which they were developed. In addition, most of these models do assume two-phase flow, but the oil & gas industry flow stream is typically of three-phase gas-liquid-solid flows.

There are basically two set of experimental data available in literature from the study of multi-phase flow in vertical pipe, one of small diameter and other of large diameter pipes. The small and large diameter pipes delineation is explicitly shown in section 2.5 using the widely validated dimensionless pipe diameter correlation developed by Kataoka and Ishii (1987). The generically accepted flow patterns in vertical pipe, namely: bubble, slug, churn and annular flow were developed from the understanding of inhomogeneous

two-phase flow experimental works in small diameter pipes. Empirical correlations were thus developed from these experiments for the prediction of flow dynamics in two-phase flow. However, these correlations were only applicable to flow conditions considered in the experiments. In order to understand the flow mechanism in multi-phase flow that covers larger scale of reference, researchers such as Orkiszewski et al. (1967), Chierici et al. (1974), Aziz et al. (1972), Asheim et al. (1986) and Hasan et al. (1988) developed mechanistic models for various flow conditions following the work of Griffith and Wallis (1961) and Nicklin and Davidson (1962). Although, mechanistic models (unlike general empirical correlations) are capable of predicting complex physical phenomenon occurring in multi-phase flow and provide significant results that represent significant improvement, there is the need to first predict the flow pattern and after then can the model predict the liquid holdup, interfacial stresses and pressure drop (Brill et al., 1987).

Lawson et al. (1974) performed statistical evaluation of correlations used to predict pressure losses in multi-phase flow in vertical oilwell tubing and concluded that these methods are highly empirical and their validity are limited to the quality and scope of the data upon which they are based. Subsequently, Cox et al. (2006) Olufemi et al. (2011), Adeyanju et al. (2012) and Ruiz et al. (2014) performed similar analysis on the accuracy of multi-phase flow correlation as applied to field and production analysis and completion strategy. These authors also concluded that most of the predictions were only accurate subject to the flow conditions upon which the correlations were derived. The authors claimed that there are no universal correlations that fit all flow scenarios. The foregoing confirmed the assertion by Hagedorn et al. (1965) who postulated that a solution to the understanding of multi-phase flow hydrodynamics would be the approach normally used in classical fluid dynamics based on the formulation and solution of the Navier-Stokes equation. But this would only be possible if the non-linearity involved and the difficulty of adequately describing the boundary conditions is resolved. However, this was not possible at the time.

Neither the empirical correlations nor the mechanistic models developed by prominent researchers considered the third phase solid particles which accompany oil and gas flow from sandstone reservoirs. Understanding multi-phase flow dynamics in this context would be different from the standard two-phase gas-liquid flow stream. The presence of sand

in the system could affect the flow patterns and energy loss. In such cases, detailed multi-dimensional models are needed to understand the complex flow dynamics (Johansen et al., 2015).

Researchers in other related field such as chemical and process industries have carried out extensive work in the study of the gas-liquid-solid flow hydrodynamics using experimental and computational fluid dynamics (CFD) approach. Among others, Rampure et al. (2003) performed experimental and CFD investigations of gas-liquid-solid flow in a 200mm vertical bubble column. Also, Li and Zhong (2015) performed CFD computation to investigate three phase gas-solid-liquid flows in a 200mm, 150mm and 100mm vertical bubble columns. The authors extended the range of the gas superficial velocities above the bubbly flow up to churn-turbulent flows. This knowledge can be applied directly to the petroleum industry. This is presently the new frontier in understanding multi-phase flow hydrodynamics. CFD methodology is accurately able to compute the interfacial transfer terms in order to predict the hydrodynamics of multi-phase flow.

2.2 Multi-phase Flow in Vertical Pipe

Multi-phase flow is the combination of two or more phases flowing together in the same flow stream. This could be categorised as either gas-liquid, liquid-liquid, gas-solid, liquid-solid or gas-liquid-solid flows. In the oil & gas industry, these phases could be natural gas with sand particles or oil with sand particles or oil with water, or gas-oil-sand. Generally, most researchers had just settled for two-phase gas-liquid when referring to multi-phase flow and had limited their multi-phase flow experiment to just gas-liquid. Therefore, their flow pattern identification was carried out in this respect.

Hewitt (2012) stated that gas-liquid two-phase flow is the most complex to understand partly because of the compressibility and the deformable interface between the phases. It is interesting to know that there are large numbers of experimental and mechanistic studies carried out on two-phase flow. It has been established that the traditional two phase flow system exhibits four main flow patterns which are bubbly, slug, churn and annular flow (Hewitt and Roberts, 1969; Taitel et al., 1980; Taitel, 1986; Costigan and

Whalley, 1997). In 1969, Hewitt and Roberts performed an experiment to determine the two-phase flow regimes in a 38mm diameter vertical pipe. The authors used the simultaneous x-ray and flash photography method to capture the flow pattern. In the same vein, Taitel et al. (1980) carried experimental study of two-phase flow in vertical pipe in order to understand flow pattern development and transitions. Further attempts to accurately describe the flow regimes in vertical pipe was carried out by Costigan and Whalley (1997) using conductivity probe to measure the dynamic variation of the void fractions of air-water flow in a vertical pipe. The authors identified six flow regimes in the process. It is worthwhile to know that there has been lots of variations in the outcome of experimental results due to measurement mechanism and individual subjectivity in the interpretation of results. While most of the past studies were done with clean two-phase gas-liquid flow mixture in small diameter pipes, it is generally accepted that four main flow patterns are present in vertical pipe and these are bubbly, slug, churn and annular flow regimes.

However, there are other school of experimental researchers that had experimented in large diameter pipe and postulated that the traditional slug flow is not present in large diameter vertical pipes. They believed that the application of modelling tools/correlation based on small diameter pipes in predicting flow behaviour (flow pattern, void fraction and pressure gradient) in large diameter pipes poses severe challenges in terms of accuracy due to lack of detailed understanding of the flow mechanism on large diameter pipes (Kataoka and Ishii, 1987; Ali Farman and Yeung, 2015; Pagan et al., 2016a). Hence the distinction between small and large diameter pipes has been a subject that has evolved because the geometric distribution of the phases and flow structures are different in small and large diameter pipes (Schlegel et al., 2012, 2016).

When the hydraulic diameter of a two-phase flow channel reaches a certain size, slug bubbles bridging the entire diameter can no longer be sustained due to Raleigh-Taylor instability. This interaction of the two types of instability results in large bubbles being broken into many smaller cap-shaped bubbles. This causes many changes to the hydrodynamics of the flow, thus producing additional turbulence due to bubble drag, enhancing turbulent diffusion, and producing strong secondary re-circulations in the flow. These changes result in very different physical mechanisms behind the transport of gas

and liquid. This means that models typically applied to flows in small-diameter pipes can no longer be guaranteed to predict flows in large-diameter channels accurately (Kataoka and Ishii, 1987; Hibiki and Ishii, 2003). The critical diameter at which this transition occurs is defined by the formulation in Equation 2.1, which was initially developed by Kataoka and Ishii (1987).

$$D_H^* = \frac{D_H}{\sqrt{\frac{\sigma}{g\Delta\rho}}} \geq 40 \qquad (2.1)$$

where, D_H^* is the dimensionless pipe diameter, D_H is the pipe diameter, σ s the surface tension, $\Delta\rho$ is the density difference and g is the acceleration due to gravity. Therefore, new experimental data and correlations should be obtained for analysis of systems that include flow channels of large diameter pipes.

Recently, researchers such as, Ohnuki and Akimoto (2000), Oddie et al. (2003), Sun et al. (2003), Omebere-Iyari et al. (2007a), Prasser et al. (2007), Schlegel et al. (2009), Kaji and Azzopardi (2010), Smith et al. (2012), Ali Farman and Yeung (2015), Pagan et al. (2016b), have studied two-phase gas-liquid flows in large diameter pipes and had discovered different flow patterns in comparison to small diameter pipes. Although the

(a) Ohnuki & Akimoto (2000) flow map

(b) Omebere-Iyari etal (2007b) flow map
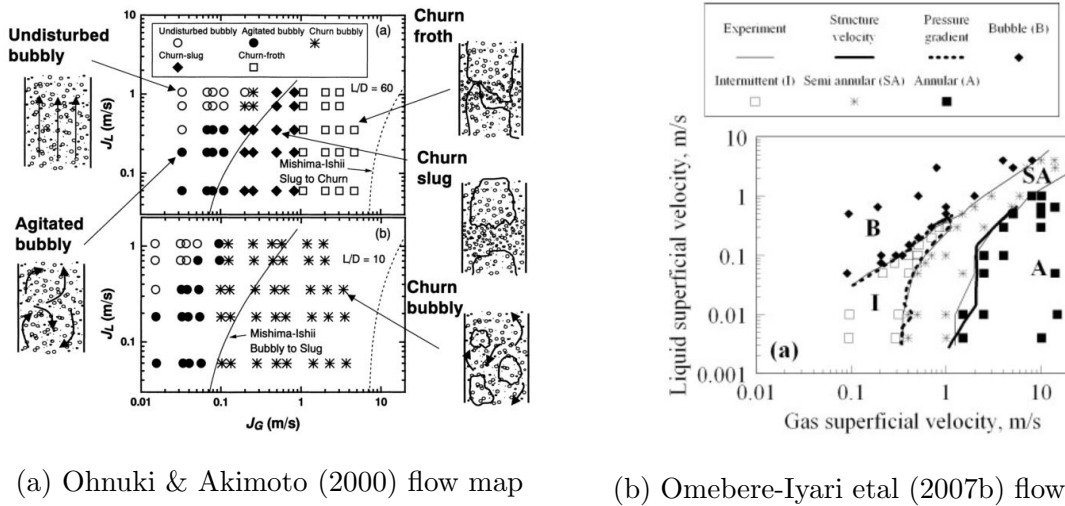
Figure 2.1: Flow Maps From Large Diameter Pipes

general conclusion by these researchers is that slug flow is not found with a two-phase gas-liquid flow in large diameter pipe however investigations of the flow dynamics of multi-phase flow in large diameter pipe so far did not include solid particles in the flow stream. Therefore, the extent to which solid particles would affect the key hydrodynamic

(a) Taitel etal (1980) flow map

(b) Hewitt and Robert (1969) flow map
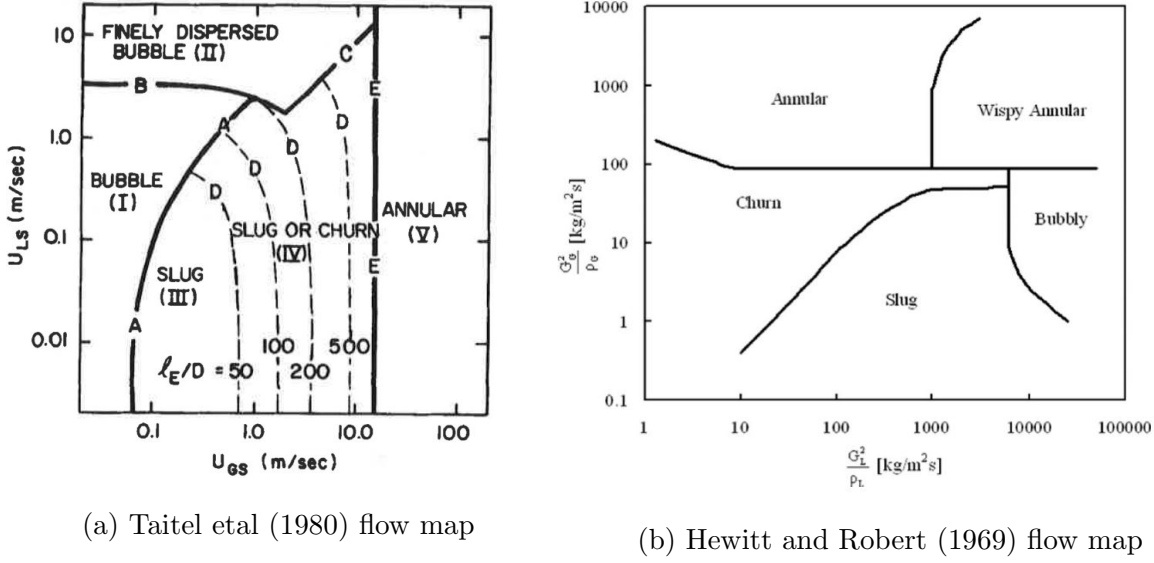
Figure 2.2: Flow Maps in Small Diameter Vertical Pipe

parameters has not yet been determined. On the other hand, Jayanti and Hewitt (1992b) had earlier stated that experimental studies are marred with subjectivities and accuracy of the measuring instrument to capture the flow mechanism to a sufficient degree of sophistication. Hence interpretation of the flow pattern identified by different researchers for various flow pattern classification for larger diameter pipes are still not consistent but bears little resemblance.

According to Pietrzak et al. (2017), an important aspect of the hydrodynamics of multi-phase flows system performance is connected with adequate identification of flow regime and the ability to accurately predict void fractions and pressure drop. This is important for the proper design, operation and scale-up of pressure management and fluid handling systems in a wide range of industrial processes (Wu et al., 2017). Over the years, lots of experimental data and theoretical models generated thereof are available for prediction of different flow regimes but, mostly applicable to small diameter pipes (Figure 2.2a and Figure 2.2b).

Because of the importance of flow patterns and regime transitions, researchers have used different types of identification techniques for the delineation of the flow configuration in addition to visual classification. The critical parameter needed for the identification of flow pattern is the gas volume fractions or gas hold-up, pressure differential and structure velocity. Jones Jr and Zuber (1975a) used the probability density function (PDF) of the

statistical gas volume fraction as a quantitative flow pattern discriminator to identify flow patterns. The authors also used spectral density function to show the inherent discreteness of the flow field. Costigan and Whalley (1997) used the same method to classify flow regimes into their respective patterns, while other researchers like Matsui (1984) and Tutu (1982) used differential pressure fluctuations for flow pattern recognition in vertical two-phase gas-liquid flows. On the other hand, researchers such as Cai et al. (1994), Mi et al. (1998, 2001) and Lee et al. (2008) used neural network for the identification of flow patterns. Cheng et al. (2008) stated that the physical mechanism controlling pressure drop is intrinsically linked to local flow pattern, hence flow pattern identification and classification is very important in the process industries.

Due to the variability and subjectivity involved in the two-phase flow experiment and regime characterisation, there has been various flow pattern groupings by different school of thoughts. While churn flow and wispy annular flow are the least studied flow regimes (Parsi et al., 2014), it was discovered in an experiment carried out by Ohnuki and Akimoto (2000) and Omebere-Iyari et al. (2007a), that churn flow is the dominant flow pattern discovered in large diameter pipe. Database regarding such large diameter pipe multi-phase flow are sparse hence, more study is required to ascertain the flow transitions in large diameter pipe (Figure 2.1). Nonetheless, for both flows in small and large diameter pipe flow mentioned earlier, the impact of the presence of sand particles on the flow hydrodynamics or the development of the flow pattern are rarely mentioned. If the flow pattern is as important as earlier stated, then there should be the need to consider what might alter the global flow regime in any flow stream. Most importantly, in an oil and gas flow system, the fluid system can rarely be referred to as clean fluid, hence it is important to determine if the same methodology is still accurate in the presence of sand particles. Some of the methods used by researchers to extract flow variables in two phase flow system are:

- Linearised X-ray system.

- Neutron radiography & image processing.

- Gamma ray system.

- Quick closing valves.

- Electrical impedance tomography.

- Electrical resistivity tomography.

Although, it is not the intent of this study to compare different methods, it is important to note that efficiency and accuracy of any methodology adopted to extract local gas volume fractions inherently depends on the fluid physical and thermophysical properties such as density, viscosity, conductivity and resistivity and other properties. Reports have shown that the configuration of the instrumentation could influence the result of the experiment (Ghosh et al., 2012). Hence, it is necessary that accurate fluid flow modelling should be devoid of any human and environmental interference, and all parameters should comply with simple laws of mass and momentum transfer.

2.3 Two-Phase Flow in Large Diameter Pipe

The focus of this thesis is on large diameter pipes, classed as sizes between 100-500mm. It is reported that most of the experimental studies carried out so far are in small diameter pipes (10-100mm). Review of the publications by Wu et al. (2017) shows that the literatures in large diameter pipe are scarce. In addition, most of the experimenters had to use air-water and steam-water combination for safety and convenience. Omebere-Iyari et al. (2007a) has shown that under the same flow conditions, the gas volume fractions are comparatively higher in a petroleum gas-oil fluid system than in an air-water two-phase flow system. The authors also shown that there is disparity in the drift velocity which can be linked to the different phase distribution profiles for steam-water and nitrogen-naphtha flow. Oddie et al. (2003) performed an experiment in a 150mm pipe using nitrogen-oil and nitrogen-tap water flows while Schlegel et al. (2009) and Smith et al. (2012) performed their experiments in a 150mm diameter pipe using air-water flow. The striking similarity to note is that these authors did not observe slug flows in any of the large diameter pipe in their cases.

Earlier on, Ohnuki and Akimoto (1996) investigated the flow structure in an air-water two phase flow system in a 480mm diameter vertical pipe with gas superficial velocity of

0.01-0.87m/s and water superficial velocity of 0.01-0.2m/s; the range at which slug flow should have been observed in a smaller diameter pipe, but found no slug flow regime. In a similar experiment, Ohnuki and Akimoto (2000) conducted investigation of two-phase gas-liquid flow in a 200mm diameter vertical pipe and found no slug flow. Similarly, Cheng et al. (1998) investigated the structure of upwards air-water flow in a vertical 150mm diameter pipe and concluded that there is no abrupt transition from bubbly to slug flow but, rather from bubbly to churn flow. Other researchers such as Sun et al. (2003), Omebere-Iyari et al. (2007b) and Ali and Yeung (2014b) also did not observe slug flow pattern in their experiments. The classification of large diameter pipes depend on the geometry and the inherent properties of the fluid system. Evaluating the dimensionless pipe diameters using the formulation given in Equation (2.1), the results depicted in Table 2.1 shows the delineation of small to large diameter pipes for different fluids systems. In this regard, pipes that can sustain large Taylor bubbles in an air-water flow field leading to slug flow will be different in an oil-gas flow field.

Table 2.1: Dimensionless Pipe Diameter Characterisation

Pipe Diameter		DH*			
DH (in)	DH (mm)	Air-Water	Gas-Oil	N_2-Naphtha	N_2-naphtha
7.4	189	70	123	113	121
5.9	150	55	97	90	96
4.7	120	44	78	72	77
4.3	110	41	71	66	71
3.9	100	37	65	60	64
3.5	90	33	58	54	58
3.1	**80**	**29**	**52**	**48**	**51**
2.8	70	26	45	42	45
2.4	60	22	39	36	39
2.0	50	18	32	30	32

Equation (2.1) has been tested by various researchers such as Smith et al. (2012); Schlegel et al. (2009) and has been validated and used to generate data set shown in

Table 2.1. As could be deduced from the table, accurate and representative modelling of multi-phase flow would depend on using a representative fluid system. Comparing the experimental results from different fluid system with steam-water and nitrogen-naphtha, Omebere-Iyari et al. (2008) showed that the gas volume fractions of an equivalent gas-oil system is comparatively higher than that of steam-water system. Only Hills (1976) has reported slug flow in a 150mm diameter pipe which may be due to measurement technique and subjectivity in interpreting the results. In summary, there seems to be reasonable agreements by researchers on the conclusion of two-phase flow in large diameter pipes, except for Hills (1976), that slug flow is inherently absent in large diameter vertical pipe flow. However, the investigations so far carried out did not include sand particles. There is need therefore to fully investigate multi-phase flow in large diameter vertical pipe with solid particles in order to develop relevant relationship and models for designs and optimisation of vertical piping systems.

2.4 Flow Regime Transitions

Most of the flow regimes studies carried out so far are based on experimental settings and empiricism. However, empirical flow regime transition has been the most disputed flow pattern specification because delineation by visualisation is subject to errors and human skills. This has led to considerable disagreement among researchers on the mechanism of flow transition. Better understanding of the physical mechanism under which transition occurs is needed (Taitel et al., 1980). The critical parameter for regime identification is the gas volume fraction, commonly called void fraction. Because flow patterns in small and large diameter pipes are different, models developed for small diameter pipes may be different from those of large diameter pipes.

There are many mechanistic models presented in literature but, only the best known will be mentioned in this thesis for understanding. In a critical review of literature carried out by Wu et al. (2017), the authors concluded that the most reliable flow regime transition models are: Barnea (1987) for disperse bubble to bubble and from slug to churn flow; Taitel et al. (1980) for bubble to slug and Mishima and Ishii (1984) for churn to annular flow. These models were originally developed for small diameter gas-liquid flows but,

may be unsuitable for flows with sand and in large diameter flow system where the flow structures and void fraction evolution are different. The following sections examine the flow regime transitions for various flow patterns.

2.4.1 Bubbly to Slug Flow Transition

Taitel et al. (1980) showed that the critical gas volume fraction for transition from bubbly to slug flow is 0.25 while Mishima and Ishii (1984) suggested 0.3 as the transition criteria for bubbly to slug flow. If U_G is the gas bubble rise velocity, α is the gas volume fraction, U_L is the liquid velocity, U_{GS} and U_{LS} are the superficial velocities of the fluid, then:

$$U_G = \frac{U_{GS}}{\alpha} \tag{2.2}$$

and

$$U_L = \frac{U_{LS}}{1 - \alpha} \tag{2.3}$$

The rise velocity, U_o of relatively large bubbles (Harmathy (1960)) is shown in Equation 2.4

$$U_o = 1.53 \left[\frac{g(\rho_L - \rho_G)\sigma}{(\rho_L)^2} \right]^{1/4} \tag{2.4}$$

if $\alpha = 0.25$, then from equation 2.2 and 2.3,

$$U_{LS} = U_{GS}\frac{1 - \alpha}{\alpha} - (1 - \alpha)U_o \tag{2.5}$$

$$= 3.0U_{GS} - 1.15 \left[\frac{g(\rho_L - \rho_G)\sigma}{(\rho_L)^2} \right]^{1/4} \tag{2.6}$$

Once the fluid properties are known, the theoretical transition curve can be plotted on U_{LS} vs U_{GS} co-ordinates and will remain invariant of the tube sizes (Taitel et al., 1980).

On the other hand, Mishima and Ishii (1984) used gas volume fraction criteria of 0.3 with the drift velocity to develop the theoretical correlations depicted in Equation 2.7.

$$U_{LS} = \left(\frac{3.33}{C_o} - 1 \right) U_{GS} - \frac{0.76}{C_o} \left[\frac{g(\rho_L - \rho_G)\sigma}{(\rho_L)^2} \right]^{1/4} \tag{2.7}$$

where for round tube,

$$C_o = 1.2 - 0.2\sqrt{\frac{\rho_G}{\rho L}} \tag{2.8}$$

The difference between dispersed bubble and bubble flow were not completely agreed on by Taitel et al. (1980) and Mishima and Ishii (1984). The latter did not consider

dispersed bubble flow as a separate regime. While Taitel et al. (1980) suggested that at high liquid flow rate, turbulent forces tend to break and dispersed the gas phase into smaller bubbles that give rise to disperse bubbles in the flow stream.

2.4.2 Slug to Churn Flow Transition

Typical slug and churn flow are shown in Figure 1.2. Earlier, Nicklin and Davidson (1962) attributed churning to flooding by the falling liquid film around the Taylor bubbles. The authors defined the velocity of the Taylor bubbles by the formulation in Equation 2.9.

$$U_T = 1.2 U_M = 0.35 \left[\frac{gD \bigtriangleup \rho}{\rho_L} \right]^{1/2} \tag{2.9}$$

where U_T is the translational velocity of the Taylor bubble. Later on, Taitel et al. (1980)
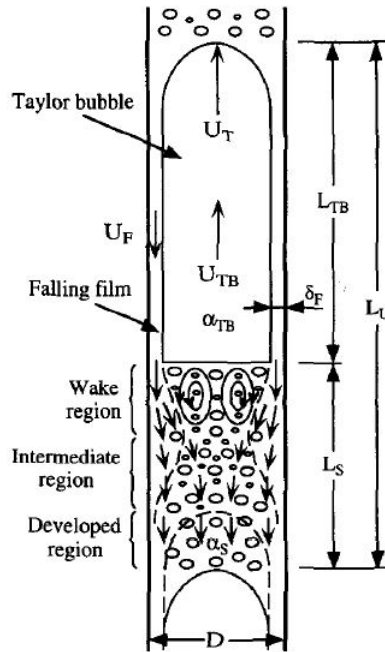
Figure 2.3: Transition from Slug Flow to Churn fFow (Chen and Brill 1997)

described churn flow as an entrance related phenomenon associated with the existence of the slug flow further along the pipe. The authors stated that the critical gas volume fraction at which this transition occurs is 0.25. The author defined the entrance length after which stable slug flow can be formed by Equation 2.10.

$$\frac{L_E}{D} = 40.6 \left(\frac{U_m}{\sqrt{gD}} + 0.22 \right) \tag{2.10}$$

where, U_m is the mixture velocity given in Equation 2.11,

$$U_m = j_g + j_l = j \tag{2.11}$$

From the equations above, the liquid superficial velocity at which transition occurs is given by Equation 2.12.

$$j_l = \sqrt{gD}\left(\frac{\frac{L_E}{D}}{40.6} + 0.22\right) - j_g \tag{2.12}$$

The critical parameter is the ratio L_E/D. As L_E/D tends to zero, the slug flow region will disappear from the flow map. Other researchers have used different models to determine the slug-churn transition irrespective of the entrance length criteria. Mishima and Ishii (1984) stated that the transition occurs when the mean gas volume fraction within the entire region, α_{avg} reaches the gas volume fraction within the slug-bubble section, α_{bs}, is defined by Equation 2.13, and α_{avg} is defined in Equation 2.14.

$$\alpha_{bs} = 1 - 0.813\left[\frac{(C_o - 1)j + 0.35\sqrt{\frac{gG\Delta\rho}{\rho_L}}}{j + 0.75\sqrt{\frac{gG\Delta\rho}{\rho_L}\left(\frac{\rho_L D^3 \Delta\rho}{U_L^2}\right)^{1/18}}}\right]^{0.75} \tag{2.13}$$

$$\alpha_{avg} = \frac{j_g}{C_o + 0.25\sqrt{\frac{gD\Delta\rho}{\rho_L}}} \tag{2.14}$$

$$C_o = 1.2 - 0.2\sqrt{\frac{\rho_g}{\rho_L}} \tag{2.15}$$

where, C_o is the distribution parameter, α_{avg} is the average gas volume fractions and j_g is the gas superficial velocity.

Brauner and Barnea (1986) and Barnea et al. (1985) postulated that the transition from slug to churn flow exists when the gas volume fraction within the liquid slug reaches the maximum of 0.52. While Barnea and Shemer (1989) suggested that the transition from slug to churn flow occurs when the gas volume fraction in the liquid slug, α_{bs} is 0.50-0.60. Chen and Brill (1997) stated that the transition from slug to churn flow can be attributed to the destruction of the liquid slug that has high gas volume fraction and relatively short length by the strong effect of the wake behind the preceding Taylor bubble, (see Figure 2.3). According to Van Hout et al. (1992), the relative liquid slug length β_s of 0.15 is the transition criteria from slug to churn flow. Where, $\beta_s = L_s/L_u$. L_u is the slug

unit which is divided into two sections, the liquid slug section L_s and the Tailor bubble section, L_{TB}.

However, all the researchers mentioned above had worked on small diameter pipes. In larger diameter pipes, Omebere-Iyari et al. (2007a) and Ohnuki and Akimoto (2000) continuously found churn flow at the gas volume fraction of about 0.6. The authors showed that churn flow is the dominant flow pattern in large diameter pipe. Churn flow was not been observed as entrance effect which is contrary to the initial understanding postulated by previous investigators who experimented on small diameter vertical pipes.

2.4.3 Churn to Annular Flow Transition

Churn flow is thought of as the most difficult flow pattern to understand due to the chaotic nature with the liquid film present along the pipe wall (Pagan et al., 2016a). As gas velocity is increased from the churn flow regime, the drag force is able to overcome the gravity of the liquid slug in the middle of the pipe which result in the continuous gas phase in the middle of the pipe and liquid film at the wall.
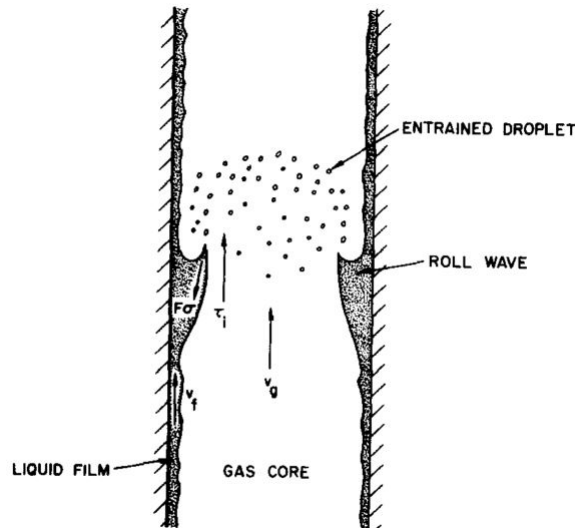
Figure 2.4: Wave Entrainment Mechanism

Mishima and Ishii (1984) proposed two mechanism for churn to annular transition. The authors postulated that the transition occurs due to:

- Flow reversal in the liquid film section along the large bubbles, and

- Destruction of liquid slugs or large waves by entrainment or deformation (Figure 2.4).

From the first criteria, the gas superficial velocity required to prevent liquid film falling back and thus ensure churn to annular flow transition is calculated by Equation 2.16.

$$j_g = \sqrt{\left(\frac{\Delta\rho g D}{\rho_g}\right)(\alpha - 0.11)} \tag{2.16}$$

The second criteria is related to large diameter pipe based on the onset of gas entrainment for film flow which result in the interplay of the force balance between the shearing force and the retaining force of the surface tension. The gas superficial velocity required is given by Equation 2.17.

$$j_g \geqslant \left(\frac{\sigma g \Delta\rho}{\rho_g^2}\right)^{1/4} N_{\mu f}^{-0.2} \tag{2.17}$$

where,

$$N_{\mu f} = \frac{\mu_f}{\left(\rho_f \sigma \sqrt{\frac{\sigma}{g\Delta\rho}}\right)^{1/2}} \tag{2.18}$$

However, Taitel et al. (1980) stated that there must be a balance between the gravity and the drag forces acting on the drop. This balance is shown in Equation 2.19.

$$\frac{1}{2}C_d \frac{\pi d^2}{4}\rho_G U_G^2 = \frac{\pi d^3}{6}g\Delta\rho \tag{2.19}$$

and,

$$U_G = \frac{2}{\sqrt{3}}\left[\frac{g d \Delta\rho}{\rho_G C_d}\right]^{1/2} \tag{2.20}$$

where d_g, the drop size was originally defined by Hinze (1955) in Equation 2.21.

$$d_g = \frac{k\sigma}{\rho_G U_G^2} \tag{2.21}$$

where $k = 30$, critical Weber number and $C_d = 0.44$. Combining Equation 2.19 and Equation 2.20, the minimum gas velocity below which annular flow cannot be seen is defined by Taitel et al. (1980) in Equation 2.22 and Equation 2.23.

$$U_G = \left(\frac{4K}{3C_d}\right)^{\frac{1}{4}}\frac{\left[\sigma g \Delta\rho\right]^{\frac{1}{4}}}{\rho_G^{\frac{1}{2}}} \tag{2.22}$$

and,

$$U_{GS} = 3.1 \frac{(\sigma g \Delta \rho)^{\frac{1}{4}}}{\rho_G^{\frac{1}{2}}} \tag{2.23}$$

Due to the thin film of liquid at the wall of a typical annular flow, the film velocity can be replaced by the film's superficial velocity (Taitel et al., 1980) hence, Equation (2.23) represent the final transition boundary.

Transition from churn to annular flow is quite important due to its application in gas lift operation, a state at which the gas velocity is sufficient to lift the entrained liquid droplets. The gas lift phenomenon is based on the entrained dispersed gas bubbles in the liquid which helps to reduce the gravity effect of the liquid to overcome the gravity force. In the gas lift system, fast moving gas bubbles exchange their momentum by transfer such that the liquid particles gain the energy required to be transported to the surface of the well.

Despite the foregoing analysis of past investigators, it is noticed that the semi-annular flow was not mentioned as an interregnum between churn flow and annular flow. Also, most of the investigations were carried out in small diameter pipes. However, researchers in large diameter pipes did not observe churn flow but, there is another flow pattern called semi-annular flow which is only mentioned by few authors (Spedding et al., 1998; Omebere-Iyari et al., 2007b). In addition, there is no mention of sand particles in the flow field and the impact this could have on bubble coalescence and breakup.

2.5 Drift Flux Model

A typical steady state and transient two-phase flow system can be solved using either a two-fluid model or a drift-flux model. The drift-flux model formulation is based on the mixture properties of the phases which is averaged over the cross-section of the pipe. It is therefore a simpler version of the two-fluid model where some of the properties of the fluid has been truncated but still represent an approximate solution of the two phase flow. The drift flux model was originally developed by Zuber and Findlay (1965) and later modified by Wallis (1969) and Ishii (1977), though, technically for small diameter pipe. Improvement has been made by Hibiki and Ishii (2003); Bhagwat and Ghajar (2014) and

others for large diameter pipes.

Typical drift flux parameters are area averaged over the cross section of the pipe. Mathematically, this is represented in Equation 2.24.

$$\langle F \rangle = \frac{1}{A} \int_A F dA \tag{2.24}$$

Invoking the drift flux model slip law relationship by Zuber and Findlay (1965) Equation 2.25 shows the correlation of the drift flux parameters.

$$V_g = C_o j + V_{gj} \tag{2.25}$$

where j is the fluid mixture superficial velocity expressed in Equation 2.26.

$$j = j_g + j_f \tag{2.26}$$

where j_g is the gas phase superficial velocity, j_f is the liquid phase superficial velocity, V_g is the in-situ gas phase velocity and V_{gj} is the gas phase drift velocity.

The one-dimensional drift flux formulation is described in Equation 2.27.

$$\langle \langle U_g \rangle \rangle = \frac{\langle j_g \rangle}{\langle \alpha_g \rangle} = C_o \langle j \rangle + \langle \langle U_{gj} \rangle \rangle \tag{2.27}$$

and,

$$\langle \alpha_g \rangle = \frac{\langle j_g \rangle}{C_o \langle j \rangle + \langle \langle U_{gj} \rangle \rangle} \tag{2.28}$$

where, the single bracket, $\langle \rangle$ and the double brackets, $\langle \langle \rangle \rangle$ indicate area averaged quantity over a cross section and void fraction-weighted averaged quantity respectively. C_o is the distribution coefficient that takes the radial profile of the velocity and the gas concentrations into consideration. The most important unknowns in the drift flux model are the distribution parameter and the drift (rise) velocity. These unknowns in the drift flux correlations can easily be obtained from a linear regression function of the void fraction-weighted mean gas velocity, $\langle \langle U_g \rangle \rangle$ and the mixture superficial velocity, $\langle j \rangle$. The gradient of the regression is equivalent to the distribution coefficient while the constant of the regression is the void fraction weighted mean drift velocity.

Mathematically, the distribution parameter and the void fraction-weighted mean drift velocity can also be obtained from the Equation 2.29 & 2.30 (Shen et al., 2014). According

27

to Bhagwat and Ghajar (2014), the distribution parameter is a representation that account for the distribution of the gas phase concentration across the pipe cross-section.

$$C_o = \frac{\langle \alpha_g j \rangle}{\langle \alpha_g \rangle \langle j \rangle} \tag{2.29}$$

and,

$$\langle \langle U_{gj} \rangle \rangle = \frac{\langle U_{gj} \alpha_g \rangle}{\langle \alpha_g \rangle} \tag{2.30}$$

where U_{gj} is the local drift velocity of the gas phase which is defined in Equation 2.31, and $\langle \langle U_{gj} \rangle \rangle$ is the cross sectional gas fraction weighted averaged of the local relative velocity of the gas phase with respect to the two phase mixture superficial velocity at the pipe volume centre. In CFD code, it is easy to calculate the mixture superficial velocity, j, and the local gas velocity, U_g such that the local drift velocity, U_{gj}, can easily be calculated using Equation 2.31.

$$U_{gj} = U_g - j = (1 - \alpha_g)(U_g - U_l) \tag{2.31}$$

Sometimes, it is possible that the gas and liquid in-situ velocity can be equal and in this case the RHS of Equation 2.31 can be zero. Hence, this equation is not applicable to all case scenarios found in two phase flow system.

Researchers have carried out some studies to develop drift flux correlations in large diameter pipe in order to determine the distribution parameter and the drift velocity. Of the many researchers that had developed drift flux correlation for large diameter pipe, Kataoka and Ishii (1987) and Ishii and Hibiki (2011) presented the most comprehensive correlations. It is generally accepted within the research community that the drift velocity and the distribution parameter depend on the pipe diameter, system pressure, gas and liquid superficial velocity and the fluid properties. The flow pattern depends on the gas superficial velocity hence, the drift velocity and distribution parameter also depend on the flow pattern.

Different researchers had proposed different values for the profile parameter, C_o, most of which were derived from small diameter pipes and with air-water experimental data. However, according to Hibiki and Ishii (2003), in a large diameter pipe, slug bubbles cannot be sustained due to interfacial instabilities. Therefore, the profile parameter and the drift velocity in a large diameter pipe can be different from those of small diameter.

Hence, models developed for small diameter pipes cannot be used for large diameter pipe. There is therefore the need for further study of two-phase gas-liquid flow in large diameter pipe.

2.6 Flow Regime Maps

Multi-phase flow hydrodynamics is characterised by different topological configurations known as flow patterns or flow regimes which can be represented on a coordinate system for prediction and analysis. The transition of the phase distribution corresponds to the change of flow pattern. These changes depend on the homogeneity and heterogeneity of the interacting phases that lead to the prevailing phase configurations observed. The fluid properties and pipe sizes play a major role in the prevailing geometrical shape developed in the flow field. Omebere-Iyari et al. (2008) investigated the impact of fluid properties and postulated that under the same conditions, the gas fractions developed in petroleum-like fluid is higher than its counterpart obtained from air and water mixtures. Similarly, as shown in Table 2.1, the pipe diameter discrimination using Kataoka and Ishii (1987) formulation, depends on the fluid properties. The table shows that large pipe for oil and gas fluid is a size greater than 80mm while, for air water pipe, large diameter pipe is a size greater than 120mm. Ohnuki and Akimoto (2000), Oddie et al. (2003), Sun et al. (2003), Omebere-Iyari et al. (2007b), Omebere-Iyari et al. (2008), Schlegel et al. (2009), Smith et al. (2012) and Ali Farman and Yeung (2015) performed experimental studies in larger diameter pipe that ranges from 101.6mm to 480mm. Only Omebere-Iyari et al. (2007b) and Oddie et al. (2003) used nitrogen (gas) and naphtha (liquid) mixtures while others used air and water, hence there are discrepancies in their experimental outcomes.

There are many flow pattern maps that have been developed from correlations and experimental results. However, most of these flow pattern or regime maps were for small diameter pipes, but the flow regimes in large pipe are significantly different and require separate analysis. Mishima and Ishii (1984) and Oddie et al. (2003) stated that correlations developed from small diameter pipes that are used in software codes like Eclipse software for large diameter operations are greatly in error due to pipe scale differences and fluid properties. Typical flow maps developed for large diameter pipe

in literature which are most referenced are from the works of Schlegel et al. (2009), Omebere-Iyari et al. (2008), Omebere-Iyari et al. (2007b), and Ohnuki and Akimoto (2000). However, there are discrepancies in the outcome of their experiments which is largely due to differences in their analysis, data range and fluid properties. Hence, database for large diameter pipes are greatly lacking. Further work is required to understand the flow development in large diameter pipes. Details gas fraction analysis needs to be carried out to study the effect of increased turbulence on flow regime transitions in large diameter pipes (Schlegel et al., 2009).

Flow regimes are mapped in different coordinate systems. This choice of coordinate units system for the flow maps has been made differently by many researchers. Pioneer researcher, Wallis (1969) was the first to present his flow map in superficial velocity scales. Taitel et al. (1980) also used the gas and liquid superficial velocity, Equation 2.35, in his flow map coordinates. Some researchers had chosen non-dimensional units. Most notably, Hewitt and Roberts (1969) used the superficial momentum fluxes, Equation 2.32, for gas and liquid. While other researchers used the mass flux, G defined in Equation 2.33 and Equation 2.34.

$$J_{g,l} = \frac{\rho_{g,l}}{j_{g,l}^2} \tag{2.32}$$

Some other authors had used the superficial mass flux G where,

$$G_g = \frac{M_g}{A} = j_g \rho_g \tag{2.33}$$

and,

$$G_l = \frac{M_l}{A} = j_l \rho_l \tag{2.34}$$

The Superficial velocity (volumetric flux) is defined as:

$$U_{gs} = \frac{Q}{A} \tag{2.35}$$

where, A is the cross-sectional area calculated from the hydraulic diameter open for flow passage.

2.7   Three-Phase Gas-Liquid-Solid Flow System

Most of the experimental and CFD studies carried out in multi-phase flow in the oil & gas industry have concentrated on two-phase gas-liquid flows while three-phase gas-liquid-solid flow studies are scarce in literature. Hence gas-liquid-solid phase database in the oil & gas industry are very limited. Thus, further investigations into the dynamics of such flows are greatly required. Three-phase gas-liquid-solid flow in the oil & gas industry has both negative and positive impact. While sand production could help increase flow efficiency from the reservoir, it however causes lifting problem and equipment erosion in the wellbore and in the surface facilities. However, three-phase flow fluidisation has found usefulness in the process and chemical industries where solid catalyst particles are suspended in a co-current gas-liquid upflow stream. Extensive applications of gas-liquid-solid fluidized bed reactors can be found in upgrading and hydro-conversion of heavy oil fractions, Fischer – Tropsch synthesis, waste water treatment, coal combustion, and catalytic hydrogenation of unsaturated fatty oils (Hamidipour et al., 2012). Hence, researchers mainly from the chemical and biotechnical engineering have done extensive work in the simulation of gas-liquid-solid flow.

Although, in the context of oil & gas production, multi-phase is a minimum of four phases (gas, oil, water and solid) in the flow stream; notable researchers in multi-phase flows such as Pietrzak et al. (2017), Shi et al. (2005) and Oddie et al. (2003) had only considered three-phase such as gas-oil-water flows without considering the sand phase. For efficient transportation of sand particles from the wellbore to the surface via vertical and inclined pipes, fluidisation must take place. Ineffective fluidisation leads to sand deposit and wellbore filling. Thus, the kinetic energy developed from the flow stream required to lift the sand particle to the surface is key to the transportation of solids and entrained particles to the surface. The CFD methodology from the chemical and process industry (Hagedorn et al., 1965) has been fully developed and can be applied directly to oil and gas with modification to study the hydrodynamics of gas-oil/water-solid flows in an oil related vertical pipes.

2.8 Computational Fluid Dynamics

Earlier attempts to investigate multi-phase flow in pipes in oil & gas wells were first through analytical studies (Versluys et al., 1930; Poettman et al., 1952), and then through empirical correlations (Hagedorn et al., 1965) and mechanistic 1D models (Ozon et al., 1987; Hasan et al., 1988; Ansari et al., 1990). However, these models were limited in their application to wider scenarios and also constrained by the complexity of resolving the interfacial transfer terms. Such complexity increases with the presence of sand particles in the flow stream (Lakehal, 2013; Gharaibah et al., 2015). In a typical 1D mechanistic models and empirical correlations, it is necessary to prior knowledge of the flow pattern in order to determine how the flow will develop before predictions are conducted.

The advancement in computing hardware has paved way for numerical computing method which is commonly called computational fluid dymamics (CFD). CFD is the analysis of systems involving fluid flow, heat transfer, and associated phenomenon such as chemical reactions by means of computer based simulation (Versteeg and Malalasekera, 2007) which is implemented by solving the continuity, momentum and energy balance equations. This progress in fluid dynamics would eliminate the need to have a priori knowledge of the flow pattern before computational predictions are carried out. CFD has the capability to provide detailed, visualized and comprehensive information of the flow dynamics which might be difficult to obtain through experimental procedure (Yamoah et al., 2015).

There are different codes that have been developed for the computation of multi-phase flow hydrodynamics but, closure laws are required to account for the phase interactions and interfacial forces. Due to these complexities, different models have been adopted for different flow patterns. Rzehak and Krepper (2013) carried out extensive CFD study to investigate the closure models for bubbly flow using Euler-Euler two fluid model with referenced data set from literatures. The authors proposed guidelines for modelling bubbly flows.

According to Ishii and Hibiki (2011), the interfacial transport of mass, momentum and energy is proportional to the interfacial area concentration (the interfacial area per

unit volume) and to a driving force which characterise the kinematics effect and therefore, must be related to the structure of two phase flow. Hence, better understanding of the coalescence and break up effect due to the interactions among the bubbles and between the bubbles and turbulence eddies is important to effective modelling of multi-phase flow (Cheung et al., 2007). In this regard, the multiple size group (MUSIG) model was developed from the Population Balance Model (PBM) (Yeoh and Tu, 2005, 2004) but for bubbly flows. However, the computational time required is enormous and thus made it unattractive for practical purpose. The combination of population balance and CFD technique offers unique hybrid model for computation of bubble coalescence and break up (Ramkrishna and Mahoney, 2002) but it is implicitly complex and requires great computing power. On the contrary, the development in interfacial area transport equation (IATE) by Ishii and Hibiki (2011) provides a simple means of modelling the spatial evolution of the geometrical structures which account for the flow pattern development and transitions of the flow regimes.

In order to simulate the flow patterns of a two-phase gas-liquid flow, researchers had used different separate numerical models for different flow patterns one at a time. Tomiyama et al. (1993), Anglart and Nylund (1996), Krepper et al. (2005), Pang et al. (2010) and Rzehak and Krepper (2013) performed numerical studies to investigate the evolution of bubbly flows and associated interfacial interactions. While Taha and Cui (2006), used the Volume of fluid (VOF) model in ANSYS CFX to predict the evolution of slug flow in vertical pipe. However, the author did not consider the bubbly to slug transitions. Similarly, Da Riva and Del Col (2009) used the VOF model to perform numerical simulation of churn flow. Besides, Liu et al. (2011) developed a two-fluid, two-components CFD model to simulate vertical upward two phase annular flow without discussing the transitions to and from any specific flow patterns.

Montoya et al. (2016) performed a comprehensive review on the mechanism and models for the churn-turbulent flow regime. The authors also examined the dynamics of churn-turbulent flow and the transitions to and from this flow pattern. The authors noted that despite the extensive attempts, robust and accurate simulations techniques for conditions such as transitions from bubbly to annular flow are still lacking. A reliable CFD model for multi-phase flow should be able to dynamically reproduce any changes

depending on the established channel and boundary conditions. Only such CFD numerical simulation models could correctly predict highly turbulent, space and time dependent flows (Montoya et al., 2016).

Recently, Kim et al. (2021) states that the IATE formulation could dynamically model the evolution of interfacial structures via mechanistic modelling of fluid particle interaction, such that it reflects the true dynamic nature of the interfacial structure and gradual flow regime transition. Although the IATE was initially developed for bubbly flow, the authors stated that it can be extended to churn and annular flow simulations. In this research, a CFD computation was performed to simulate two phase gas-liquid flow with Euler-Euler model with IATE and the results were validated. It was discovered that the model was capable of simulating all flow regime spectrum. This model was then extended to simulate and investigate three-phase gas-liquid-solid flows. The results were also validated against published experimental and CFD work.

The theory and basis of Fluid dynamics, CFD and turbulence modelling relevant to this work are found in the books of Schetz and Fuhs (1999), Pope (2001), Kundu and Cohen (2002), Ferziger et al. (2002), Versteeg and Malalasekera (2007) and Ishii and Hibiki (2011).

MULTI-PHASE FLOW MODELLING

3.1 The CFD Method

It has been elucidated in the foregoing chapter that greatest problem in the study of multi-phase flow has been how to resolve the interfacial transfer forces. In the past, this seemed insurmountable, but with the advent of new computing power, a computational fluid dynamics (CFD) method has been able to proffer solution to the once insurmountable set back. A CFD method is therefore applied in this project using the state of the art ANSYS Fluent computational tool for multi-phase flows. ANSYS Fluent provides the volume-of-fluid (VOF), mixture, and Eulerian computational models. The VOF model is suitable for immiscible fluids where the flow is separated, and the interface is tracked using various interface tracking techniques like Geo-Reconstruct, compressive interface capturing scheme for arbitrary meshes (CICSAM) and Modified High Resolution Interface Capturing (HRIC) scheme. The mixture model is a simplified version of the Euler-Euler model which assumes the phases interact strongly but a single momentum equation is used for the phases using mixture properties of the phases. The Eulerian model is a robust method of the two-fluid approach in which the two phases are treated as interpenetration continuum. It solves the instantaneous continuity and momentum equations for each phase separately with a single energy equation.

There are two numerical approaches in the modelling architecture, the Euler-Lagrange and the Euler-Euler numerical computation methods. In the Eulerian approach, a control volume is defined where the fluid flow occurs and the fluid properties are defined as field with time dependency and the individual fluid particles are considered to be inter-penetrating continua. While in the Lagrangian approach, the fluid particles are

considered discrete entities which are tracked and the variations along the trajectory are defined. Both methods can lead to the same result if appropriate numerical schemes are used to solve the resulting formulation (Sokolichin et al., 1997).

The combination of these approaches gave birth to the two methodology in multi-phase flow simulation called the Euler-Euler (two-fluid) and the Euler-Lagrange multi-phase flow simulation methods. These two basic CFD multi-phase flow modelling methods are available in commercial CFD packages for numerical computation of multi-phase flow hydrodynamic parameters. Stringent selection of the appropriate modelling method from the two broad methods described above can be a daunting task. The comparison of the numerical approaches are shown in Table 3.1 which is used as a first pass screening criteria for the selection of fit for purpose model for this research. The Lagrangian formulation has different capabilities for various interactions such as the discrete phase model (DPM), discrete element model (DEM), dense discrete phase model (DDPM) with optional kinetic theory of granular flow (KTGF). The Eulerian-Eulerian approach is more general in that it allows the simulation of all types of multi-phase combination once proper phase interaction models are defined. Although, the dynamic motions of dispersed phases in a continuous phase carrier flow can be modelled by either adopting the Eulerian-Eulerian or the Eulerian-Lagrangian framework (Gharaibah et al., 2015).

As earlier mentioned in the literature review, it has been recognised since 1965 that the way forward in understandings the complex flow mechanism that occurs in multi-phase flow is through a resolved solution of the Navier-Stokes Equation. This complexity is as a result of the interactions and inter-phase couplings of momentum, mass and energy between the different phases (Panneerselvan et al 2009). The foundation of the CFD methodology is the principle of the conservation of mass, momentum and energy. The solver is based on different numerical schemes and the transport equations for mass, momentum and energy are solved for each phase components in the flow stream. A typical CFD solution procedure is developed and achieved through:

- discretisation of the domain into sets of finite control volumes called cells.

- Discretisation of Partial differential equations into sets of algebraic equations.

- Solving the algebraic numerical equations to convergence to achieve the solution

Table 3.1: Model Selection Grid (Fluent 2018)

Model	Numerical Approach	Particle-Fluid Interaction	Particle-particle Interaction	Particle size Distribution (PSD)
DPM	Fluid–Eulerian Particles-Lagrangian	Empirical models for sub-grid particles	Neglected	Easy to include PSD because of Lagrangian description
DDPM-KTGF	Fluid–Eulerian Particles-Lagrangian	Empirical models for sub-grid particles	Approximate P-P interactions determined by granular models	Easy to include PSD because of Lagrangian description
DDPM-DEM	Fluid-Eulerian Particles-Lagrangian	Empirical models for sub-grid particles	Accurate determination of P-P interactions	Easy to include PSD because of Lagrangian description
Macroscopic Particle Model	Fluid-Eulerian Particles-Lagrangian	Interactions are determined as part of solution: particles span many fluid cells	Accurate determination of P-P interactions	Easy to include PSD; if particles become smaller than the mesh, uses an empirical model
Euler-Granular Model	Fluid-Eulerian Particles-Eulerian	Empirical models for sub-grid particles	P-P interactions modelled by fluids properties such as granular pressure, viscosity, drag, etc.	Different phases to account for a PSD; when size change operations happen, use population balance models

field.

Most of the flows of engineering significance are turbulent in nature. Turbulent flow occurs when the velocity and all other flow properties vary randomly and in a chaotic way. The biggest challenges with multi-phase flow is how to resolve the turbulent fluctuations in the properties of turbulent flow. There are three approaches to modelling turbulence and these are the Direct Numerical Simulation (DNS), the Large Eddy Simulation (LES) and the Reynolds-Average Navier-Stokes (RANS) equations. Each of these can be implemented using different numerical techniques such as the finite volume method (FVM), the finite element method (FEM) and the finite difference method (FDM). The DNS approach is computationally intensive in simulation time, and hence its limitations for computation of large scale practical engineering flow problems. The LES method directly resolves turbulent flow as distinct large and small scale fluctuations. Although the LES approach is also quite expensive, advances in computing power has helped in this regard to make it commercially attractive to end users. The most commonly used approach for most practical purpose is the RANS Equation approach which is less expensive in terms of time and memory that are required. The choice of the RANS equations method is due to the fact that it is not very necessary to predict the detailed

flow and instantaneous information of the entire turbulence scale in most engineering applications. The RANS equations approach solves time-averaged Navier-Stokes equation for all turbulent length scales.

The most difficult aspect of multi-phase modelling is the interfacial interaction forces between the phases and particularly for three phase flows. The interfacial transfer terms are directly proportional to the interfacial area concentration (IAC) which is the total area per mixture volume (Ishii and Hibiki, 2011). Accurate modelling of the IAC is therefore a prerequisite for detailed analysis of two phase flows using the two fluid model (Sharma et al., 2019). To better represent the dynamics of the evolution of the structure of two phase flow, a more mechanistic approach, the Interfacial Area Transport Equations (IATE) was proposed by Kocamustafaogullari and Ishii (1995). This method is simplified in comparison to the more advanced population balance model. The IATE is thus used in this project with the Eulerian model. The model treat the two and three phases as inter-penetrating continua. The following sections shows the outlook of the type and theories of multi-phase flow. Full description of theories of two-fluid model and CFD models available in commercial CFD packages are described in the books of Pope (2001), Versteeg and Malalasekera (2007) and Ishii and Hibiki (2011).

3.1.1 The VOF Model

The VOF model uses the interface tracking scheme to track the interface and volume fraction of two immiscible fluids. The VOF method shares a single set of momentum equation for all phases. The key point on the VOF model treatment of multi-phase flow is that the two fluids are not inter-penetrating. Less attention is paid to the VOF model in this research due to the inadequacy of the model relative to predicting wider range of multi-phase flow regime.

3.1.2 The Mixture Model

The mixture model is a simplified version of the Eulerian model. The mixture model can be used to model any number and type (fluid and solid) of phases unlike the VOF model. It can be used to model n number of phases (fluid or particulate) by solving

the momentum, continuity, and energy equations for the mixture, the volume fraction equations for the secondary phase and algebraic expressions for the relative velocities. The mixture model is not used in this research due to the limitations in multi-phase modelling of complex flows.

3.1.3 The Eulerian and Multi-fluid VOF Model

The Eulerian multi-phase modelling in a commercial CFD code allows for the modelling of multiple separate, yet inter-penetrating phases. The Eulerian phases can be liquids, gases, or solids in any number of combination but are coupled through their phasic fractions. The volume phasic fraction is described by Equation 3.1.

$$V_i = \int_v \alpha_i dV \tag{3.1}$$

where:

$$\sum_{i=1}^{n} \alpha_i = 1 \tag{3.2}$$

The effective density of phase i ($i = g, l, s$) defines the properties in the control volume which is determined by Equation 3.3.

$$\hat{\rho}_i = \alpha_i \rho_i \tag{3.3}$$

where ρ_i is the physical density of phase i. The Eulerian multi-fluid VOF model is a hybrid model that couples the Eulerian model with the VOF model. The multi-fluid VOF model provides a framework where flow structures with interfaces in relatively large scale (that can be reasonably resolved in a computational mesh) are tracked by the VOF model while the small scales multi-phase flow structures are accounted for by the Eulerian scheme. This hybrid model provides composite discretization scheme for both sharp and dispersed phase by using the Compressive and HRIC interface capturing scheme (Wacławczyk and Koronowicz, 2008; Khrabry et al., 2011) with symmetric (isotropic) and anisotropic drag laws. The symmetric drag law has limitations at higher drag coefficient while the anisotropic drag law direct the higher drag in the normal direction to the interface and less in the tangential direction to the interface. Multi-phase flow simulation using the CFD method can be achieve either through the Eulerian framework or the

Lagrangian framework and appropriate combination of the methods. In the Eulerian system, all variables are described in terms of a single set of fixed coordinate plus time while in the Lagrangian system, the position of each particle is studied as a function of time and the particle's initial position (Schetz and Fuhs, 1999). Details of these systems and the selection criteria are discussed on the next two sections.

3.2 The Euler-Lagrange Approach

In this method, the fluid phase is treated as a continuum and one set of conservation equations is solved for this phase, while the dispersed phase is solved by tracking a large number of particles, bubbles, or droplets through the calculated flow field. The dispersed phase can exchange momentum, mass, and energy with the continuous phase and this is taken into account by separate models for drag and non-drag forces, (Fluent, 2018). This method is very complex due to particle-particle interaction which could be neglected for simplicity. This approach is most applicable where the particle concentration is relatively low.

3.3 The Euler-Euler Approach

In the Euler-Euler approach (also know as two-fluid model), different phases (gas, liquid or solid) are treated mathematically as inter-penetrating continua. Since the spatial volume of a phase cannot be occupied by the other phases, the concept of phasic volume fraction is introduced. These volume fractions are assumed to be continuous functions of space and time and their sum is always equal to one. Conservation equations for each phase are derived to obtain sets of equations, which have similar structure for all phases. These equations are closed by providing constitutive relations that are obtained from empirical information, or in the case of granular flows, by application of kinetic theory of granular flow (KTGF) (Fluent, 2018). In the Euler-Euler reference frame, three models are available for computational analysis, the VOF model, the Mixture model and the Eulerian model. To choose a model, the first thing to do is to identify the prevailing flow regime that

best fit the multi-phase case to be modelled. The Euler-Euler model is the most versatile of the Eulerian method as it is capable of modelling complex flows of multiple phases including solid particles. The combination of such is the Euler-Euler-Granular model. The Euler-Euler and the granular combination model is computationally efficient in modelling complex multi-phase flows which contains gas-liquid-solid flow combination. This feature is utilised in this research to examine the hydrodynamics of two-phase gas-liquid and then three-phase gas-liquid-solid flows. Full details of the description of the two-fluid model is found in the text of Ishii and Hibiki (2011).

3.4 Description of the Computational Methods

The mathematical equations used to compute and predict the multiphase flow hydrodynamics are based on the conservation equation for mass, momentum and energy for the three phases. A 3D transient CFD model using the Eulerian multi-fluid VOF approach in combination with interfacial area transport equations (IATE) was adopted for this research. This model considers the three phases to be inter-penetrating continuum.

The Multi-fluid VOF is a hybrid version that couples the VOF and Eulerian methods. It allows the use of discretization schemes and options suited to both sharp and dispersed interface regimes while overcoming some limitations of the VOF model that arise due to the shared velocity formulation. This allows the use of interface sharpening schemes (Like Geo-Reconstruct, Compressive and CICSAM) in the Eulerian framework along with the symmetric and anisotropic drag laws. The symmetric drag law, which is used as the default in the sharp interface regime, is isotropic and tends to approach the behaviour of the VOF model for high drag coefficients. The anisotropic drag law helps to overcome a limitation of the symmetric drag law by allowing higher drag in the normal direction to the interface and lower drag in the tangential direction (Fluent, 2018; Dai et al., 2013). Hence the anisotropic drag law was adopted in this research for the fluid system.

The pressure field is shared by the three phases in accordance to their phasic fractions. The liquid phase is treated as the primary (continuous) phase while the gas is the secondary (disperse) phase for two-phase flow and gas & solid are both treated as secondary phases in the case of three-phase flow simulation. The transport equations

for this research are based on the Euler-Euler-Euler approach in which the gas, liquid and solids are treated as three independent phases but considered as pseudo continuum (Li and Zhong, 2015). Thus, each phase has its own conservative mass and momentum flux equations that are solved using the phase-coupled SIMPLE (PC-SIMPLE) algorithm in ANSYS Fluent.

3.4.1 Mass balance equation

The general continuity equation for each phase i, $(i = g, l, s)$ which is valid for compressible and incompressible flows in which there are no mass transfer between the phases is given in Equations 3.4 - 3.6.

For gas,

$$\frac{\partial}{\partial t}\left(\alpha_g \rho_g\right) + \nabla.\left(\alpha_g \rho_g \vec{v}_g\right) = 0 \tag{3.4}$$

For liquid,

$$\frac{\partial}{\partial t}\left(\alpha_l \rho_l\right) + \nabla.\left(\alpha_l \rho_l \vec{v}_l\right) = 0 \tag{3.5}$$

For solid,

$$\frac{\partial}{\partial t}\left(\alpha_s \rho_s\right) + \nabla.\left(\alpha_s \rho_s \vec{v}_s\right) = 0 \tag{3.6}$$

where the phasic volume fractions should satisfy the constitutive relation of Equation 3.7.

$$\alpha_l + \alpha_g + \alpha_s = 1 \tag{3.7}$$

where,

$\vec{v}_i$ is the phase velocity, ρ_i is the phase density.

3.4.2 Momentum Balance Equation

The momentum exchange conservation is derived from Newton's second law which states that the rate of change of momentum of a fluid particle is equal to the sum of the forces on the particle. There are two main types of forces in such balance interplay. These are the surface (pressure, viscous) force which is treated separately in the momentum equation and the body (gravity, centrifugal, coriolis, electromagnetic) force which is normally

regarded as the source terms (Versteeg and Malalasekera, 2007). These equations are described mathematically in Equations 3.8 - 3.10 for the respective phases.

For gas,

$$\frac{\partial}{\partial t}(\alpha_g \rho_g \vec{v}_g) + \nabla.(\alpha_g \rho_g \vec{v}_g \vec{v}_g) = -\alpha_g \nabla p + \nabla.\overline{\overline{\tau}}_g + \alpha_g \rho_g \vec{g} + M_{i,g} \tag{3.8}$$

For liquid,

$$\frac{\partial}{\partial t}(\alpha_l \rho_l \vec{v}_l) + \nabla.(\alpha_l \rho_l \vec{v}_l \vec{v}_l) = -\alpha_l \nabla p + \nabla.\overline{\overline{\tau}}_l + \alpha_l \rho_l \vec{g} + M_{i,l} \tag{3.9}$$

For ganular phase solid,

$$\frac{\partial}{\partial t}(\alpha_s \rho_s \vec{v}_s) + \nabla.(\alpha_s \rho_s \vec{v}_s \vec{v}_s) = -\alpha_s \nabla p_{fr} - \nabla p_s + \nabla.\overline{\overline{\tau}}_s + \alpha_s \rho_s \vec{g} + M_{i,s} \tag{3.10}$$

where $\overline{\overline{\tau}}$ is the stress -strain tensor is mathematically described in Equations 3.11 - 3.13.

$$\overline{\overline{\tau}}_g = \mu_{eff,g}\left[\left(\nabla \vec{v}_g + \nabla \vec{v}_g^T\right) - \frac{2}{3}\nabla.\vec{v}_g \overline{\overline{I}}\right] \tag{3.11}$$

$$\overline{\overline{\tau}}_l = \mu_{eff,l}\left[\left(\nabla \vec{v}_l + \nabla \vec{v}_l^T\right) - \frac{2}{3}\nabla.\vec{v}_l \overline{\overline{I}}\right] \tag{3.12}$$

$$\overline{\overline{\tau}}_s = \mu_{eff,s}\left(\nabla \vec{v}_s + \nabla \vec{v}_s^T\right) + \left(\lambda_s - \frac{2}{3}\mu_{eff,s}\right)\nabla.\vec{v}_s \overline{\overline{I}} \tag{3.13}$$

where, with respect to phase, p_s is additional solid pressure due to solid collision, p is static pressure, λ_s is the bulk viscosity, $M_{i,l}, M_{i,g}, M_{i,s}$ represent the inter-phase force term for liquid, gas and solid phase respectively, μ_{eff} is the effective molecular viscosity, $\overline{\overline{I}}$ is the unit tensor, while $\nabla.\vec{v}_s \overline{\overline{I}}$, accounts for the effect of volume dilation in the system. In the above equations, the sign convention for pressure is negative because it is a compressive force while the viscous stress (tensile stress) is in opposite direction and thus takes a positive sign. The effective molecular viscosity shown in Equations 3.11 - 3.13, governs the diffusion of the momentum in each phase. For each phase, the effective viscosity is given in Equations 3.14 - 3.16

$$\mu_{eff,l} = \mu_l + \mu_{T,l} + \mu_{g,l} + \mu_{s,l} \tag{3.14}$$

$$\mu_{eff,g} = \mu_g + \mu_{T,g} \tag{3.15}$$

$$\mu_{eff,s} = \mu_s + \mu_{T,s} \tag{3.16}$$

where, $\mu_{l,g,s}$ are the molecular viscosities, $\mu_{T,l,g,s}$ are the eddy induced viscosities for the respective phases, while $\mu_{g,l}$ and $\mu_{s,l}$ are the gas bubble and solid particle induced viscosities on the liquid phase. The solid phase molecular viscosity μ_s is further decomposed into other components described in Equation 3.40.

3.4.3 Conservation of Energy

The energy equation is derived from the first law of thermodynamics which states that the rate of change of energy of a fluid particle is equal to the rate of heat addition to the fluid particle plus the rate of work done on the particle (Versteeg and Malalasekera, 2007). The energy equation is generally not considered for incompressible fluids flow because the density is assumed to be constant i.e. without heat transfer. Without the density variation, there is no linkage between the energy equation and the mass and momentum conservation equations and in which case the density in the mass and momentum equations would be excluded from the equations (Versteeg and Malalasekera, 2007). In this research work, density changes due to temperature and pressure is negligible. The dynamic viscosity is also assumed to be constant (Isothermal condition is assumed). Changes in momentum is due to pressure and velocity only. Hence, in this research work, the fluid flow is simulated by considering the mass and momentum equations only. However, the energy equation is similarly described by separate enthalpy formulation described in Equation 3.17.

$$\frac{\partial}{\partial t}\left(\alpha_q \rho_q h_q\right) + \nabla.\left(\alpha_q \rho_q \vec{u}_q h_q\right) = \alpha_q \frac{dp_q}{dt} + \bar{\bar{\tau}}(\nabla \vec{u}_p - \nabla.\vec{q}_q)$$
$$+ S_q + \sum_{p=1}^{n}\left(Q_{pq} + \dot{m}_{pq}h_{pq} - \dot{m}_{qp}h_{qp}\right) \tag{3.17}$$

Where, with respect to phase q^{th}: h_q is specific enthalpy, S_q is source term, $\vec{q}_q$ is heat flux, Q_{pq} is heat intensity exchange between the phases and h_{pq} is interface enthalpy.

3.4.4 Interfacial Area Transport Equation (IATE)

The Interfacial Area Transport Equation (IATE) was first p roposed by Kocamustafaogullari and Ishii (1995) to account for the transport mechanisms in two-phase bubbly flow. T he t ransport m echanism i n t wo-phase fl ow de pends on the Interfacial Area concentration (IAC) and the driving force. The IAC is the inferfacial area per unit mixture volume. Since the two-fluid model treats the two phases differently, the transfer of mass, momentum and energy takes place at the interface. The interfacial interaction terms couples the two fluids w ithout w hich t he t wo p hases a re essentially independent. Thus, the interfacial transfer terms is the product of the IAC and the driving force. Prior to the IATE being formulated, flow r egime d epended correlation approach of predicting the IAC would require that the flow r egime b e k nown fi rst and then calculate the IAC. This process was time consuming and prone to errors. The IATE dynamically predicts the IAC in two-phase flow w ithout p rior k nowledge o f t he flow regimes. Constitutive equations are thus required to predict the transport mechanism for different flow conditions.

The Interfacial Area Transport Equation is formulated based on the Boltzmann transport equation which describes the particle transport by an integro-differential equation of the particle distribution function. For two-phase flow s ystem, t he particle transport equation is described in Equation 3.18.

$$\frac{\partial f}{\partial t} + \nabla.(fv) + \frac{\partial}{\partial V}\left(f\frac{dV}{dt}\right) = \sum_j \left(S_j + S_{ph}\right) \tag{3.18}$$

where, S_j ans S_{ph} are the particle source and sink rates per unit mixture volume V, due to the jth phase particle velocity and f is the particle number density function. Without proof, the macroscopic form of equation Equation 3.18 for the transport equation of the interfacial area concentration for one-group and two-group can be obtained by multiplying the equation by the surface area of particles of volume V, $A_i(V)$. After integrating over the volume within which each bubble group is defined and simplifying, the resulting equation are given in Equations 3.19 - 3.20

for one-group,

$$\frac{\partial(a_{i1}}{\partial t} + \nabla.(a_{i1}v_{i1}) + \int_{Vmin}^{Vc} \left\{ A_i \frac{\partial}{\partial V} \left(f \frac{dV}{dt} \right) \right\} dV = \int_{Vmin}^{Vc} \left(\sum_j (S_j + S_{ph}) \right) A_i dV \quad (3.19)$$

and for two-group,

$$\frac{\partial(a_{i2}}{\partial t} + \nabla.(a_{i2}v_{i2}) + \int_{Vc}^{Vmax} \left\{ A_i \frac{\partial}{\partial V} \left(f \frac{dV}{dt} \right) \right\} dV = \int_{Vc}^{Vmax} \left(\sum_j (S_j A_i dV) \right) \quad (3.20)$$

where, d/dt denote substantial derivative, a_i is the interfacial area concentration, v_i is the interfacial velocity, A_i is the surface area and V is the particle volume. Details of the IATE and all constitutive equations are found in Ishii and Hibiki (2011).

To close the IATE, the source and sink term are represented with constitutive relations which are defined as:

for particle number source and sink,

$$\int_{Vmin}^{Vmax} \left(\sum_j (S_j dV) \right) = \sum_j R_j \quad (3.21)$$

for source and sink rate for a_i

$$\int_{Vmin}^{Vmax} \left(\sum_j (S_j A_i dV) \right) = \sum_j \phi_j \quad (3.22)$$

The obvious interfacial interaction mechanism which result in particle coalescence and disintegration and modelled mechanistically to close the IATE and which for the interaction between the two group of bubbles. These are, Random Collision R_{RC}, wake entrainment R_{WE}, Turbulent impact T_{TI}, surface instability R_{SI}, and rise velocity R_{RV}.

In this research, Ansys Fluent is used to model the integral source and sink terms in the interfacial area transport equation caused by particle coalescence and breakup mechanism mentioned above. The transport equation for the interfacial area concentration equation used is given in Equation 3.23.

$$\frac{\partial \left(\rho_g X p \right)}{\partial t} + \nabla.\left(\alpha_g \vec{u}_g X_p \right) = \frac{1}{3} \frac{D\rho_q}{Dt} X_p + \frac{2}{3} \frac{\dot{m}_g}{\alpha_g} X_p + \rho_g \left(S_{RC} + S_{WE} + S_{TI} \right) \quad (3.23)$$

where:

X_p is the interfacial area concentration ($\frac{m^2}{m^3}$), α_g is the gas volume fraction, $\frac{1}{3} \frac{D\rho_q}{Dt} X_p$ is the gas bubble expansion due to compressibility and $\frac{2}{3} \frac{\dot{m}_g}{\alpha_g} X_p$ is the mass transfer (phase

change). $\dot{m}_g$ is the mass transfer rate into the gas phase per unit mixture volume ($\frac{kgs^{-1}}{m^3}$). S_{RC} and S_{WE} are the coalescence and sink terms due to random collision and wake entrainment respectively. S_{TI} is the breakage source term due to turbulent impact. The interfacial area concentration solves for the three effects that are responsible for the mass, momentum and energy transfer through the interface of the phases. There are three models available in Fluent to model the influence of interfacial area and these are the Hibiki and Ishii (2000) model, the Ishii and Kim (2001) & Wu et al. (1998) models, and the Yao and Morel (2004) Model. In this work, Hibki-Ishii model was used to model the coalescence and breakage. Details of these models are given in subsubsection 4.3.1.1 of this thesis.

3.5 Closure Laws for Interface Momentum Exchange

One of the major problems with the Eulerian model is the numerous constitutive equations required to close the momentum equations and strings of assumptions in the turbulent modelling due to phase interactions (Tebowei, 2016). The phase interaction terms describe the transfer of mass, momentum and energy between the phases. There are additional unknowns in the conservation equations that need to be modelled to close the system of equations to enable a numerical solution to be reached. Typical effects that are modelled for dispersed flows are drag forces, lift forces, turbulent dispersion, and droplet or bubble coalescence or break-up (Gharaibah et al., 2015). Such effects should be interpreted and closed by appropriate closure models. These closure models are discussed in the following sections.

With regards to multi-phase flow, the complexity of the modelling and understanding of the flow dynamics is the interface transfer forces. The M_i terms in the momentum Equations 3.8 - 3.10 account for the interface forces which need to be resolved through empirical correlations and assumptions. The selection criteria for the right correlation is based on whether it is a fluid-fluid, fluid-solid and solid-solid exchange coefficient and with the appropriate drag functions. For three-phase flow, it is absolutely important that the right selection of models are implemented. The components of the interfacial forces are shown in Equation 3.24.

$$M_i = F_d + F_{lift} + F_{wl} + F_{vm} + F_{td} + F_{ti} \qquad (3.24)$$

3.5.1 Interfacial Drag Force

The drag force, F_d is the dominant force of the interfacial transfer forces. Three interplay drag models considered in this research are liquid-gas, liquid-solid and gas-solid models. The gas-liquid-solid interface closure models is shown in Figure 4.1 and the details of the fundamentals of the mathematical equations are found in Fluent (2018) theory guide, Li and Zhong (2015), Xu et al. (2014) and Panneerselvam et al. (2009).

3.5.1.1 Gas Interface Transfer Force

The gas-liquid interface is a fluid-fluid interface exchange for which is defined as:

$$F_{D,gl} = K_{D,gl}\left(\vec{u_g} - \vec{u_l}\right) \qquad (3.25)$$

where, $K_{D,gl}$ represent the gas-liquid interface momentum exchange coefficient. This coefficient is expressed as:

$$K_{D,gl} = C_{D,lg}\frac{3}{4}\rho_l\frac{\alpha_l\alpha_g}{d_b}|\vec{u_g} - \vec{u_l}| \qquad (3.26)$$

where, $C_{D,gl}$ is the drag coefficient between the gas and liquid phases.

3.5.1.2 Liquid-Solid Interface Transfer Force

This represent the momentum transfer between the continuous phase and the solid dispersed phase. The constitutive equation is represented as:

$$K_{D,ls} = C_{D,ls}\frac{3}{4}\rho_l\frac{\alpha_l\alpha_s}{d_p}|\vec{u_s} - \vec{u_l}|\left(\vec{u_s} - \vec{u_l}\right) \qquad (3.27)$$

where, $C_{D,ls}$ is the drag coefficient between the liquid and solid phases. This takes the effect of viscosity into consideration in the formulation.

3.5.1.3 Gas-Solid Interface Transfer Force

The gas-solid interface transfer force is expressed as:

$$K_{D,gs} = C_{D,gs}\frac{3}{4}\rho_g\frac{\alpha_g\alpha_s}{d_p}|\vec{u_s} - \vec{u_g}|\left(\vec{u_g} - \vec{u_s}\right) \qquad (3.28)$$

where, $C_{D,gs}$ is the drag coefficient between the gas and solid phases. The drag coefficient, C_D, is implicit in the drag function, f_D defined in Equation 3.29. In all interface model, it is the drag function that differs among the exchange coefficient models which is inherently due to the drag coefficient (Fluent, 2018).

$$f_D = \frac{C_D R_e}{24} \tag{3.29}$$

Different drag models are available in ANSYS Fluent to calculate drag coefficients. The choice of these drag models depends on the nature of the phases and the flow stream. Some of the available drag models are:

Anisotropic drag model- This drag model is useful when the ration of normal to tangential drag is greater than 1. This type of interaction is common in vertical pipe flow.

-Schiller and Naumann (1935) model which is generally used for fluid-fluid pairs of phases.

-Morsi and Alexander (1972) model is good for wide range of Reynolds numbers but it is thought to be mostly unstable than other models.

-Grace et al. (1978) - Good for gas bubbles with different shapes and well suited for gas-liquid flows. The model uses the Eotvos and Morton numbers in its formulation.

-Tomiyama and Takamasa (1999) - This model is also well suited for gas-liquid flows and uses the Eotvos number in its formulation.

-The Universal drag laws. This law was proposed by Kolev and Kolev (2005) and is good for gas-liquid flows and applicable to non-spherical droplets and bubbles. It is however not suitable for solids. Details of these multi-phase flow drag laws can be found in ANSYS Fluent theory guide.

3.5.2   Non-Drag Forces

In CFD modelling of multi-phase flow hydrodynamic and phase transition, the non-drag forces play important roles in phasic interaction, geometrical configuration and the phase transition. Careful selection of these non-drag models are important for the development of flow field configuration. The non-drag forces are external force, lift force, wall lubrication, virtual mass force, turbulent dispersion and turbulent interaction force (Equation 3.24). Details of these forces are given in the next sections.

3.5.2.1 Lift Force

The lift force is due to the velocity gradient of the primary phase on the secondary. Often the lift force is neglected due to its small value in comparison to the drag force. It is considered in this work because the phases may separate quickly during transient flow development. The lift force is derived by Drew and Lahey (1993) and represented in Equation 3.30.

$$\vec{F}_{lift} = -C_l \rho_q \alpha_p \left(\vec{v}_q - \vec{v}_p \right) \times \left(\nabla \times \vec{v}_q \right) \tag{3.30}$$

where C_l is the lift coefficient, p is the secondary phase and q is the primary phase. There are varieties of lift coefficient models that can be used. These are: Moraga lift force model developed by Moraga et al. (1999), Saffman-Mei lift force model developed by Saffman (1965), Legendre-Magnaudet lift force developed by Legendre and Magnaudet (1998), Tomiyama lift force model developed by Tomiyama (1998) but later modified by Frank et al. (2004). In the present study, Saffman-Mei model was used for the solid-liquid, which is applicable mainly to spherical solid particles, while the Tomiyama model was used for the gas-liquid interfacial transfer force because it is applicable to larger scale deformable bubbles in ellipsoidal and spherical cap regimes.

3.5.2.2 Wall Lubrication Force

The wall lubrication force is the force that tends to push the secondary dispersed phase from the wall in a gas-liquid flows. The mathematical formulation of the wall lubrication force is shown in Equation 3.31.

$$\vec{F}_{wl} = C_{wl} \rho_q \alpha_p | \left(\vec{v}_q - \vec{v}_p \right)_\parallel |^2 \vec{n}_w \tag{3.31}$$

where C_{wl}, is wall lubrication coefficient, ρ_q is density of primary phase, α_p is the secondary phase volume fraction, $|\left(\vec{v}_q - \vec{v}_p \right)|$ is relative phase velocity component tangential to the wall surface and $\vec{n}_w$ is the unit normal pointing away from the wall. Different wall lubrication coefficients are available in literature. In this research, Tomiyama (1998) model is used for gas-liquid flows due to its superiority to other models in that it is dependent on the pipe diameter which is an advantage in this research. It does better for flows in pipe geometries by incorporating the pipe diameter and the Eotvos number. However,

the wall lubrication force is not enabled and thus not computed in gas-liquid-solid flows in this research.

3.5.2.3 Virtual Mass Force

The virtual mass force is the force exerted on the secondary (the impact of the primary phase density on the secondary phase) phase due to relative motion between the primary and secondary phases. The virtual mass force is described in Equation 3.32.

$$\vec{F}_{vm} = C_{vm}\alpha_p\rho_q\left(\frac{d_q\vec{v}_q}{dt} - \frac{d_p\vec{v}_p}{dt}\right) \tag{3.32}$$

where C_{vm} is the virtual mass coefficient which is taken as 0.5. Virtual mass force is significant when $\rho_p << \rho_q$. Therefore, the coefficient value of 0.5 was used to model the virtual mass in this research.

3.5.2.4 Turbulent Dispersion Force

For turbulent flows, the turbulent dispersion term is added to the momentum equation which accounts for the inter-phase turbulent momentum transfer. The turbulent dispersion force acts as a turbulent diffusion in dispersed flows (Fluent Theory guide, 2017). The turbulent dispersion force is the average of the interface drag term. For a dispersed phase, p, and a continuous phase q, the turbulent drag is computed with Equation 3.33.

$$K_{pq}\left(\vec{\vec{v}}_p - \vec{\vec{v}}_q\right) = K_{pq}\left(\vec{v}_p - \vec{v}_q\right) - K_{pq}\vec{v}_{dr} \tag{3.33}$$

where $K_{pq}\left(\vec{\vec{v}}_p - \vec{\vec{v}}_q\right)$ is the instantaneous drag, which represent the mean exchange between the two phases, K_{pq} is the interface exchange coefficient, $\vec{v}_p$ and $\vec{v}_q$ are the mean phase velocity vectors. The last term, $K_{pq}\vec{v}_{dr}$, is the turbulent dispersion force which is normally limited by the formulation in Equation 3.34.

$$\vec{F}_{td,q} = -\vec{F}_{td,q} = -f_{td,limiting}K_{pq}\vec{v}_{dr} \tag{3.34}$$

where $\vec{v}_{dr}$ is the drift velocity that account for the dispersion of the secondary phase due to transport by turbulent fluid motion, $f_{td,limiting}$ is the limiting factor that is used to limit the turbulent dispersion force but is often omitted in various models of turbulent dispersion force available. In this research, the Simonin and Viollet (1990) model was used

to effect the turbulence dispersion of the secondary phase due to transport by turbulent fluid notion. For three-phase flow, the turbulence dispersion modelling for solid-liquid interracial transfer ensures there is interaction between the primary liquid and secondary solid phase flow.

3.5.2.5 Turbulent Interaction Force

In the Eulerian multi-fluid VOF, the fluids are inter penetrating and hence disperse phase will influence the continuous phase and vice versa. In such situations, it is necessary to capture the interfacial transfer force from the disperse phase to the continuous phase. The turbulence interaction model can be added to the momentum equation to compute the turbulent interaction between the dispersed phases and the continuous phase. A source term is used to represent the turbulent effect of the dispersed phase.

3.6 Solids Phase Pressure

In a gas-liquid-solid flows where solid particle is one of the interacting phases, as shown in the momentum Equation 3.10, it is necessary to account for the solid pressure, p_s in the momentum equation. This is the normal pressure force due to particle motion. The solid pressure formulation developed by Lun et al. (1984) given in Equation 3.35 is used in this project. Other formulations available are that of Ahmadi and Ma (1990) and Syamlal et al. (1993a). The formulation account for the kinetic and collisional contribution in the overall solid pressure given in Equation 3.35.

$$p_s = \alpha_s \rho_s \Theta_s + 2\rho_s \Big(1 + e_{ss}\Big)\alpha_s^2 g_{0,ss}\Theta_s \tag{3.35}$$

where e_{ss} is coefficient of restitution for particle collisions, $g_{0,ss}$ is radial distribution function and Θ_s is the granular temperature. The radial distribution function, g_0, is a correction factor that modifies the probability of collisions between grains when the solid granular phase becomes dense. The radial distribution is described by nondimensional distance between the particles in a manner given in Equation 3.36.

$$g_{0,ss} = \frac{s + d_p}{s} \tag{3.36}$$

where s is the distance between grains; for dilute mixture, $s \to \infty$, and therefore $g_0 \to 1$ and vice versa. However, the formulation used in ANSYS Fluent in case of one solid phase is the formulation developed by Ogawa et al. (1980) shown in Equation 3.37.

$$g_{0,ss} = \left[1 - \left(\frac{\alpha_s}{\alpha_{s,max}}\right)^{1/3}\right]^{-1} \tag{3.37}$$

where, $\alpha_{s,max}$ is the maximum packing limit for solids given as 0.63 for one solid phase flow field. Under isothermal condition, the granular temperature Θ_s, in Equation 3.35 for the solid particle phase describes the kinetic energy of the particle's random motion due to fluctuating velocity. In other words, the granular temperature provides a measure of the energy associated with solid particles fluctuations where the intensity of the particle velocity fluctuations determines the pressure and viscosity of the solid phase. Solids viscosities and stresses are computed by simultaneously solving a fluctuating energy equation for the particulate phase. This energy is expressed in Equation 3.38. More details about the granular temperature, Θ_s is available in Huilin and Gidaspow (2003).

$$\Theta_s = \frac{1}{3}u_{s,i}^2 \tag{3.38}$$

where, $u_{s,i}$ is the ith component of the fluctuating particle velocity. On the basis of the kinetic theory of granular flow, the granular temperature is different from the temperature in the energy equation and isothermal assumption is still valid. The granular temperature is a measure of the random collisions of the particles in the flow field. The equation of the transport of solids fluctuating energy developed by Ding and Gidaspow (1990) is given in Equation 3.39.

$$\frac{3}{2}\left[\frac{\partial}{dt}\left(\alpha_s\rho_s\Theta_s\right) + \nabla.\left(\alpha_s\rho_s\vec{v}_s\Theta_s\right)\right] = \left(-p_sI + \tau_s\right) : \nabla\vec{v}_s + \nabla.\left(k_{\Theta s}\nabla\Theta_s\right) - \gamma_{\Theta s} + \varphi_{ls} \tag{3.39}$$

where $\left(-p_sI + \tau_s\right) : \nabla\vec{v}_s$ is the the generation of energy by the solid stress tensor, $\left(k_{\Theta s}\nabla\Theta_s\right)$ is the diffusion of energy, $\gamma_{\Theta s}$ is the collisional dissipation of energy, φ_{ls} is the energy exchange between the phases and $k_{\Theta s}$ is the diffusion coefficient for granular energy.

The granular temperature can be evaluated by solving the complete transport equation Equation 3.39. Alternatively, the simpler algebraic formulation can be used which assumes

that the granular energy is in a steady state and dissipates locally and the convention and diffusion distribution in the transport equation are neglected, keeping only the generation and dissipation. More details about the granular temperature can be found in Ding and Gidaspow (1990), Huilin and Gidaspow (2003) Van Wachem and Almstedt (2003) and Fluent (2018).

3.7 Frictional Pressure

Additional pressure gradient present in the multi-phase flow with solids is the frictional pressure, ∇P_{fr} term in the momentum Equation 3.10. The frictional pressure is a function of the solid concentration and depends on the radial distribution which tends to infinity at packing limit. However, this does not apply in this study as the solid concentration is diluted. Various models available for modelling frictional pressure are available in ANSYS Fluent theory guide.

3.8 Solid-Phase Shear viscosity

For multi-phase flows involving solid particles, there is additional solid stress tensor added to the solid pressure force. This is the solid shear viscosity as a result of particle momentum exchange due to translation (kinetic) and collision which is normally accounted for in the KTGF model. The solids shear viscosity comprises of three components which are the collisional part, kinetic part, and optional frictional part. Hence the summation of these viscosities gives the total overall solid particle shear viscosity in the flow stream. Thus, Equation 3.40 shows the overall solid shear viscosity. This includes the frictional viscosity which is applicable only at near packing limit.

$$\mu_s = \mu_{s,col} + \mu_{s,kin} + \mu_{s,fr} \tag{3.40}$$

where, $\mu_{s,col}$ is the collisional viscosity, $\mu_{s,kin}$ is the kinetic viscosity and $\mu_{s,fr}$ is the frictional viscosity. Equation 3.41 defines the effective viscosity for the solid phase by adding the turbulence viscosity, $\mu_{T,s}$ of the solid phase.

$$\mu_{eff,s} = \mu_{s,col} + \mu_{s,kin} + \mu_{s,fr} + \mu_{T,s} \tag{3.41}$$

3.8.1 Granular Viscosity

The granular viscosity is comprised of the Kinetic and collisional viscosities. The computation is done using the models proposed by Gidaspow et al. (1991) and Syamlal et al. (1993b) shown in the next sections.

3.8.1.1 Collisional Viscosity

Collisional viscosity is as a result of particle fluctuating movement, contact and rebound within the fluid domain. This fluctuating motion adds additional viscosity component which must be accounted for in the multi-phase computation. The model equation (Gidaspow et al., 1991; Syamlal et al., 1993b) for the collisional shear stress is expressed in Equation 3.42.

$$\mu_{s,col} = \frac{4}{5}\alpha_s\rho_s d_s g_{0,ss}\big(1 + e_{ss}\big)\left(\frac{\Theta_s}{\pi}\right)^{\frac{1}{2}}\alpha_s \tag{3.42}$$

3.8.1.2 Kinetic Viscosity

Due to the translational and fluctuating movement of solid particle in the vertical flow system, additional shear viscosity is added to the overall viscosity formulation. The Syamlal et al. (1993b) model expressed in Equation 3.43 is the default model in ANSYS Fluent used to account for this additional stresses.

$$\mu_{s,kin} = \frac{\alpha_s d_s \rho_s \sqrt{\Theta_s \pi}}{6\big(3 - e_{ss}\big)}\left[1 + \frac{2}{5}\big(1 + e_{ss}\big)\big(3e_{ss} - 1\big)\alpha_s g_{0,ss}\right] \tag{3.43}$$

while the Gidaspow et al. (1991) model is expressed in Equation 3.44.

$$\mu_{s,kin} = \frac{10\alpha_s d_s \sqrt{\Theta_s \pi}}{96\alpha_s\big(1 - e_{ss}\big)g_{0,ss}}\left[1 + \frac{4}{5}g_{0,ss}\alpha_s\big(1 + e_{ss}\big)\right]^2\alpha_s \tag{3.44}$$

3.8.2 Frictional Viscosity

The friction between the particles in a dense flow give rise to the frictional stress which is not accounted for in the solid stress viscosity model. Hence the frictional viscosity is more applicable to dense flow where contact between particles are paramount in high volume particle flows. However, due to the low solid volume fraction in this research, it

is neglected in the computational model. But where applicable, the model developed by Schaeffer (1987) can be used.

3.8.3 Granular Bulk Viscosity

The solids bulk viscosity accounts for the resistance of the granular particles to compression and expansion. Although this is neglected in this research, but where applicable, the model developed by Lun et al. (1984) can be used. This formulation is described in Equation 3.45.

$$\lambda_s = \frac{4}{3}\alpha_s^2 \rho_s d_s g_{o,ss} \left(1 + \rho_{ss}\right) \left(\frac{\Theta_s}{\pi}\right)^{\frac{1}{2}} \tag{3.45}$$

3.8.4 Turbulent Viscosity

The turbulent viscosity (shear induced eddy viscosity) is related to the turbulent kinetic energy and specific dissipation rate as described in Equation 3.57.

3.9 Turbulent Flow

Fluid flow is characterised by two types of flow description, laminar and turbulent flows which are distinguished by a non dimensional parameter called Reynolds number, R_e. Laminar flow is experienced when the fluid velocity does not change with time and the streamline is parallel to the axis. While in turbulent flow, the fluid velocity field varies significantly and irregularly in position and time. This turbulence is generated by the shear in the mean flow. The Reynolds number gives a measure of the inertia (shear) versus the viscous forces. Turbulence is described by the mean properties and statistical fluctuating components of the flow properties. This process is called Reynolds decomposition and the turbulent flow is characterise by turbulent eddies (rotational flow structures). The eddying motion leads to effective interchange of mass, momentum and heat exchange. In simple terms, the Reynolds decomposition of velocity u and scalar flow property φ is the summation of the average of the steady components and time varying fluctuating components as expressed in Equations 3.46 - 3.47

$$U = \overline{u} + u' \tag{3.46}$$

and,

$$\Phi = \overline{\varphi} + \varphi^{'} \tag{3.47}$$

where, $\overline{\varphi}$ & $\overline{u}$ are the mean values and $u^{'}$ & $\varphi^{'}$ are the fluctuating components. The Reynolds number discriminates between the viscous stress and inertia force for pipe flow. The radial distance from the pipe wall is used to determine the Reynolds number and where the inertia force is dominant further away from the wall. However, the viscous force tends to dominate at the viscous sub-layer section closer to the wall. At some arbitrary point, the viscous force and the inertia force will be equal, where both are considered to be important This layer is characterised by y^+, which is a very thin layer from the wall. Typically, $30 < y^+ < 500$, is the region within which inertia and viscous forces are equal. At this point, the shear stress, τ, is equal to the wall stress τ_w.

The basic equation used to described turbulence in fluid flow is the Navier-Stokes (NS) Equations. The NS Equations incorporate the viscous stress into the momentum equations derived from Newton's second law. Three basic approaches to model turbulence are the Direct Numerical Simulation (DNS), the Large Eddy Simulation (LES) and the Reynolds-averaged Navier Stokes (RANS) equations. The DNS approach solves the Navier-Stokes equations without averaging or approximation other than numerical discretisations whose errors can be estimated and controlled. But the amount of information contained in the turbulence eddies due to the velocity fluctuations is so enormous that the direct numerical method is highly cumbersome. Due to the turbulence fluctuation, additional turbulent shear stress called Reynolds Stress is introduced. But the time average (Reynolds-average) of the fluctuating properties would be zero. This in essence generates closure issues for the solution of the averaging of the NS Equations as the equations cannot be solved unless a method to determine the Reynolds Stresses is developed. Hence, in order to close the RANS Equations, turbulence models are use to predict the Reynolds Stress and other scalar terms to generate a usable solution to the RANS transport equations. The LES and the RANS equations solves for an accurate representation of the turbulence by approximation of the turbulence fluctuating properties by introducing different turbulence models into the transport equations motions to approximate the turbulent length and time scales. Full details of turbulence modelling

can be found in the texts of Pope (2001), Ferziger et al. (2002) and Versteeg and Malalasekera (2007),

3.9.1 Reynolds-averaged Navier-Stokes (RANS) Equations

The RANS Equations is developed from the instantaneous NS Equations where the turbulent fluctuating scales are represented as Reynolds averages of the additional normal and shear stresses. There are nine additional 3 dimensional Stresses that are added to the instantaneous NS equations that are required to be closed. These are $-\rho\overline{u'^2}$, $-\rho\overline{v'^2}$, $-\rho\overline{w'^2}$, $-\rho\overline{u'v'}$, $-\rho\overline{u'w'}$, $-\rho\overline{v'w'}$, and the representative scalar quantities for pressure, energy or species concentration, $\overline{u'\varphi'}$, $\overline{v'\varphi'}$ and $\overline{w'\varphi'}$. The general explicit 3 dimensional RANS equations for compressible and incompressible single phase fluid flow system is shown in Equations 3.48 - 3.51.

Continuity equation:

$$\frac{\partial \rho}{\partial t} + \nabla.(\rho u) = 0 \tag{3.48}$$

Momentum (Reynolds-averaged) equations:

$$\frac{(\partial \rho U)}{\partial t} + \nabla.(\rho U U) = \frac{\partial P}{\partial y} + \nabla.(\mu \nabla U) + \left(-\frac{\partial(\overline{\rho u'^2})}{\partial x} - \frac{\partial(\overline{\rho u'v'})}{\partial y} - \frac{\partial(\overline{\rho u'w'})}{\partial z} \right) + S_{Mx} \tag{3.49}$$

$$\frac{(\partial \rho V)}{\partial t} + \nabla.(\rho V U) = \frac{\partial P}{\partial x} + \nabla.(\mu \nabla V) + \left(-\frac{\partial(\overline{\rho u'v'})}{\partial x} - \frac{\partial(\overline{\rho v'^2})}{\partial y} - \frac{\partial(\overline{\rho v'w'})}{\partial z} \right) + S_{My} \tag{3.50}$$

$$\frac{(\partial \rho W)}{\partial t} + \nabla.(\rho W U) = \frac{\partial P}{\partial x} + \nabla.(\mu \nabla W) + \left(-\frac{\partial(\overline{\rho u'w'})}{\partial x} - \frac{\partial(\overline{\rho v'w'})}{\partial y} - \frac{\partial(\overline{\rho w'^2})}{\partial z} \right) + S_{Mz} \tag{3.51}$$

where, U, V, W and P are the mean components and the u', v', w', p' and φ' are the fluctuating components

Similarly, the scalar transport equation is represented in Equation 3.52

$$\frac{\partial(\rho \Phi)}{\partial t} + \nabla.(\rho \Phi U) = \nabla.(\Gamma_\Phi \nabla \Phi) + \left(-\frac{\partial(\overline{\rho u'\varphi'})}{\partial x} - \frac{\partial(\overline{\rho v'\varphi'})}{\partial y} - \frac{\partial(\overline{\rho w'\varphi'})}{\partial z} \right) + S_\Phi \tag{3.52}$$

The averaging process of the random shear stresses in the above equations would be unclosed and hence no solution can be obtained. Therefore, these additional random fluctuating stresses are approximated using various turbulence models in order to close the RANS Equations. These turbulence models are discussed in section 3.10. More details about the RANS Equations are found in Pope (2001) and Versteeg and Malalasekera (2007).

3.9.2 Direct Numerical Simulation (DNS)

The DNS approach is used to solve the Navier-Stokes equations, by resolving all the scales of motion with initial and boundary conditions appropriate to the flow considered Pope (2001). It is more suited for moderate Reynolds number flow and becomes increasingly (at the cube of Reynolds number) complex at high Reynolds number and thus requires high computer resources such that it may become impracticable to implement in industrial scale. However, when feasible, the DNS provides the most accurate solution to the NS equations by resolving all scales in the flow fluctuations. The DNS is useful in validating experimental results and could be used to extract useful statistics that are not possible to obtain from experiment.

3.9.3 Large Eddy Simulation (LES)

Due to the complexity of the turbulence modelling, there is no fit for all approach that is applicable to all application due to large and small eddies behaviour. Small eddies are isotropic and have similar attributes while large eddies are anisotropic and depends on the pipe geometry and other external factors. Large eddies extract energy from the mean flow and transfer to the small eddies. In the application of the LES approach, time averaging is not used, rather the large eddies are filtered out and directly represented whereas the small eddies are separated and modelled. The filtered small eddies are solved by the eddy viscosity model while the large eddies are solved numerically. The LES simulation would require smaller time step and hence it is more computationally demanding than the RANS method. More details about the LES are found in Pope (2001)

3.10 Turbulence Flow Models

The modelling of turbulence in multi-phase flow is very complex. However, there are various turbulence models available which can be applied in ANSYS Fluent to approximate the turbulent fluctuating properties. These are: two-equation Models (k-ε and k-ω), and the seven-equation Reynolds Stress Model (RSM). These models are classified based on the number of additional transport equations to be solved, where the RSM has the highest number of additional transport equations (Versteeg and Malalasekera, 2007). The k-ε model, first derived by Launder and Spalding (1972), has been modified and tested by various researchers and found to be very stable but most suitable for fully turbulent flows. It considers the molecular viscosity of the phases and accurate near wall treatment is required. Hence, Wilcox et al. (1998) developed the Standard k-ω, BSL k-ω and SST k-ω models which incorporate turbulence damping feature to model high turbulent flows correctly. For gas-liquid flows with large bubble, it is important to resolve the high velocity gradient at the interface between two fluids which results in high turbulence generation. Hence, turbulence damping is required in the interfacial area to compute such flows correctly at high superficial velocity.

In the k-ω turbulence model, this turbulence damping term is summed over all the phases and added as a source term to the k-ω equation (Dai et al., 2013) hence, this turbulence model is used in this research. The k-ω model does exceedingly well in semi-annular and annular flow simulation at high flow rate even without the turbulence damping feature. The k-ω model has gone through various modification by the addition of the production terms to the kinetic energy and the specific dissipation terms for improved accuracy. The transport equations for the standard k-ω model is expressed in Equations 3.53 - 3.54:

$$\frac{\partial}{\partial_t}\left(\rho\kappa\right) + \frac{\partial}{\partial_{Xi}}\left(\rho\kappa u_i\right) = \frac{\partial}{\partial_{Xj}}\left(\Gamma_\kappa \frac{\partial\kappa}{\partial_{Xj}}\right) + G_\kappa - Y_\kappa + S_\kappa \tag{3.53}$$

And,

$$\frac{\partial}{\partial_t}\left(\rho\omega\right) + \frac{\partial}{\partial_{Xi}}\left(\rho\omega u_i\right) = \frac{\partial}{\partial_{Xj}}\left(\Gamma_\omega \frac{\partial\omega}{\partial_{Xj}}\right) + G_\omega - Y_\omega + S_\omega \tag{3.54}$$

where: G_κ is the generation of turbulent kinetic energy due to mean velocity gradient, G_ω is the generation of the specific dissipation rate, $\Gamma_{\kappa,\omega}$ are the effective diffusivities,

$Y_{\kappa,\omega}$ are the dissipations due to turbulence and $S_{\kappa,\omega}$ are the user define source terms. The effective diffusivities are calculated from Equations 3.55 - 3.56

$$\Gamma_\kappa = \mu + \frac{\mu_t}{\sigma_k} \tag{3.55}$$

$$\Gamma_\omega = \mu + \frac{\mu_t}{\sigma_\omega} \tag{3.56}$$

where: $\sigma_{k,\omega}$ are the turbulent Prandtl numbers in the k-ω model. The eddy viscosity is expressed as in Equation 3.57 with optional damping factor, α^*.

$$\mu_t = \alpha^* \frac{\rho k}{\omega} \tag{3.57}$$

where, μ_t, is the turbulent viscosity, k is turbulent kinetic energy and ω is the specific dissipation rate. The turbulent kinetic energy is defined as the variance of the fluctuations in the velocity $(\frac{m^2}{s^2})$, while the ω is the turbulence frequency defined in Equation 3.58 and is dimensionless in value.

$$\omega = \frac{\varepsilon}{\kappa} \tag{3.58}$$

The α^* is the dampening coefficient for the turbulent viscosity that causes a low-Reynolds number correction expressed in Equation 3.59.

$$\alpha^* = \alpha^*_\infty \left(\frac{\alpha^*_0 + Re_t/R_k}{1 + Re_t/R_k} \right) \tag{3.59}$$

where as : $Re_t = \frac{\rho K}{\mu \omega}$; $Rk = 6$; $\alpha^*_0 = \frac{\beta_i}{3}$ and $\beta_i = 0.072$. In case of high Re, $\alpha^* = \alpha^*_\infty = 1$ From Equations 3.53 - 3.54, the production terms are defined as follows:

$$G_\kappa = -\rho \overline{u'_i u'_j} \frac{\partial u_j}{\partial x_i} \tag{3.60}$$

Using the Boussinesq hypothesis, G_κ can be evaluated with Equation 3.61.

$$G_\kappa = \mu_t S^2 \tag{3.61}$$

where S = modulus of the mean rate-of-strain tensor defined in Equation 3.62.

$$S \equiv \sqrt{2 S_{ij} S_{ij}} \tag{3.62}$$

and,

$$G_\omega = \alpha \frac{\omega}{K} G_\kappa \tag{3.63}$$

It can be seen that the production of ω is a function of G_κ. whereas,

$$\alpha = \frac{\alpha_\infty}{\alpha^*} \left(\frac{\alpha_0 + Re_t/R_\omega}{1 + Re_t/R_\omega} \right) \tag{3.64}$$

where, $R_\omega = 2.95$ and $\alpha = \alpha_\infty = 1$ for high Reynolds form of k-ω.

From Equations 3.53 - 3.54, the kinetic dissipation terms are defined as follows:

$$Y_k = \rho \beta^* f_{\beta^*} K \omega \tag{3.65}$$

where, for $X_k \leq 0$

$$f_{\beta^*} = 1 \tag{3.66}$$

and for $X_k > 0$

$$f_{\beta^*} = \frac{1 + 680 X_\kappa^2}{1 + 400 X_\kappa^2} \tag{3.67}$$

but,

$$X_k \equiv \frac{1}{\omega^2} \frac{\partial K}{\partial X_j} \frac{\partial \omega}{\partial X_j} \tag{3.68}$$

and,

$$\beta^* = \beta_i^* \left[1 + \zeta^* F(M_t) \right] \tag{3.69}$$

$$\beta_i^* = \beta_\infty^* \left(\frac{4/15 + (Re_t/R_\beta)^4}{1 + (Re_t/R_\beta)^4} \right) \tag{3.70}$$

From Equations 3.53 - 3.54, the specific dissipation term, ω is defined as follows:

$$Y_\omega = \rho \beta f_\beta \omega^2 \tag{3.71}$$

where,

$$f_\beta = \frac{1 + 70 X_\omega}{1 + 80 X_\omega} \tag{3.72}$$

and,

$$X_\omega = \left| \frac{\Omega_{ij} \Omega_{jk} S_{ki}}{(\beta_\infty^* \omega)^3} \right| \tag{3.73}$$

and,

$$\Omega_{ij} = \frac{1}{2} \left(\frac{\partial u_i}{\partial x_j} - \frac{\partial u_j}{\partial x_i} \right) \tag{3.74}$$

$$\beta = \beta_i \left[1 - \frac{\beta_i^*}{\beta_i} \zeta^* F(M_t) \right] \tag{3.75}$$

where, S_{ij} defined as the mean stress-strain tensor given as:

$$S_{ij} = \frac{1}{2} \left(\frac{\partial u_j}{\partial x_i} + \frac{\partial u_i}{\partial x_j} \right) \tag{3.76}$$

where, $\zeta^* = 1.5$, $R_\beta = 8$, $\beta_\infty^* = 0.09$, $\alpha_\infty^* = 1$, $\alpha_\infty = 0.52$, $\alpha_0 = \frac{1}{9}$, $\beta_i = 0.072$, $R_k = 6$, $\alpha_k = \alpha_\omega = 2.0$.

For high Reynolds number flow in k-ω modelling, $\beta_i^* = \beta_\infty^*$. $F(M_t)$, the compressibility function is neglected by default in Fluent.

3.10.1 Turbulence Damping

The k-ω model has the turbulence damping option which is used to dampen high turbulence in the interfacial area of free surface flows due to high velocity gradient between the two fluids. This is needed to model the interfacial area correctly. In this method, an additional source term is added to the specific dissipation rate (ω) Equation 3.54. This source term is defined in Equation 3.77.

$$S_\omega = S_i = A_i \Delta n \beta \rho_i \left(\frac{D_f 6 u_i}{\beta \rho_i \Delta n^2} \right)^2 \tag{3.77}$$

where,

A_i = interfacial area density for phase i, which is calculated with Equation 3.78.

$$A_i = 2\alpha_i |\nabla \alpha_i| \tag{3.78}$$

where,

Δn = cell height normal to the interface, $\beta = \kappa_\omega$ computes the closure coefficient of destruction term which is equals to 0.075, D_f = the damping factor which is set in Fluent with a default of 10, α_i, = the volume fraction of phase i, $|\nabla \alpha_i|$ = the magnitude of gradient of volume fraction of phase i, μ_i and ρ_i are the viscosity and density of the respective phases.

SOLUTION TECHNIQUE OF GOVERNING EQUATIONS

This chapter presents the solution technique used for the computation of multi-phase flow hydrodynamics in large diameter vertical pipe. The flow structures and dynamics of a large diameter pipe flow are proven to be different from that of a small diameter pipe (Schlegel et al., 2016, 2012). This research is focused on larger vertical pipe which is found to be mostly used in the oil & gas installation and the process industries. Pipe size used in the wellbore are typically 80-250mm which are classified as large diameter pipe (Table 2.1). Initial computation was conducted for two-phase gas-liquid flows which was validated with the experimental data set of Omebere-Iyari et al. (2007b). Thereafter, sand particles were introduced to the flow scheme to determine the impact of a third solids-phase on the flow hydrodynamic parameters. The governing equations and closure laws discussed in chapter 3 were applied in the solution scheme and solved by ANSYS Fluent CFD computational tool. The benchmarked experimental work of Omebere-Iyari et al. (2007b) was conducted on a vertical pipe with an internal diameter of 189mm and a height of 52m at 20 and 90 bar. However, due to the limitation of CFD, only a section of the pipe was simulated, considering the entrance length limitation. Besides, only the results for the 20bar pressure was computed and validated in this research.

4.1 Solution Method

The Euler-Euler and Euler-Euler-Euler approaches were adopted in this research in which the phases were inter-penetrating continua in a manner depicted in Figure 4.1 (Li and Zhong, 2015), and implemented in ANSYS Fluent. In this approach, the continuous phase

interacts with the two secondary phases and the secondary phases also interact with each other. The liquid is the primary continuous phase while the gas and solids phases are considered as the secondary phases. Accurate solution of multi-phase gas-liquid-solid flow dynamic depends on selecting the appropriate models for the turbulence and interfacial forces. Detailed description of these interfacial forces and turbulence models were given in chapter 3.
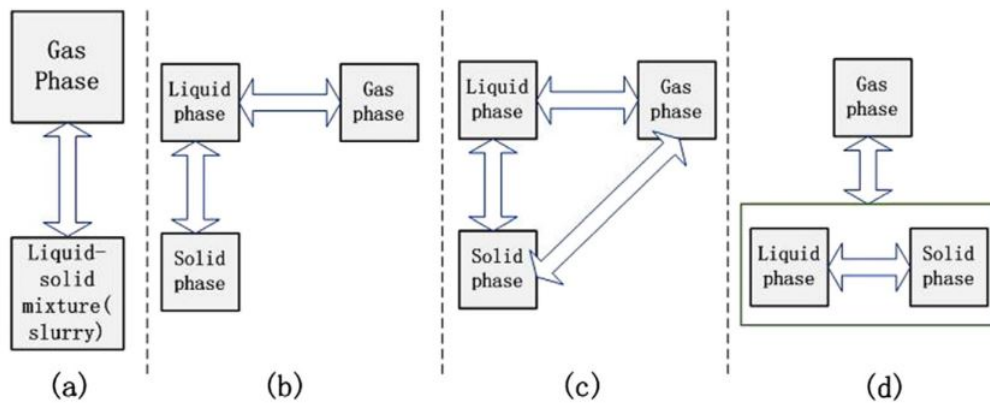
Figure 4.1: Gas-Liquid-Solid-Interface Momentum Model (Li and Zhong (2015)

The numerical scheme selected for this research, with the turbulence and interfacial forces make up the *Solution Technique*. The predictions of this *Solution Technique* were validated with published experimental data set. The k-ω turbulence model was used in this investigation because of its stability with high velocity flows, while all the interfacial forces which include drag force, virtual mass, wall lubrication, lift force, turbulence dispersion and turbulence interaction were computed in this study. The solids stress was computed using the kinetic theory of granular flow (KTGF). The bubble coalescence and break-up were simulated by implementing the interfacial area concentration equation postulated by Hibiki and Ishii (2000).

4.1.1 Solution Domain and Boundary Conditions

This research aim and objectives are to be achieved through sets of CFD simulations covering range of multi-phase flow encountered in convectional oil & gas and process industries. Initial analysis is conducted for two phase gas-liquid flows which mimic option (a) in Figure 4.1 in the Eulerian framework. The experimental set-up of Omebere-Iyari

et al. (2007b) is used to validate the model. Their experiment was performed in a 52m, 189mm diameter vertical pipe at 20 and 90 bar in order to determine the flow pattern characteristics in large diameter pipe at high pressures. Only a section of the pipe, 5.67m high and diameter of 189mm at a pressure of 20 bar was modelled based on the entrance length. The hydrodynamic entrance length was calculated from Equation 4.1 (Yunus, 2010) developed for small diameter pipe.

$$\frac{L_e}{D} = 4.4(R_{em})^{1/6} \tag{4.1}$$

where, L_e is the theoretical entrance length at which the flow should have been fully developed, D is the pipe diameter and R_{em} is the mixture Reynolds number. The calculated L_e is 5m, hence all data collection points were at this height. Earlier on, Schlegel et al. (2012) stated that in large diameter pipe, the available development length is much shorter than in small diameter pipe.

The solution domain is a 3-dimensional vertical cylindrical pipe of 5.67m with a diameter of 189mm. The sketch of the domain used in this research is shown in Figure 4.2. The geometry was generated by ANSYS Design Modeller. This geometry was then exported to ANSYS ICEM meshing tool which was used to generate a uniform O-type structured hexahedral mesh. The O-grid mesh allows for refining the meshes closer to the wall which prevents singularity at the center of the pipe. Uniform number of cells were chosen along the axis of the pipe. Two velocity inlet boundary conditions for gas and liquid were used while the outlet was pressure controlled at atmospheric condition. The pipe wall was modelled as stationary no slip boundary condition. Standard initialisation was used to set up the initial condition of the pipe to be filled with liquid and at the specified liquid superficial velocity for each of the cases investigated.

4.1.2 Test Case and Parameters

Literature survey carried out in chapter 2 shows that few attempts have been made to characterise the dynamics of gas-liquid flow in large diameter pipe. Nonetheless, there are lack of agreements on the measurements methods, predictions and conclusion of the flow dynamics and thus detailed understanding of the flow mechanism is still lacking. Hence this detailed understanding of the complex flow hydrodynamics in large diameter
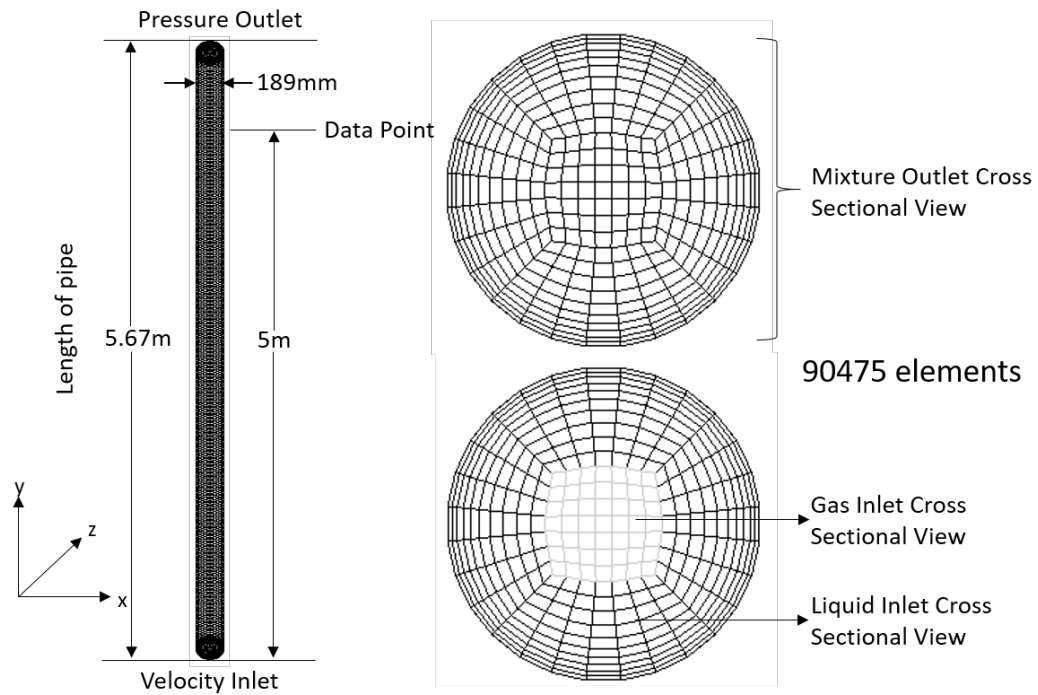
Figure 4.2: Solution Domain & Boundary Conditions

pipe is required. In this research, data set of Omebere-Iyari et al. (2007b) two-phase flow experiment in large diameter vertical pipe was used as the case study for the purpose of validation of the CFD results and flow pattern analysis. Thereafter, the CFD model was extended to simulate three-phase gas-liquid-solid flow to study the effect of sand and particle entrainment in the flow field.

Omebere-Iyari et al. (2007b) experimental setup consists of a 52m vertical pipe with a diameter of 189mm. This is categorised as large diameter pipe according to Table 2.1 developed from Equation 2.1. The test fluid were nitrogen gas and naphtha liquid which have similar properties to oil and gas fluid. Details of the fluid properties are shown in Table 4.1. Due to the limitation of the computing power available for the computational fluid dynamics (CFD) modelling, only 5.67m (based on Equation 4.1) of the pipe length was simulated.

Table 4.1: Fluid Properties

Press (Bar)	Tempt (^oC)	Density (kg/m^3)			Viscosity (Pa.s)			Diam. (μm)	Surf. Tens (n/m)
System		Gas	Liquid	Solid	Gas	Liquid	Solid	Solid	Liquid
20	30	23.4	702.3	2500	1.77E-05	3.59E-04	KTGF	250	0.0185

The superficial velocities of the data set used for this research were extracted from the experimental work of Omebere-Iyari et al. (2007*b*) which covers the full range of the flow pattern spectrum from bubbly flow to annular flow regimes. CFD computation was performed for gas superficial velocities of 0.088 to 14.782 m/s and liquid superficial velocities range of 0.00360 to 4.1255 m/s. Details of these gas and corresponding liquid superficial velocities for each run are shown in Table 4.2. These superficial velocity values cut across the entire flow pattern spectrum from bubbly flow to annular flow according to the experimental report.

4.1.3 Mesh Generation and Independence Study

The outcome of CFD computation depends largely on the selection of appropriately tuned numerical scheme and, specifically on the specification of the mesh density and shape. In this research, the mesh sensitivity study was done to ascertain the optimum grid requirements to achieve optimum solution convergence, at optimum computational time. Grid sensitivity analysis were carried out on 57,204 cells, 90,475 cells, 158,364 cells and 229,100 cells. Parametrization of the grid sizes was done considering the reduction of the cell height to the maximum cell size as shown in Table 4.3. The surface cross-sectional view of these cells are shown in Figure 4.3. The optimal cell model of 90,475 cells was selected based on the simulation time and accuracy of the matched results.

4.1.4 Model Setup

The model set up consist of a two-phase and three-phase Eulerian framework with multi-fluid VOF and k-ω viscous model in a manner similar to options (a) and (c) of Figure 4.1. The multi-fluid VOF model provides the framework to couple the VOF and the Eularian multi-phase model. The VOF model can compute two immiscible fluids to resolve the large scale (non penetrating) interfaces while, the Eulerian model compute the interpenetration interfaces. Full details of the multi-fluid VOF are found in Fluent (2018). Two volume fraction formulation, explicit and implicit are available in ANSYS Fluent tool. The former is non iterative and depends on the courant-based stability criteria while the latter is iterative and does not depends on the courant number. The

Table 4.2: Fluid Superficial Velocities (from Omebere-Iyari et al. (2007b))

Gas Superficial Velocity (m/s)	Liquid Superficial Velocity (m/s)	Gas Superficial Velocity (m/s)	Liquid Superficial Velocity (m/s)
0.088	0.047	0.975	0.009
0.091	0.502	0.991	0.004
0.092	0.050	1.003	0.306
0.092	0.004	1.283	0.295
0.092	0.009	1.451	0.491
0.100	0.050	1.468	0.004
0.147	0.050	1.478	0.009
0.183	0.660	1.488	0.048
0.199	0.071	1.928	0.999
0.201	0.095	1.974	0.646
0.210	0.049	2.420	0.009
0.277	0.072	2.434	0.094
0.291	0.096	2.454	0.047
0.293	0.004	2.488	0.290
0.310	0.009	2.945	0.998
0.336	0.096	3.911	4.085
0.387	0.004	3.950	0.290
0.390	0.009	3.953	0.095
0.392	0.095	4.000	0.050
0.393	0.048	4.859	0.652
0.395	0.147	4.967	3.025
0.400	0.050	4.974	0.501
0.488	0.009	5.844	0.996
0.490	0.097	7.891	0.995
0.491	0.047	8.004	4.126
0.498	0.193	9.793	0.642
0.501	1.017	9.796	0.476
0.506	0.143	9.800	0.289
0.590	0.070	9.930	4.021
0.682	0.295	9.942	0.994
0.683	0.096	9.989	0.004
0.693	0.193	13.722	4.117
0.770	3.084	13.832	2.976
0.834	0.291	13.849	0.641
0.972	0.647	14.095	0.047
0.972	0.498	14.782	0.009
0.973	0.096	0	0

implicit formulation requirements can accommodate higher time step and has been proven to be more stable in three-phase gas-liquid-solid flow computation and is thus, used in this research. However, it requires higher order transient formulation for the volume fraction

Table 4.3: Mesh Sensitivity Data

Number of Cells	Maximum size	Height	Height ratio
57204	0.022	0.0027	1.2
90475	0.022	0.0022	1.2
158364	0.022	0.0018	1.2
229100	0.022	0.0015	1.2

(a) 57204   (b) 90475

(c) 158364   (d) 229100
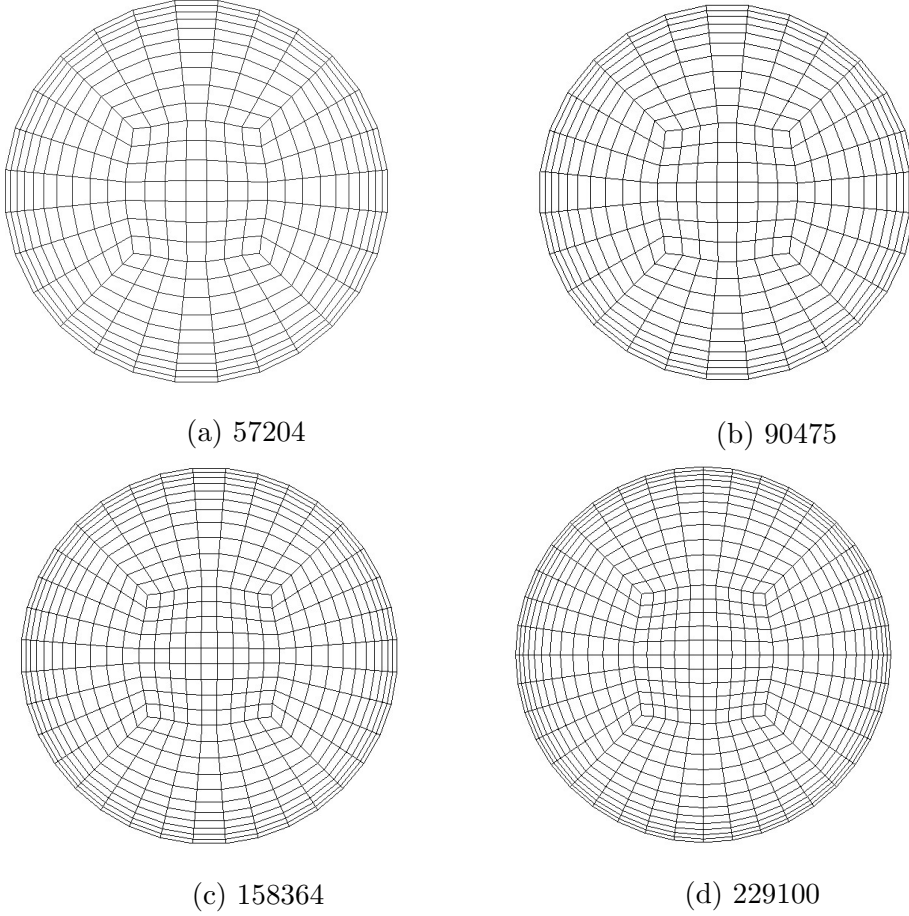
Figure 4.3: Cross Sectional View of Mesh Sensitivities

computation. The implicit volume fraction discretisation is achieved using Equation 4.2

$$\frac{\alpha_q^{n+1}\rho_q^{n+1} - \alpha_q^n\rho_q^n}{\Delta t}V + \sum_f \left(\rho_q^{n+1}U_f^{n+1}\alpha_{q,f}^{n+1}\right) = \left[S_{\alpha q} + \sum_{p=1}^n \left(\dot{m}_{pq} - \dot{m}_{qp}\right)\right]V \qquad (4.2)$$

where,

$n + 1$ = index for current time step, n = index for previous time step, α_q^{n+1} = cell value of volume fraction at time step $n + 1$, α_q^n = cell value of volume fraction at time step

n, $\alpha_{q,f}^{n+1}$ = face value of the qth volume fraction at time step $n + 1$, U_f^{n+1} volume flux through the face at time step $n + 1$, and V = cell volume. The implicit computation of the scalar equation for the secondary phase volume fraction is solved iteratively. In this sense, the current time step volume fraction does not only depend on the volume fraction but also on other quantities within the time and the face fluxes are interpolated. The main difference between the implicit and explicit formulation is that the explicit computation does not require iteration at the current time step but simply use the known quantities from previous time step.

The selection of the interface model determines the volume fraction spatial discretisation scheme available for selection. Due to the spectrum of this research, the sharp/dispersed scheme was chosen for the interface modelling. The sharp/dispersed model allows distinct interface and interpenetration of the phases. This option is able to capture mildly sharp and diffused interfaces. On the sharp/dispersed scheme, only Compressive and HRIC scheme are available for volume fraction spatial discretisation, both of which uses the algebraic formulation. There is no evidence if one is better than the other so, selection of the Compressive scheme used in this research is a matter of choice.

4.1.5 Solver Numerical Scheme

A three dimensional (3D) transient model is developed to simulate the local hydrodynamics of gas-liquid and gas-liquid-solid flows in large diameter vertical pipe using a CFD method. The numerical governing equations were discretized and solved using the advanced Phase-Coupled SIMPLE (PC-SIMPLE) solver technology of Fluent in an Eulerian frame of reference with multi-fluid VOF and implicit volume fraction formulation. The compressive implicit formulation which is independent of the Courant-based stability criterion, was chosen to avoid divergence and allows use of larger time step. The sharp/dispersed interface modelling was selected which was meant to capture the mildly sharp interfaces in the flow scheme. Table 4.4 shows the numerical schemes selected for each variable in this research.

Table 4.4: Solver Numerical Scheme

Variables	Scheme
Solver	Pressure Based
Pressure velocity Coupling	Phase Coupled Simple
Momentum	Second Order Upwind
Volume Fraction	Compressive Implicit
Turbulent Kinetic Energy	Second Order Upwind
Specific Dissipation Rate	Second Order Upwind
Transient Formulation	First Order implicit

4.1.5.1 Pressure Based

In ANSYS Fluent, the density based and the pressure based solvers are available. In the density based solver, the density is obtained from the continuity equation and the pressure field is obtained from equation of state (EoS). While the pressure based solver uses the projection algorithm in which the constraint of mass and momentum conservation is resolved by solving a pressure or pressure correction equation derived from the continuity and momentum equations in a manner that the pressures corrects the velocity field to meet the continuity conditions. The solution process is iterative until a converged solution is obtained from the non linear governing equations. The pressure based solver was selected for this research because it is more suited for incompressible multi-phase flow in low speed. Both methods however use the control volume approach to discretise the conservation equations.

4.1.5.2 Phase Coupled SIMPLE

When using the Eulerain modelling methodology for multi-phase flow computation, only phase coupled SIMPLE (segregated) and the coupled algorithm are available. The segregated approach used in this research uses a sequential iteration to achieve a converged solution. This approach is simple and does not require large memory because the segregated solution is stored one at a time. The coupled scheme solves the coupled pressure based continuity and momentum equations together and thus better accuracy

may be achieved. However, the coupled scheme is more time consuming and takes more memory space. On the other hand, segregated solution technique is time efficient when compared to the coupled method and also gave a reasonably faster solution convergence in this research. More details about the segregated and the coupled solution technique are available in Fluent (2018).

4.1.5.3 Second Order Upwind

There are several discretisation schemes available in ANSYS Fluent that are suitable for various purposes and scenarios. By default, Fluent scalar values, φ are stored at the cell centers, but the face values, φ_f are required for the transportation and must be interpolated from the cell centre values. The methodology to achieve this interpolation is called the Upwind technique. In the Upwind scheme, the scalar value at face f, φ_f is derived from the scalar quantities that are in the upstream (Upwind) to the flow direction normal to the face. The First Order Upwind simply takes the cell face value to be equal to the upstream centre value all through. This is simply an approximation technique. On the other hand, with the Second Order Upwind technique, the face values are linearly reconstructed through a Taylor series expansion of the cell centred solution about the centroid using Equation 4.3.

$$\varphi_{f,SOU} = \varphi + \nabla\varphi.\overrightarrow{r} \tag{4.3}$$

where, φ is the cell centred value, $\nabla\varphi$ is the gradient of the upstream scalar value, $\overrightarrow{r}$ is the displacement vector from the upstream cell centroid to the face centroid.

The Second-Order Upwind (SOU) scheme provides better solution accuracy than the First-Order Upwind (FOU). However, the SOU may lead to numerical divergence hence, the computation was started with FOU and then switched to SOU when the simulation was stabilised. The gradient, $\nabla\varphi$ was computed using the Least Squares Cell based gradient computation technique. This gradient is easier to compute with this method than the Node/Cell based Green-Gauss method. Other Upwinding schemes are the Quick, Power Law and Third-Order MUSCL discretisation schemes but, these are more suited for rotating and swirling flows and do not provide better solution result for multi-phase flows. The Second-Order Upwind scheme was selected for the momentum,

turbulent kinetic energy, specific dissipation rate, energy and interfacial area concentration (IAC) computation for this study. The transient formulation is by default computed with first-order implicit technique.

4.1.5.4 Solution Control

The discretised equations of mass and momentum solved in a computational domain are inherently nonlinear. Hence the scalar variable, φ will normally increase too much and therefore, it is required to be controlled by sets of variable factors that are used in the iterative algorithm to reduce the change ($\Delta\varphi$) of φ to ensure the stability and convergence of the numerical solution. Thus the new variable φ in a cell depends on the older variable, φ_{old}. The under relaxation factor, α is set for each variables such that the relationship influences the variable φ as defined in the relation described in Equation 4.4. This method of under relaxation of variables is also called explicit relaxation.

$$\varphi = \varphi_{old} + \alpha\Delta\varphi \tag{4.4}$$

On the other hand, the under relaxation of equations called implicit relaxation can also be used in a pressure based solver to stabilise the convergence of the non-linear iterations. In this method, a selective amount of φ is introduced into the discretised equations. More details of this method is found in Fluent (2018).

In this research, the explicit relaxation was used to stabilize the residuals for effective convergence. Due to the complexity of three-phase gas-liquid-solid flow, two sets of factors were used, one set for two-phase gas-liquid and another for three-phase gas-liquid-solid flows. The default under relaxation factors in Fluent were adjusted for optimal solution. Details of these factors are shown in Table 4.5. Another factor that was used to achieve stabilisation is the time step size. Reasonable care was taken to set the optimal time step to as large as practically possible for quicker results. This is the advantage of compressive implicit formulation earlier mentioned. The value of 0.001 sec was used to ensure stability of the numerical results.

Table 4.5: Under Relaxation Parameters

Variables	Factors
Pressure	0.3
Density	1
Momentum	0.5
Volume Fraction	0.5
Granular Temperature	0.2
Turbulent Kinetic Energy	0.8
Turbulent Dissipation Rate	0.8
Turbulent Viscosity	1
Energy	1
Inter-facial Area Concentration	0.3

4.1.5.5 Interface Transfer Terms

Considering the model used in this research, the interaction between the phases are described in the momentum conservation Equations 3.8 - 3.10, where the interfacial transfer forces are represented by the interaction terms $M_{i,l}$, $M_{i,g}$, and $M_{i,s}$. The model option c in Figure 4.1 indicates that the interactions or interface exchange are fluid-fluid (liquid-gas), fluid-solids (liquid-sand) and fluid-solids (gas-sand) interface exchanges that are inter-penetrating, which means that the interaction is two ways for each of the fluid. The interface exchange momentum terms in Equations 3.8 - 3.10 have detailed meaning which will be illustrated in the next sections. In ANSYS Fluent, in addition to the interface exchange models described in Chapter 3, the model exchange coefficients selected to model the interfacial transfer determines the success of the computation.

4.2 The Drag and Non-Drag Laws

The interaction of the phases and the transfer of momentum are achieved by drag and non-drag laws. There are different drag law models available in ANSYS Fluent for different fluid models. These Drag laws are either isotropic or anisotropic. Anisotropic drag law is

needed if there is a higher drag in the normal direction to the interface and lower drag in the tangential direction to the interface. This is more suited for multi-phase phase flow simulation in vertical pipe and is thus used in this research for gas-liquid flow interface transfers. While Schiller and Naumann (1935) model was used for the fluid-solid interface force transfers.

Invoking the momentum Equations 3.8 - 3.10, the explicit definition of the interface force terms are:

For fluid-fluid,

$$M_{i,f} = \sum \left(F_{gl} + \dot{m}_{gl}V_{gl} - \dot{m}_{lg}V_{lg} \right) + \left(F_{lift} + F_{wl} + F_{vm} + F_{td} + F_{ti} \right) \qquad (4.5)$$

and for fluid-solids,

$$M_{i,s} = \sum \left(F_{fs} + \dot{m}_{fs}V_{fs} - \dot{m}_{fs}V_{fs} \right) + \left(F_{lift} + F_{wl} + F_{vm} + F_{td} + F_{ti} \right) \qquad (4.6)$$

Where the first term in the bracket on the right-hand side is the drag force while the second term in bracket on the right hand side is the non-drag forces defined earlier in this thesis. Because there is no mass transfer, the drag force reduces to $F_{D,gl}$ which is equal to Equation 3.25 and the $K_{D,gl}$, is the gas-liquid interface momentum exchange coefficient, also defined in Equation 3.26. The drag and non-drag coefficient are what make the difference in the drag models and non drag models. Hence,

$$M_i = F_D + F_{lift} + F_{wl} + F_{vm} + F_{td} + F_{ti} \qquad (4.7)$$

The drag force is the most dominant of all the interfacial forces. The interaction is a three-way coupling as shown earlier in Figure 4.1 and inter-penetrating.

In this research, the liquid, gas and solid phases are coupled such that they are continually inter-penetrating. The non-drag forces are modelled in this research to account for all variables that contribute to the interfacial forces. Because this research scope covers wide range of flow conditions, all variables are included in the computation to ensure that any exclusion does not lead to wrong results. Details of the drag and non-drag laws model selection in Equations 4.5 - 4.6 are given in subsections 3.5.1 - 3.5.2. While the summary of the selected models is shown on Table 4.6. The importance of the granular temperature and the choice of algebraic model was initially described in section section 3.6.

Table 4.6: Selected Drag and Non Drag Models

Variables	Models selected
Granular viscosity	Syamla-Obrien 1987
Granular temperature	Algebraic
Solid pressure	Lun et al 1984
Virtual mass	Constant (0.5)
Drag (gas-liquid)	Anisotropic
Drag (solid-gas)	Schiller-Naumann 1935
Drag (solid-liquid)	Schiller-Naumann 1935
Lift (gas-liquid)	Tomiyama 1998
Lift(solid-liquid)	Saffman-mei 1965
Wall lubrication (gas-liquid)	Tomiyama et al 1998
Turbulent dispersion (gas-liquid)	Simonin and Viollet 1990
Turbulent dispersion (solid-liquid)	Simonin and Viollet 1990
Turbulence interaction (gas-liquid)	Trosko-hassan 2001
Turbulence interaction (solid-liquid	non

4.3   Phase Property Set-up

The work of this thesis is split into 2 multi-phase flow cases which are: two-phase gas-liquid and three-phase gas-liquid-solid flows. In either case, the liquid-phase is the continuous phase while the gas and solid are the secondary dispersed phases. In addition to the drag and non-drag laws explained in previous section, the secondary phase fluid property set-up is relevant to the success of the computation. The Eulerian multifluid VOF set-up used in this research is unique and is designed to produce the fluid geometrical configuration that transition from bubbly to annular flow regime spectrum. The following sections give the overview of the setup used for the secondary phases in this research.

4.3.1 Gas Phase Set Up

4.3.1.1 Interfacial Area Concentration

Accurate set up of the gas-phase determines the success of multi-phase flow computation. In this research, the interfacial area transport model described in Equation 3.23 was enabled in the phase property setup. In the setup, the size distribution of the gas phase is meant to change according to the evolution of the phase geometrical configuration. The changes in the discrete phase size distribution is due to the following: (1) Growth, resulting from the mass transfer between the phases when this is included in the model setup, (2) Expansion, due to pressure variations, agglomeration of the discrete bubbles and breakage of the bubbles and (3) Nucleation of the discrete bubble. Nucleation is the source term that determines rate of changes of formation of the secondary phase. These mechanisms were computed with the interfacial area concentration equation. The IAC which was originally developed for bubbly flow but has been proven to be adaptable to other flow patterns configurations. Invoking the IAC formulation in Equation 3.23,

$$\frac{\partial\left(\rho_g X p\right)}{\partial t} + \nabla.\left(\alpha_g \vec{u}_g X_p\right) = \frac{1}{3}\frac{D\rho_q}{Dt}X_p + \frac{2}{3}\frac{\dot{m}_g}{\alpha_g}X_p + \rho_g\left(S_{RC} + S_{WE} + S_{TI}\right)$$

the agglomeration (coalescence) of the secondary phase is represented by two source term variables; S_{RC}, due to random collision and S_{WE}, due to wake entrainment. The destruction of the bubbles is computed by the turbulence impact sink term S_{TI}. There are two models that account for the source and sink term in the IAC equation. These models are the Hibiki and Ishii (2000) & Ishii and Kim (2001) models. The Hibiki-Ishii model does not account for the wake entrainment while the Ishii-Kim model does account wake entrainment in their formulation. However, in this research, Hibiki & Ishii model gave better and stable results that best matched the experimental data and this model is used in this research. The Hibiki & Ishii formulation is expressed in Equation 4.8.

$$
\begin{aligned}
S_{RC} &= -\frac{1}{3\varphi}\left(\frac{\alpha_g}{X_p}\right)^2 f_c n_b \lambda_c = -\left(\frac{\alpha_g}{X_p}\right)^2 \frac{\Gamma_c \alpha_g^2 \epsilon^{1/3}}{d_b^{11/3}(\alpha_{gmax}-\alpha_g)} exp\left[-KC\frac{d_b^{5/6}\rho_f^{1/2}\epsilon^{1/3}}{\sigma^{1/2}}\right] \\
&= -\frac{\Gamma_c}{\psi^{11/3}}\frac{\epsilon^{1/3}}{(\alpha_{gmax}-\alpha_g)}\alpha_g^{1/3}X_p^{5/3}exp\left[-KC\psi^{5/6}\frac{\rho_f^{1/2}\epsilon^{1/3}}{\sigma^{1/2}}\left(\frac{\alpha_g}{X_p}\right)^{5/6}\right]
\end{aligned}
\tag{4.8}
$$

The average bubble diameter is computed from Equation 4.9.

$$d_b = \psi \frac{\alpha_g}{X_p} \tag{4.9}$$

and

$$\lambda_c = exp\left[-K_c \frac{d_b^{5/6} \rho_f^{1/2} \epsilon^{1/3}}{\sigma^{1/2}}\right] \tag{4.10}$$

The turbulence impact is calculated from the Equation 4.11

$$
\begin{aligned}
S_{TI} &= \frac{1}{3\varphi}\left(\frac{\alpha_g}{X_p}\right)^2 f_B n_e \lambda_B \\
&= \left(\frac{\alpha_g}{X_p}\right)^2 \frac{\Gamma_B \alpha_g (1-\alpha_g) \epsilon^{1/3}}{d_b^{11/3}(\alpha_{gmax}-\alpha_g)} exp\left[-K_B \frac{\sigma}{\rho_f d_b^{5/3} \epsilon^{2/3}}\right] \\
&= \frac{\Gamma_B}{\psi^{11/3}} \frac{(1-\alpha_g)\epsilon^{1/3} X_p^{5/3}}{\alpha_g^{2/3}(\alpha_{gmax}-\alpha_g)} exp\left[-\frac{K_B}{\psi^{5/3}}\frac{\sigma}{\rho_f \epsilon^{2/3}}\left(\frac{X_p}{\alpha_g}\right)^{5/3}\right]
\end{aligned}
\tag{4.11}
$$

From these equations, f_c is the frequency of the collisions, λ_c = coalescence efficiency for the collision of bubble and n_b = number of bubbles per mixture volume, f_B = frequency of collision between bubbles and turbulent eddies of the primary phase, λ_B = breakage efficiency from the impact of collision and n_e = the number of turbulent eddies per mixture volume, ψ is the shape factor given as 6, and φ is $1/360\pi$ if the bubbles are spherical. For the coefficients, $\Gamma_c = 0.188$, $K_C = 0.129$, $\Gamma_B = 0.264$ and $K_B = 1.37$

The efficiency of breakage is calculated from the formulation given in Equation 4.12.

$$\lambda_B = exp\left[-K_B \frac{\sigma}{\rho_f d_b^{5/3} \epsilon^{2/3}}\right] \tag{4.12}$$

The alternative Ishii-Kim formulation is described in Equations 4.13 - 4.15.

$$
\begin{aligned}
S_{RC} &= -\frac{1}{3\varphi}\left(\frac{\alpha_g}{X_p}\right)^2 C_{RC}\left[\frac{n_b^2 \mu_t d_b^2}{\alpha_{gmax}^{\frac{1}{3}}\left(\alpha_{gmax}^{\frac{1}{3}}-\alpha_g^{\frac{1}{3}}\right)}\right]\left[1 - exp\left(-C\frac{\alpha_{gmax}^{\frac{1}{3}}\alpha_g^{\frac{1}{3}}}{\alpha_{gmax}^{\frac{1}{3}}-\alpha_g^{\frac{1}{3}}}\right)\right] \\
&= -\frac{1}{3\pi}C_{RC}\mu_t X_p^2\left[\frac{1}{\alpha_{gmax}^{\frac{1}{3}}\left(\alpha_{gmax}^{\frac{1}{3}}-\alpha_g^{\frac{1}{3}}\right)}\right]\left[1 - exp\left(-C\frac{\alpha_{gmax}^{\frac{1}{3}}\alpha_g^{\frac{1}{3}}}{\alpha_{gmax}^{\frac{1}{3}}-\alpha_g^{\frac{1}{3}}}\right)\right]
\end{aligned}
\tag{4.13}
$$

$$
\begin{aligned}
S_{WE} &= -\frac{1}{3\varphi}\left(\frac{\alpha_g}{X_p}\right)^2 n_b^2 d_b^2 \mu_r C_D^{\frac{1}{3}} \\
&= -\frac{1}{3\pi}C_{WE}\mu_t X_p^2 C_D^{\frac{1}{3}}
\end{aligned}
\tag{4.14}
$$

$$
\begin{aligned}
S_{TI} &= -\frac{1}{3\varphi}\left(\frac{\alpha_g}{X_p}\right)^2 C_{TI}\left(\frac{n_b \mu_t}{d_b}\right)\left(1 - \frac{We_{cr}}{We}\right)^{\frac{1}{2}} exp\left(-\frac{We_{cr}}{We}\right) \\
&= \frac{1}{18}C_{TI}\mu_t \frac{X_p^2}{\alpha_g}\left(1 - \frac{We_{cr}}{We}\right)^{\frac{1}{2}} exp\left(-\frac{We_{cr}}{We}\right)
\end{aligned}
\tag{4.15}
$$

where,

v_t is the mean fluctuating velocity of the bubble, v_r is the terminal velocity of the bubble. The terminal velocity and the mean bubble fluctuating velocities and additional variables are defined in Equations 4.16 - 4.20.

$$v_t = \varepsilon^{\frac{1}{3}} d_b^{\frac{1}{2}} \tag{4.16}$$

$$v_r = \left(\frac{d_b g \Delta \rho}{3 C_D \rho_f} \right)^{\frac{1}{2}} \tag{4.17}$$

$$C_D = 24 \frac{(1 + 0.1 Re_D^{0.75})}{Re_D} \tag{4.18}$$

$$Re_d = \frac{\rho_f \mu_f d_b}{\mu_f} (1 - \alpha_g) \tag{4.19}$$

$$We = \frac{\rho_f \mu_t^2 d_b}{\sigma} \tag{4.20}$$

where,

μ_f is the molecular viscosity of the fluid phase, g is the gravitational force, σ is the interfacial surface tension, We is the Weber number and We_{cr} is the cross over Weber number below which the breakage rate is equal to zero and in which case, Equation 4.15 becomes zero and thus, the turbulence is not destroying the bubbles. Ishii and Kim (2001) defined the following coefficients applicable to their model which are implemented in ANSYS Fluent: $C_{RC} = 0.004$, $C_{WE} = 0.002$, $C_{0.085} = 0.085$, $C = 3.0$, $We_{cr} = 6.0$, and $\alpha_{gmax} = 0.75$

4.3.1.2 Sauter Mean Diameter

For multi-phase flow modelling with the Eulerian model, it is necessary to specify the bubble diameter range. The IAC uses the Sauter Mean diameter range in the computation of the bubble diameter range. Hence, the diameter calculation for this research was set to use the Sauter Mean formulation. The Sauter Mean diameter is the average diameter of the bubble/droplet with the same volume to surface area ratio of the ensembles of

the entire bubbles (all discrete particles in the computational domain) which is used to characterise the size. The Sauter Mean diameter is denoted as d_{32} or D_{sm}, and is often larger than the arithmetic mean d_{10}. ANSYS Fluent obtains the most probable size, d_0 from d_{32}. The Sauter Mean diameter finds application in the field of combustion, mass, momentum & energy transfer and efficiency studies. The Sauter Mean diameter D_{sm}, and the range of diameters set in the computational model is used to allow the effect of the IAC values necessary for the interfacial transfer of mass, momentum and heat transfer between the phases. Using the correlation of Wu et al. (1992), and Resin Rammler distribution, the Sauter Mean Diameter is defined in Equation 4.21.

$$d_{32} = 1.330\lambda We^{-0.74} \tag{4.21}$$

The most probable diameter, d_0 is calculated from Equation 4.22

$$d_0 = 1.2726 d_{32} \left(1 - \frac{1}{s}\right)^{\frac{1}{s}} \tag{4.22}$$

where,

$s = 3.5$, λ is $\frac{d}{8}$, σ is the surface tension of droplet and λ is the radial internal length scale at the entrance. In the Eulerian multi-fluid VOF model, the interfacial area transport equation can be solved by:

- Allowing for the distribution of the secondary phase diameter through the Sauter Mean range.

- Specifying the diameter and compute the interfacial area through algebraic formulation

The simulation set-up also requires the dissipation function. This function calculates the dissipation rate in the model for the coalescence and breakage formulation. The Wu-Ishii-Kim model was used in this research because it takes into consideration the hydraulic diameter of the system. The formulation for the dissipation rate is defined in Equation 4.23.

$$\varepsilon = f_{TW} \left(\frac{1}{2D_h}\right) V_m^3 \tag{4.23}$$

where,

$$f_{TW} = \frac{0.316}{[(1 - \alpha) R_{em}]^{0.25}} \tag{4.24}$$

and,

$$R_{em} = \frac{\rho_m V_m D_h}{\mu_m} \tag{4.25}$$

where, ρ_m is the mixture density, V_m is the mixture velocity, R_{em} is the mixture Reynolds number and D_h is the hydraulic diameter which is $0.189m$ in this research. The range of the interfacial area concentration is set for the gas phase diameter. This is $0.1 \leq d_g \leq 40mm$ for the gas phase.

4.3.1.3 Surface Tension Effect

Surface tension is the radially attractive (cohesion) forces between the molecules of a fluid which tends to minimise the surface area but also counterbalanced by the radially outward pressure gradient (adhesive) force across the surface. Surface tension is important in determining the interfacial/geometrical configuration of the gas-liquid dynamics that result to the prevailing flow pattern. Surface tension is dependent on two dimensionless quantities, Weber number and Capillary number. In this research, the Weber number was considered because the Reynolds number $R_e >> 1$.

$$We = \frac{\rho L v^2}{\sigma} \tag{4.26}$$

Using the fluid data from this research for a typical churn turbulent flow at $j_g = 0.21m/s$ and $j_l = 0.05m/s$:

$$We = \frac{23.4 \times 5.67 \times 1.3359^2}{0.0185} = 12798$$

This shows that the inertia force is dominant force in the fluid flow scheme. In this research, the surface tensions value of 0.0185n/m for the liquid (naphtha) phase was used.

4.3.2 The Granular Secondary Phase Set Up

For three-phase gas-liquid-solid set up (option c of Figure 4.1), the secondary solid phase property set-up is relevant to successful computation of the interfacial forces. Full details of the granular solid phase property set up have been discussed in chapter 3. The granular secondary phase used in this project is sand (silicon dioxide) whose phase properties are shown on Table 4.1. ANSYS Fluent uses the phase property for the granular temperature

(the kinetic energy of the random motion of the solids) computation, hence it is important that the granular phase properties are correctly set up for accurate computation. ANSYS Fluent Algebraic formulation is used to compute the granular temperature in this research. From the solid phase momentum flux Equation 3.10, in addition to the interfacial forces, the solid pressure, ∇P_s and the frictional pressure, ∇P_{fr} are important input to the momentum flux computation which should be determined.

The kinetic theory of granular flow (KTGF) is important in less dense flow when the particles can instantaneously collide with each other. This collision creates frictional stress, τ_{fric} which is defined in Equation 4.27 in Newtonian form.

$$\tau_{fric} = P_{fric}\vec{I} + \mu_{fric}\left(\nabla\vec{\mu}_s + (\vec{\mu}_s)^T\right) \tag{4.27}$$

In this research, the solid pressure is computed with the Lun et al. (1984) model. This is the pressure gradient, ∇P_s in the granular phase momentum flux Equation 3.10 and expressed in Equation 3.35. This formulation account for the kinetic and collisional contribution in the overall solid pressure. The solid pressure and the solid viscosity are calculated from Equations 4.28 and 4.29. The kinetic viscosity (kinetic part of the solid/granular viscosity) is calculated with Syamlal et al. (1993b) formulation given in Equation 3.43.

$$P_s = P_{kin} + P_{fric} \tag{4.28}$$

$$\mu_s = \mu_{kin} + \mu_{fric} \tag{4.29}$$

The frictional viscosity, which is calculated with Schaeffer (1987) formulation is normally neglected in less dense flows as in this research. In addition, the frictional pressure term in Equation 4.28 which is also included in the momentum Equation 3.10 is a function of solid concentration and is therefore neglected in this research. The Granular bulk viscosity which is the resistance of the solid particle to compression and expansion is also neglected in this research. The radial distribution is applicable in dense flow and therefore, it is neglected in the set up. Technically, the momentum flux of the solid defined in Equation 3.10 is thus reduced to Equation 4.30.

$$\frac{\partial}{\partial t}(\alpha_s\rho_s\vec{v}_s) + \nabla.(\alpha_s\rho_s\vec{v}_s\vec{v}_s) = -\nabla p_s + \nabla.\bar{\bar{\tau}}_s + \alpha_s\rho_s\vec{g} + M_{i,s} \tag{4.30}$$

4.3.3 Turbulence Model Selection

Turbulence model selection in CFD computation determines the solution convergence and outcome of turbulent flows in a flow systems. Basically, the turbulence models are used to close the RANS equations. Typically, most turbulence models used in multi-phase flow are k-epsilon (k-ε) (2 eqn), k-omega (k-ω) (2 eqn) and Reynolds stress (7 eqn) models. Each of these models has options which can be selected on best fit choice. The k-ω has the Standard, Baseline (BSL) and Shear-Stress Transport (SST) options while the k-ε has the Standard, Renormalisation group (RNG) and Realizable options. The Reynolds stress model features the pressure strain and the quadratic pressure strain options. Details of these models are given in chapter 3. A good CFD practice requires validation of the results against experimental data. In this research, turbulence model sensitivity was carried out on the 3 turbulence models to determine which model best match the experimental results by visual of the contour plots and appropriate validation of the gas volume fractions with the experimental results. The test case for churn turbulent flow was used to validate the turbulence model used in this research.

4.3.3.1 Qualitative Validation of Turbulence Model

The comparison of the gas fractions for the 3 options of the k-ω model is shown on qualitative plot of Figure 4.4 for computational time of up to 180 seconds to determine the most stable model for this research. The results shows that the longer the simulation runs, the BSL k-ω and SST k-ω become unstable as could be seen on the contour plot as the contours becomes unrepresentative of the churn flow pattern. The k-ω standard is stable at all time during the simulation runs. The stability criterion means that the churn flow geometric configuration did not change irrespective of the simulation time from 30s to 180s and even beyond. Once stabilised flow has been reached, all variables remain constant all through the duration of the simulation.

Secondly, simulation for the k-ε models was carried out. These include the Standard k-ε, RNG k-ε and the Realizable k-ε with standard wall treatment. The qualitative plot of the results is shown in Figure 4.5. From the contour plots, it can be seen that the k-ε standard produced similar results to the k-ω standard. However, it can be seen from the
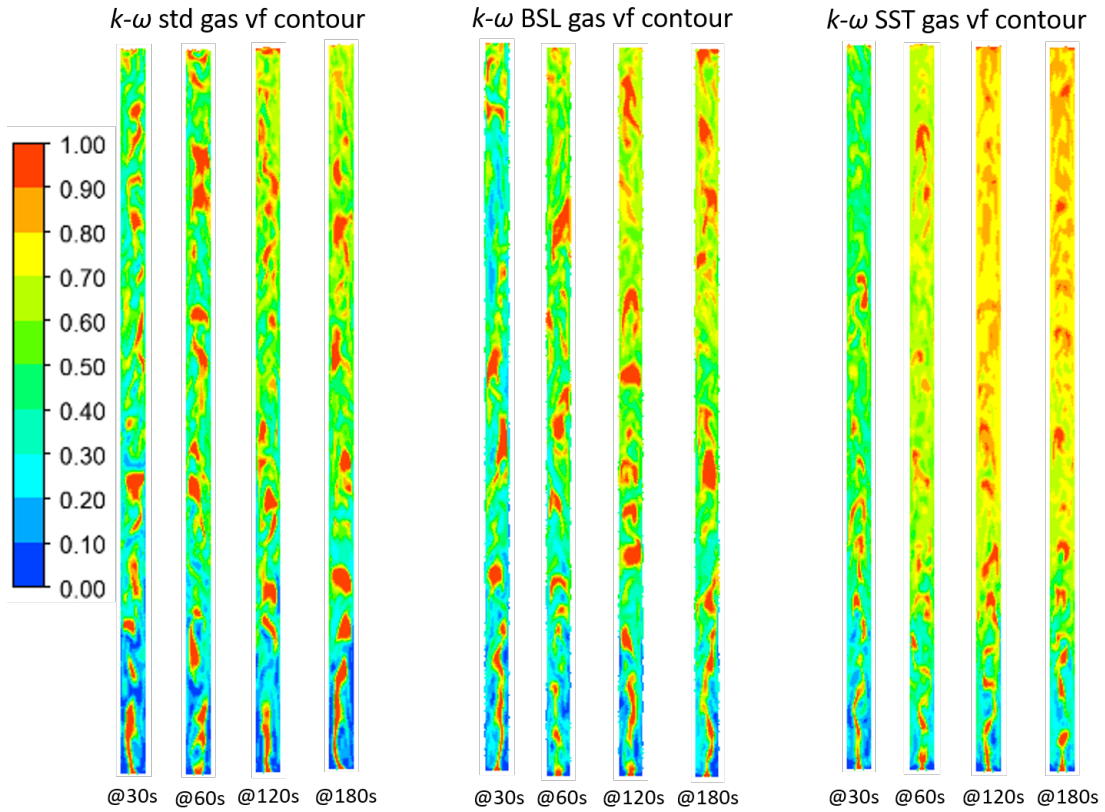
Figure 4.4: Churn Flow Gas Volume Fraction Comparison for k-ω Model

plot that the k-ω standard was more stable at longer computational time. Although, the result of the Reynolds stress model is not shown in this thesis, but the outcome was not representative and further analysis was not carried out on the model.

Therefore, it can be concluded from the foregoing presentation and analysis from the qualitative plots of all model options that the Standard k-ω shows better stability for as long as the simulation runs and maintained a stable churn configuration all through the duration of the computation.

4.3.3.2 Quantitative Validation of Turbulence Model

CFD validation process requires both qualitative and quantitative analysis of the flow dynamics, hence, quantitative information is required to further validate the CFD turbulence model used in this research. Statistical analyses of the time averaged gas volume fractions were compared with those obtained by Omebere-Iyari et al. (2007b) in their experimental work. The area averaged gas volume fractions of a churn flow (gas superficial velocity of 0.21 m/s and liquid superficial velocity of 0.05 m/s) obtained from
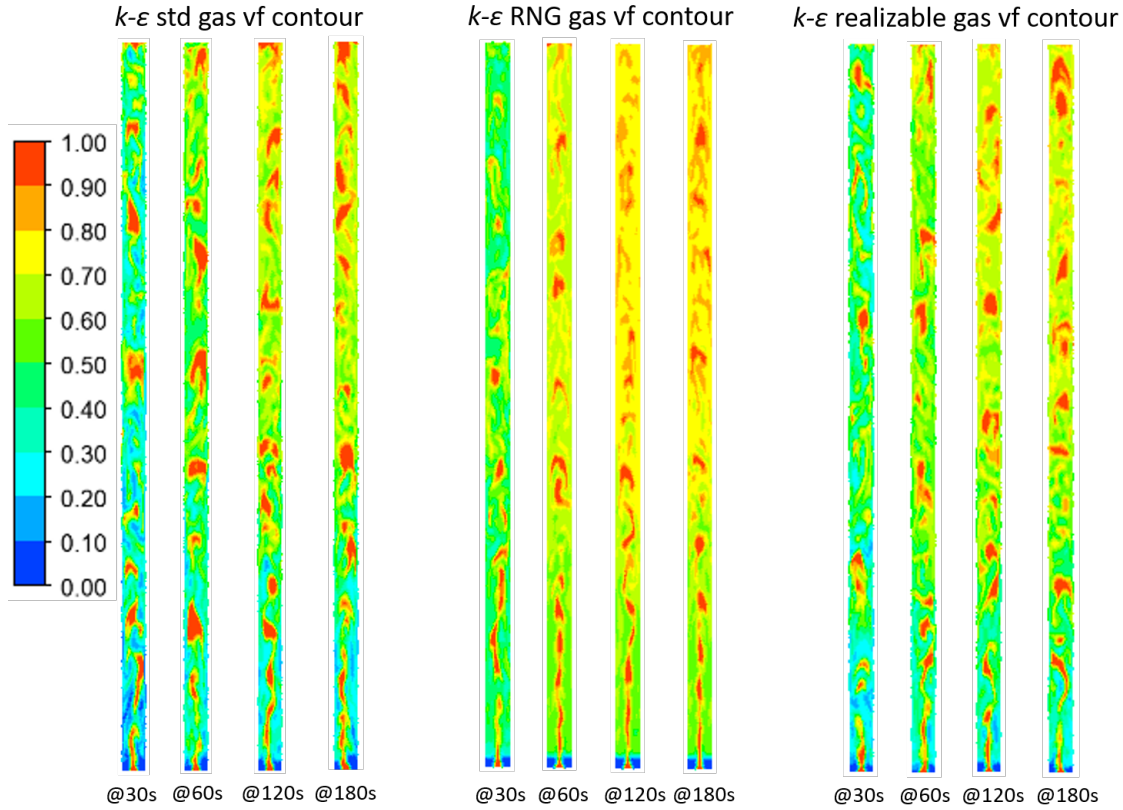
Figure 4.5: Churn Flow Gas Volume Fraction Comparison for k-ε Model Options

the CFD results were compared with the experimental gas volume fraction traces. The graphical plots are shown in Figure 4.6 and Figure 4.7. Analysis of the plots indicate that the volume fractions are in the average of: experiment = 0.63; k-ω standard = 0.62; k-ω BLS = 0.70; k-ω SST = 0.79; k-ε Standard =0.70; k-ε RNG =0.79 and the k-ε Realizables = 0.74. From the comparison of the values, the k-ω standard best fit the experimental data set of Omebere-Iyari et al. (2007b) with an averaged gas volume fraction of 0.62 . Further detailed gas volume fraction comparison of the performance of k-ω standard is shown in Figure 5.4 for the validation of other flow regimes encountered in the experimental work.

Following the qualitative and statistical validation of the gas volume fractions, the k-ω standard turbulence model is the chosen formulation used to compute the turbulence effect in this research.
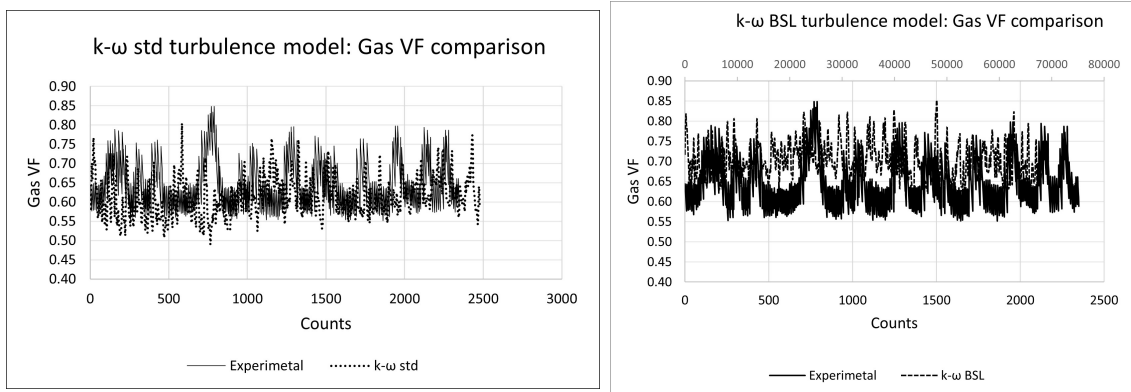
(a) K-Omega Std

(b) K-Omega BSL
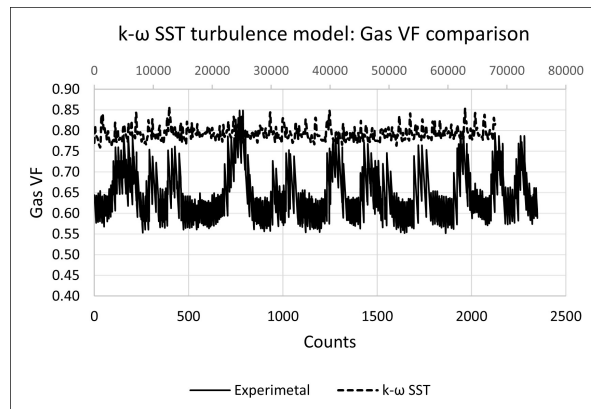
(c) K-Omega SST

Figure 4.6: Gas Volume Fraction Comparison for K-Omega Turbulence Models
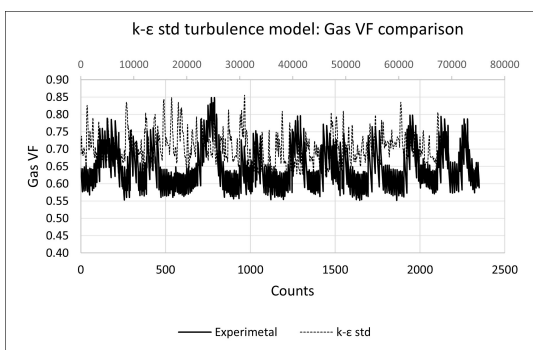
(a) K-Epsilon STD
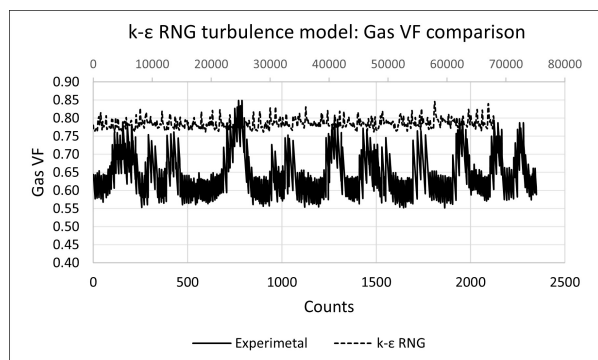
(b) K-Epsilon RNG
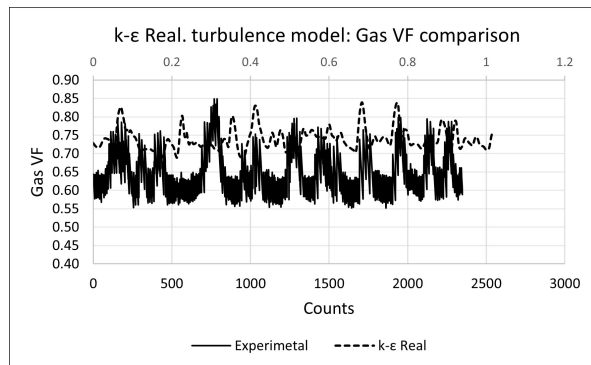
(c) K-Epsilon Realisable

Figure 4.7: Gas Volume Fraction Comparison for K-Epsilon Turbulence Models

TWO-PHASE FLOW RESULTS & ANALYSIS

This chapter deals with two-phase flow results and discussions while chapter 6 covers the three-phase flow results and discussions. Two-phase flow model operates a heterogeneous regime where the bubble diameter sizes are determined by coalescence and breakup phenomena at constant physical properties and operating conditions. The variation of the bubble sizes depend on the fluids superficial velocities.

Experimental results of Omebere-Iyari et al. (2007b) is used as initial benchmark to validate the appropriateness of the chosen computational model. Their experimental research work covers the gas superficial velocities of 0.09m/s $\leq j_g \leq$ 14.8m/s and liquid superficial velocities of 0.004m/s $\leq j_l \leq$ 4m/s at a pressure of 20 bar and a temperature of 30 deg C. These superficial velocities cover the full spectrum of flow regimes from bubbly to annular flows in large diameter vertical pipe. The fluid types used by the authors are nitrogen gas and liquid naphtha which have similar physical properties to natural gas and oil in the petroleum field. The validated and chosen model shown in chapter 4 is used to investigate two-phase gas-liquid flow in large diameter pipe presented in this chapter. The results presented here covers the flow regime spectrum of a large diameter vertical pipe with petroleum fluid properties. The test fluid properties, solution domain and boundary conditions are shown in Table 4.1 and Figure 4.2 respectively.

Pioneer researchers who investigated the hydrodynamics of multi-phase flow in large diameter vertical pipe, (irrespective of the fluid properties) had claimed that slug flow was not observed at any gas superficial velocities, rather, churn flow was dominant at the superficial velocities where slug flow used to be observed (Smith et al., 2012; Schlegel et al., 2009; Omebere-Iyari et al., 2007b; Sun et al., 2003; Ohnuki and Akimoto, 2000). Nonetheless, the experimental data set available for large diameter pipe are still

very sparse compared to small diameter pipe. Therefore, detailed understanding of the hydrodynamics and the mechanism of multi-phase flow in large scale pipe are required to fill the gap in the understanding of multi-phase flow for cases where large scale pipe is required.

5.1 Test Case

The test case data set used for validation of this research work were obtained from the experimental work of Omebere-Iyari et al. (2007b). These data setsS were chosen because they used natural petroleum fluid properties which are different from air and water commonly used in most experiments. The rationale is to use fluid with the same properties as natural gas and oil that are found in a typical conventional oil well. In order to measure the gas volume fractions, the authors used two types of densitometers in their experimental work, the fast volume weight meter (FVWM) densitometer and the single beam gamma densitomer (SBGD). These densitometers contain Cs 137 radioactive source and an ionisation detector. The gas fractions signals were detected from the attenuation of the radiation intensity. In this research, two-phase flow CFD simulation was performed

Table 5.1: Four Flow Pattern Test Case

Flow Conditions and Flow Patterns Identified				
Cases	j_g (m/s)	U_{ge} (m/s)	Exp. flow patterns	CFD flow patterns
case I	0.1	0.64	Bubbly	Bubbly
case II	0.21	1.34	Intermittent (Churn)	Intermittent (Churn)
case III	1	6.36	Semi Annular	Semi Annular
case IV	4	25.45	Annular	Annular
@ $j_l = 0.05$m/s and liquid entrance velocity, u_{le}. =0.0593m/s				

with the experimental data set to investigate the four most prominent flow patterns in two-phase flow in vertical pipe. Four experimental outcomes were obtained at constant liquid superficial velocity of 0.05m/s, with variable gas superficial velocities of 0.1, 0.21, 1.0 and 4m/s selected at subsequent runs. The inlet configuration of the pipe geometry

was split into two separate gas and liquid inlets, in a manner similar to the experimental setup, in order to achieve the initial fluid entrance velocity conditions. The separate gas inlet methodology is meant to provide the single orifice type spargering effect for the inlet gas. However, Omebere-Iyari et al. (2007b) has proven in their experiment that the inlet gas configuration has no effect on the flow pattern achieved in the downstream of the mixing point. Equations 5.1 and 5.2 were used to calculate the gas and liquid entrance velocities from the respective superficial velocities. Details of the parameters as well as the simulation outcomes are shown in Table 5.1.

$$U_{ge} = \frac{A j_g}{A_1} \tag{5.1}$$

$$U_{le} = \frac{A j_l}{A_2} \tag{5.2}$$

where,

U_{ge} is the local gas entrance velocity at the inlet A_1, U_{le} is the local liquid entrance velocity at the inlet A_2 and A is the outlet total cross-sectional area which is pressure controlled. j_g and j_l are the gas and liquid superficial velocities respectively. The schematic of the cross-sectional inlet and outlet boundary conditions is shown in Figure 5.1.
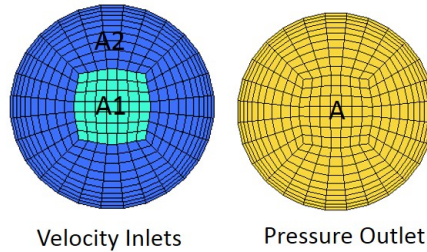
Figure 5.1: Inlet and Outlet Cross-Sectional View

5.2 Flow Pattern Analysis

The definition attributed to the geometrical configuration of the fluid arrangement and structures in a two-phase gas-liquid flow is based on the qualitative and quantitative analysis of the gas volume fractions and other variables. These two approaches are used in this research to delineate the flow patterns and attributes. In addition to the development of correlations for the prediction of gas fractions, the ability to accurately identify the flow

regimes and characterise the physical mechanism governing each flow regime is necessary for the development of accurate two phase flow models (Schlegel et al., 2009).

Although, few qualitative and quantitative data are analysed and shown in this thesis, the simulations were ran for large number of cases such that covers various flow patterns in a vertical pipe. Due to page limitation, not all the results are presented but, details of the velocity data used are shown in Table 4.2. Where necessary, videos have been attached to this write up to view some of the flow development of the depicted qualitative data and figures. As the database of two-phase gas-liquid flow in large diameter vertical pipe is few, this research would be considered as an additional proof of findings that are already published on literatures on large diameter pipe flows and new outcomes from this research.

5.2.1 Qualitative Analysis and Classification of Flow Pattern

One of the earliest methods used for flow pattern identification is the visual observation of the flow configurations. Although, most past investigators used this method, there were issues with the accuracy of their outcomes due to human errors and personal interpretation of the results as well as limitation of the instrumentation device employed. The CFD method provides a better internal symmetrical view of the flow pattern evolution. One of the objectives of this research is to investigate the flow regime development in large diameter pipe (made possible in CFD) and compares the results with the experimental results and findings in published literatures. Although the classification of the geometrical configuration in multi-phase flow can be subjective, attempt has been made to use the most appropriate analysis and comparison with published literatures to reach a conclusion.

Four distinct flow patterns were observed during the simulation which were compared with the results of Omebere-Iyari et al. (2007b). The summary of the results is shown in Table 5.1. The four flow patterns observed are churn bubbly, churn turbulent (intermittent churn), semi-annular and annular flow. Traditional slug flow which is often present in many small diameter pipe experiments was not observed in this research. This is in line with the results obtained by Smith et al. (2012), Omebere-Iyari et al. (2007b) and Ohnuki and Akimoto (2000) from their experiments in large diameter pipes. The following

sections describes the qualitative analysis of the two-phase flow hydrodynamics.

5.2.1.1 Bubbly Flow

Figure 5.2a shows the instantaneous symmetrical and cross-sectional qualitative static plots of churn bubbly flow obtained in this research at 138s, 165s and 282s. The bubbles are characterised by deformable, elongated and irregularly shaped bubble particles travelling in a zigzag motion which looks like coalesced and dispersed churn-like bubbles in the flow field. While the liquid stream moves in a forward and reverse manner. The bubbles shown in Figure 5.2a is a type of group-2 bubble which can be determined based on the drag behaviour of the bubbles according to Schlegel et al. (2010). This type of bubbles are different from group-1, the type of bubbly flow known as dispersed bubbles which are traditionally found in bubble columns at low superficial velocities in small diameter vertical pipe. The behaviour of group-2 bubbles is closely linked with the surface instability in large diameter pipe which differentiate its flow field from those of small diameter pipe. There are different mechanisms responsible for bubble coalescence and breakup that result in group-2 bubbles. These mechanisms are: Random collision, Wake entrainment, Turbulent impact, Shearing off and Surface instability.

In this research, it is observed that small round bubbles and cap bubbles are not obtained in the bubbly region and subsequent regions. It is also observed that as the fluid velocity was increased from low to high velocities, smaller bubbles agglomerate to form large bubbles while some of the smaller bubbles are engrained within the liquid film which becomes unnoticeable. These mixtures of large and small bubbles translate to higher gas volume fractions in the flow scheme than would normally be observed in the case of well dispersed bubble flow pattern. This increase in gas volume fractions is shown in section 5.3.

5.2.1.2 Turbulent Churn Flow

Churn flow is the most difficult flow pattern to understand. In the early stages of multi-phase flow studies, most researchers believed that churn flow was just a transition flow pattern or an entrance phenomenon. In this research, churn flow is seen to transit
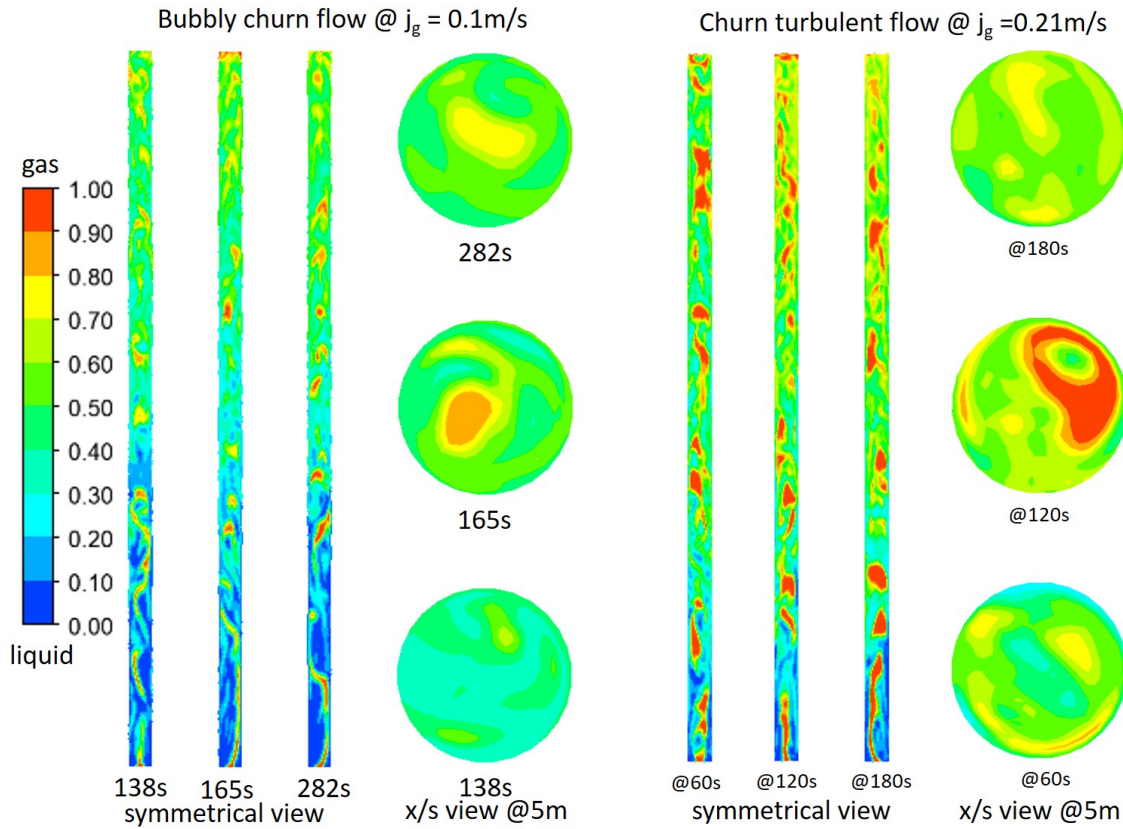
(a) Qualitative plot of bubbly churn flow   (b) Qualitative plot of churn turbulent flow

Figure 5.2: Instantaneous Qualitative Plots for Churn Bubbly and Churn Turbulent Flow

over a wide range of superficial velocities and is a well established flow pattern of interest in large diameter pipe. The churn turbulent flow is characterised by continuous liquid slugs with dispersed churning bubbles in the liquid film. The traditional well defined flow pattern called slug flow was not observed between the bubbly and stabilised churn (froth) flow. This finding is similar to that obtained by Omebere-Iyari et al. (2007b) and Ohnuki and Akimoto (2000).

The instantaneous symmetrical and cross-sectional qualitative plots of churn flow pattern observed in this research is shown in Figure 5.2b for 60s,120s and 180s. The structure of the geometrical configurations shown in the contour plots bear the signature of churn flow in large diameter pipe which are similar to the observations of Omebere-Iyari et al. (2007b) and Schlegel et al. (2010). It is observed in this investigation that churn flow is characterised by churning (swirling) motion with deformed bubble structures in which vertical flow motion of the liquid film are oscillatory and produces irregular shaped

portions of gas bubbles that are larger than local group-2 bubbles. Unlike the slug flow, these bubbles have narrower shaped gas plugs where continuity seems to be destroyed by the gas phase turbulence (McQuillan and Whalley, 1985) and flow reversal with falling liquid; a condition referred to as flooding (Hewitt and Jayanti, 1993). Results from this research has shown that, for moving fluids, changes in the velocities and flow conditions alters the geometrical configurations developed in the flow scheme due to instability and continuous breakup and coalescence of the bubbles.

5.2.1.3 Semi-Annular Flow

Semi-Annular flow is an interregnum regime that occurs between churn flow and full annular flow (Spedding et al., 1998). Figure 5.3a shows the symmetrical and cross-sectional qualitative plots of the semi-annular flow obtained in this investigation. This flow pattern is observed as the gas superficial velocity increases, and the gas-phase tends to flow in the centre of the pipe with entrained liquid slugs in the gas core. Semi annular flow is different from annular flow where there is distinct center gas core all through the pipe centre. The Semi-annular flow pattern is a rare flow regime and its characterisation can be subjective depending on the traces observed, hence most researchers did not categorise it differently. Only few researcher have recognised and reported the existence of semi-annular.

5.2.1.4 Annular Flow

Annular flow regime occurs when there is a high gas to liquid superficial velocity ratio. This flow pattern is characterised by a centre core of gas carrying little entrained liquid droplets or in most cases, no liquid droplet in the gas core at the center of the pipe. The gas superficial velocity plays a crucial role in annular flow development. When the gas rate is insufficient, the liquid droplets fall back, accumulate, and form a bridge and semi annular/churn flow takes place. Figure 5.3b shows the symmetrical and cross-sectional qualitative plots of the annular flow obtained from this CFD investigation. The cross-sectional plots were obtained at different times and at the same height to show the contour plots are different locations. The very thin liquid film is shown in the

(a) Qualitative semi annular flow plot   (b) Qualitative annular flow plot
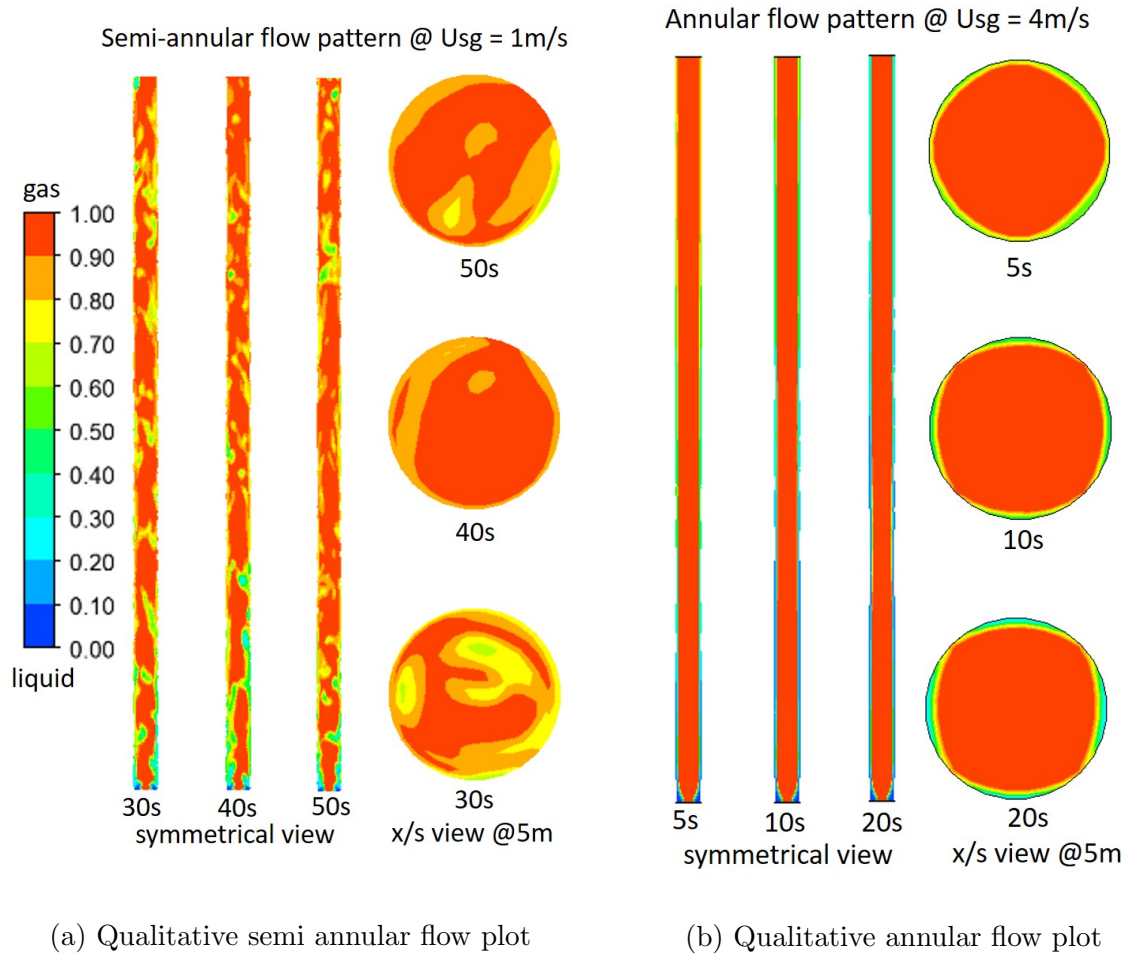
Figure 5.3: Instantaneous Qualitative Plot for Semi Annular and Annular Flow Patterns

symmetrical view of the pipe vertical section of Figure 5.3b.

5.3 Quantitative Analysis of the CFD Results

Statistical analysis and characterisation of time series gas volume fractions and pressure gradients obtained from experimental and CFD results have been an effective tool for flow pattern identification and parameter determination to investigate flow pattern in two-phase flows. The initial step of this research was the investigation of four cases as indicated on Table 5.1 and compare with the benchmarked experimental results. The key parameter needed for flow pattern analysis is the gas fraction or gas concentrations at the cross section of the pipe. The gas volume fractions is the most fundamental and crucial parameter as it is required as an input in almost every two-phase flow calculations such as two-phase mixture density, two-phase mixture viscosity and actual velocities of

each phase (Bhagwat and Ghajar, 2014). Hence, the gas volume fractions in conjunction with pressures and in-situ velocities were obtained at various height of the pipe and were analysed in a manner similar to Jones Jr and Zuber (1975*b*), Costigan and Whalley (1997), Song et al. (1995) and Lowe and Rezkallah (1999) using various statistical analysis methods. Classical drift flux technique is also used to analyse the gas fractions and velocities.

Statistical analysis of time dependent averaged gas concentrations commonly called void fractions or gas holdup were performed accordingly. The gas concentration data in this investigation were monitored and extracted at axial location of 26.5 diameter, and compared with the expected trends from the benchmarked experimental results. The gas fractions data were extracted at 1ms (fixed time step size of 0.001s) which is equivalent to a frequency of 1000Hz at fully developed flow. The gas volume fraction is the average over the cross section which shows the passage of gas bubble particles within the flow. This computed area-weighted average of the gas volume fraction is obtained from the mathematical formulation of Equation 5.3.

$$\frac{1}{A} \int \alpha A = \frac{1}{A} \sum_{i=1}^{n} \alpha_i A_i \tag{5.3}$$

where, A = cross-sectional area open for flow, α_i = fraction of phase i and A_i is the interfacial area. The summation is applied to the cross sectional surface area available for the fluid flow. The gas volume fractions obtained were compared with the experimental data of Omebere-Iyari et al. (2007*b*). Figure 5.4 shows the graphical plot of the local gas volume fractions for the four cases (bubbly, churn, semi-annular & annular flow) validated against the experimental data set. Detailed statistical analysis of the results obtained in this investigation are presented in the following sections.

5.3.1 Gas Volume Fraction Traces

multi-phase flow hydrodynamic parameters are mostly computed from the gas volume fractions. In this research, the extracted gas volume fractions were used to characterise the flow configurations into its respective flow patterns which in turn is used to develop the flow regime map in large diameter pipe. Hence, the flow pattern comparison was

(a) Bubbly Flow

(b) Churn Turbulent Flow

(c) Semi Annular Flow

(d) Annular Flow
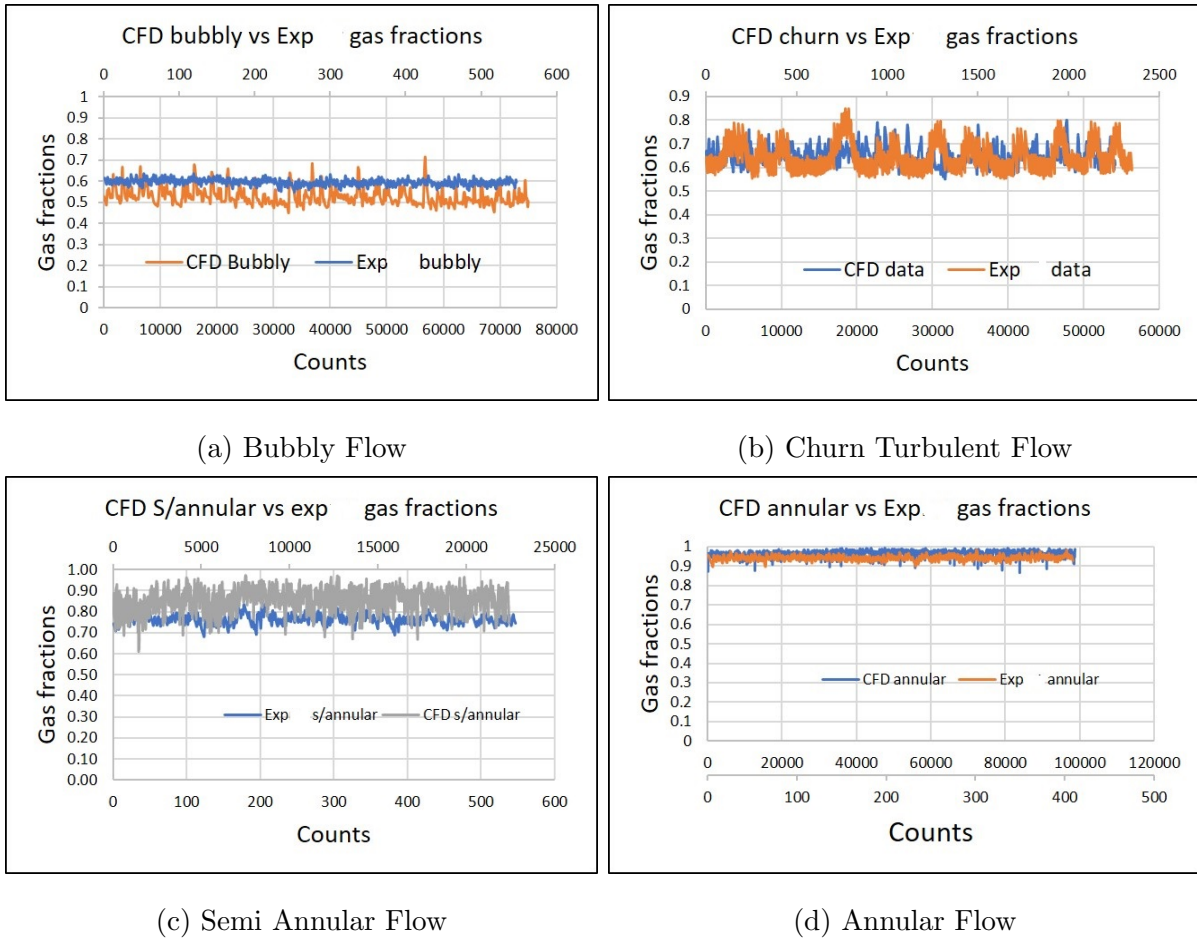
Figure 5.4: CFD vs Omebere-Iyari et al. (2007b) Gas Volume Fraction Comparison

performed using the gas fraction analysis of the results from the CFD computation. The root mean square error (RMSE) of the CFD results in comparison to the experimental results is computed from the formulation given in Equation 5.4. The results of the RMSE

Table 5.2: RMSE Values of CFD Results

Regime	Bubbly flow	Churn flow	Semi annular flow	Annular flow
RMSE	3%	7%	8%	2%

for each of the flow patterns are shown in Table 5.2. It can be seen that the RMSE for all the flow patterns compared are well below acceptable threshold of 10%. This confirmed the accuracy of the research solution technique earlier presented in chapter 4 that is used in this research.

$$RMSE = \left(\sum_{i=1}^{n} \left(\Delta \alpha_i \right)^2 / n \right)^{\frac{1}{2}} \tag{5.4}$$

where, n = sample counts, $\Delta\alpha_i$ = difference in gas fractions. The gas fractions analysis of the four flow patterns obtained in this investigation is presented below.

5.3.1.1 Bubbly Flow Gas Fractions

Bubbly flow characterisation has a wide range of flow structures from small spherical to disturbed or agitated (clustered) and deformed bubbles which unquestionably cannot be described as slug or full churn flow. In this research and in the benchmarked experimental results, gas-liquid superficial velocity of 0.1m/s and 0.05m/s respectively produces bubbly churn flow. The time series cross-sectional gas volume fraction from the CFD computation were monitored and extracted from the pipe cross-section at height of $Y/D = 26.5$. The trends from the CFD and experimental traces were appropriately compared as shown in Figure 5.4a. This means that the gas fractions extracted at $Y/D = 26.5$ in this CFD simulation was fully developed at length shorter than that at which the experimental investigators obtained developed results.

(a) Bubbly Flow Gas Fractions   (b) Bubbly Flow in-situ Velocity
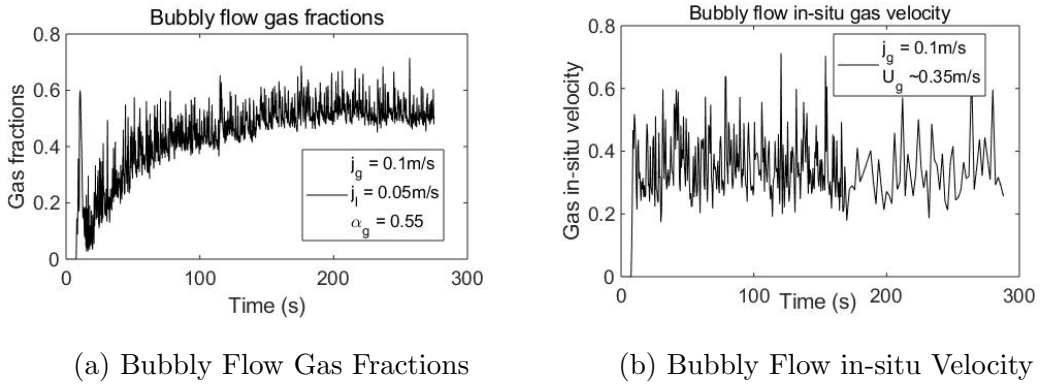
Figure 5.5: Bubbly Flow Time Averaged Gas Fractions and In-Situ Velocity

Figure 5.5 shows the bubbly gas volume fractions and the in-situ velocity obtained from this investigation. It can be seen that at fully developed flow, the gas in-situ velocity, U_g is greater than the superficial velocity, j_g. This is expected for a two phase flow simulation or experiment. Earlier on, Harmathy (1960) postulated that the rise velocity of fairly large bubbles (bubbly flow) which is insensitive to bubble size can be described by the formulation given in Equation 5.5

$$U_\infty = 1.53 \left[\frac{g\left(\rho_l - \rho_g\right)\sigma}{\rho_l^2} \right]^{1/4} \tag{5.5}$$

where, U_∞ is the rise velocity of the bubbles. The rise velocity is also called the local drift velocity which can be described by Equation 5.6

$$U_{gj} = U_g - j \tag{5.6}$$

where, U_{gj} = local drift velocity which is equivalent to the rise velocity, U_∞. Inserting values of the results and the fluid properties into Equations 5.5 and 5.6 and solving, we have the following results shown in Table 5.3. From the table, it can be seen that the rise velocity, U_∞ is equivalent to the local drift velocity, U_{gj}. Thus, in bubbly flow, the rise velocity is equivalent to the local drift velocity.

Table 5.3: Bubbly Flow in-situ Field Variables

Variables	U_g(m/s)	j(m/s)	U_∞(m/s)	U_{gj}(m/s)	α_g
Results	0.35	0.15	0.2	0.2	0.5-0.6

5.3.1.2 Churn Turbulent Flow Gas Fractions

As the gas superficial velocity was increased from 0.1 to 0.21m/s ($\approx$ 100% increase), the number density of the bubbles increases. This makes the bubbles to closely packed together leading to coalescence of the bubbles. The bubble size agglomerates into churn like but yet chaotic gas morphology which are not spherical but highly deformed. This regime is characterised by high turbulence and swirling motion leading to continuous coalescence and breakage of the deformed bubbles and transfer of momentum. This process called churning hence, the name churn turbulent flow because of its heterogeneous nature. The deformity depends on the Eotvos number, the ratio of the gravitational force to the surface or interfacial tension force. Omebere-Iyari et al. (2007*b*) called it intermittent flow pattern. In this study, the churn turbulent was observed with the gas fractions ranging from 0.5 to 0.8. The continuous coalescence and breakage of the gas bubbles creates large bubbles (than the bubbly churn) and smaller deformed bubbles in the continuous liquid stream. This leads to increase in the gas fractions traces. Figure 5.6a shows the time averaged gas fractions and the in-situ gas velocity. Table 5.4 shows the in-situ results for churn flow field variables.

Table 5.4: Churn Flow in-situ Field Variables

Variables	j_g(m/s)	j(m/s)	U_g(m/s)	U_{gj}(m/s)	α_g
Results	0.21	0.26	0.48	0.22	0.50-0.80
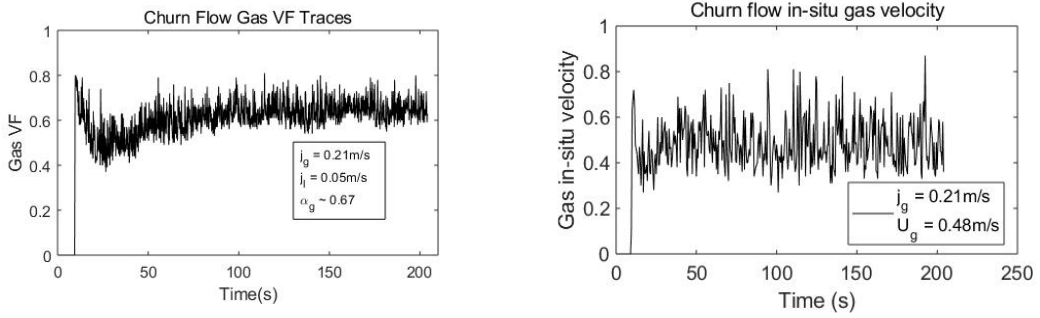
(a) Churn flow gas fractions

(b) Churn flow in-situ gas velocity

Figure 5.6: Churn Flow Time Averaged Gas Fractions and in-situ Velocity

The line plot shown in Figure 5.7 shows the distribution of the gas fractions across the pipe width. The plot shows the dynamic nature of the flow characteristics, as a result of continuous coalescence and breakage of the gas bubbles throughout the duration of the simulation. The bubbles were not able to coalesce into larger Taylor bubbles found in slug flow. The continuous coalescence and destruction of the bubbles in the churn threshold shows the intermittent nature of the churn flow.
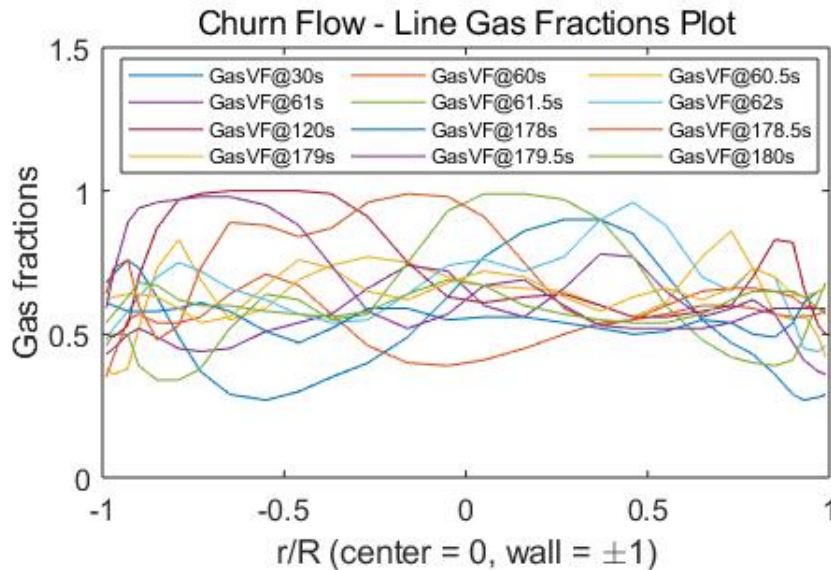
Figure 5.7: Churn Flow Instantaneous Gas Fraction Line Plot

From the plot, r = radial position from the center and R = radius of the pipe. Figure 5.4b shows the validation of the churn flow with the experimental data at gas and liquid superficial velocities of 0.21 and 0.05m/s respectively. The cross-sectional gas volume fraction for bubbly/churn transition observed in this research was 0.5 - 0.6 which matched the experimental results of Omebere-Iyari et al. (2007b).

5.3.1.3 Semi-Annular Flow Gas Fractions

The graphical plot of the semi-annular flow gas volume fractions and in-situ average gas velocity are shown in Figure 5.8. This flow pattern was observed at the gas fractions range of 0.75 to 0.9. The volume fraction comparison of this result with that obtained by Omebere-Iyari et al. (2007b) is shown on the graphical plot of Figure 5.4c. The RMSE percentage for the semi-annular flow is 8%, within acceptable limit of error in the CFD computation. This comparison validates the CFD model being able to simulate this rare flow pattern without prior knowledge of the gas volume fractions.

(a) Semi annular flow gas fractions

(b) Semi-annular flow in-situ velocity
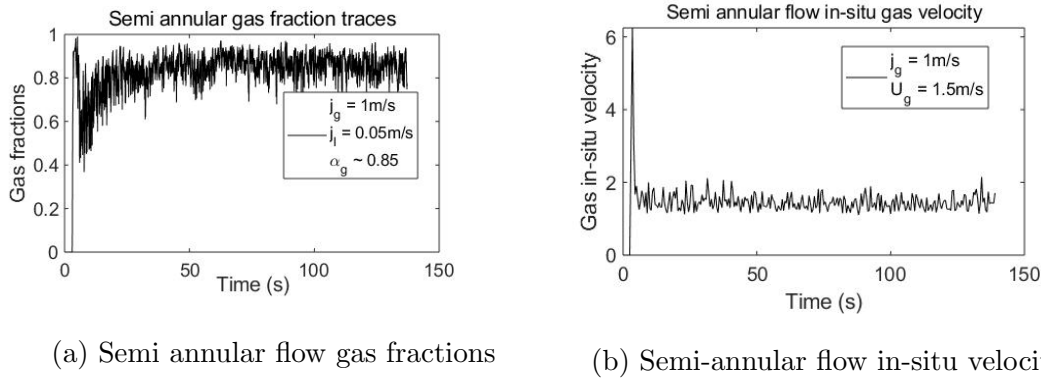
Figure 5.8: Semi Annular Flow Time Averaged Gas Fractions and In-Situ Velocity

Semi-annular flow is a bridge flow pattern that is rarely mentioned in literature while some researchers called it churn flow. Spedding et al. (1998) presented details of semi annular flow to be present between churn and annular flow in vertical pipe. There is a close relationship between churn turbulent and semi annular flow in that they have the same gas structures and swirling bubble motion that carries reduced liquid slug that resembles extreme chaotic churn flow. It can be seen from Figure 5.8b that the in-situ gas velocity is one-half of the gas superficial velocity. Comparing with the churn flow, the in-situ gas velocity ration is lower in semi-annular flow than in churn flow.

5.3.1.4 Annular Flow Gas Fractions

Further on, the gas superficial velocity was increased in line with the experimental data. This increase led to the development of the annular flow pattern. This flow pattern is characterised by a high speed gas core containing entrained liquid droplet and features a thin film of liquid around the pipe wall. Figure 5.9 shows the gas fraction and the in-situ velocity obtained at the cross-section at 26.5 diameter. The results show that the gas fraction is 0.95 and the gas in-situ velocity is approximately equal to the gas superficial velocity. The annular liquid film is so thin that it could be hardly noticeable such that the gas fraction is 0.95 and the gas local velocity approaches the gas superficial velocity as initially claimed by Taitel et al. (1980). This is shown in Figure 5.9b which indicates that the two velocities are approximately equal to the gas superficial velocity which are 4.06m/s and 4m/s respectively. The Annular flow pattern is mostly observed in gas condensate wells and wet gas wells. Proper understanding of annular flow pattern is required for accurate modelling of gas condensate wells to prevent liquification of the wellbore Figure 5.3b

(a) Annular flow gas fractions

(b) Annular flow in-situ velocity
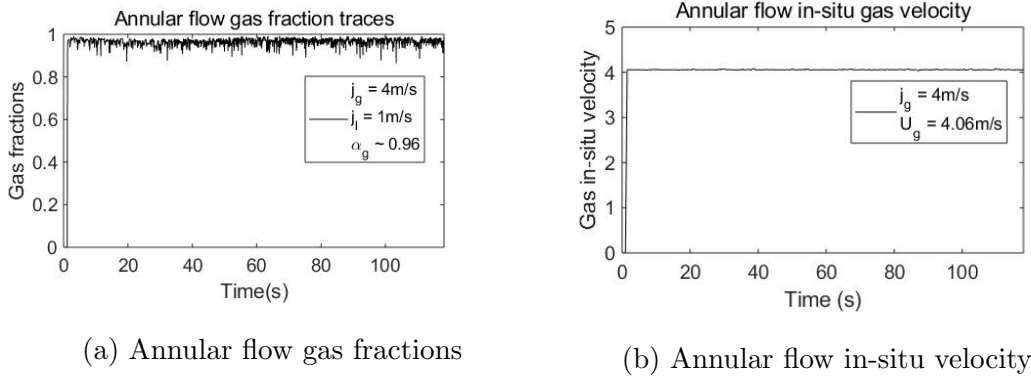
Figure 5.9: Annular Flow Time Averaged Gas Fractions and in-situ Velocity

5.3.2 Probability Density Function of Field Variables

To further investigate the flow patterns found in this research, the probability density function (PDF) traces were used in a manner similar to Rocha and Simões-Moreira (2008) and Costigan and Whalley (1997) to analyse the gas fractions. PDF is the probability that a time series data will have a specific value in a range of measured values

under consideration. In this research, the $ks - density$ function in Matlab was used to compute the occurrence probability distribution of the gas fractions, which is similar to the amplitude histogram. The comparison of the graphical plot of the PDF for bubbly, churn, semi-annular and annular flow is shown in Figure 5.10. As shown in the graphical plot, the CFD results appropriately compared with the experimental data set on all four types of flow plotted. However, some differences were noticed which may be as a results of experimental errors due to human interpretation, instrumentation calibration, setup and environmental factors. In addition, the CFD simulation may slightly be inaccurate due to selected model capabilities and setup. The differences were however within the limit of acceptable root mean square error as shown in Table 5.2.

(a) Bubbly Flow

(b) Churn Turbulent Flow

(c) Semi Annular Flow

(d) Annular Flow
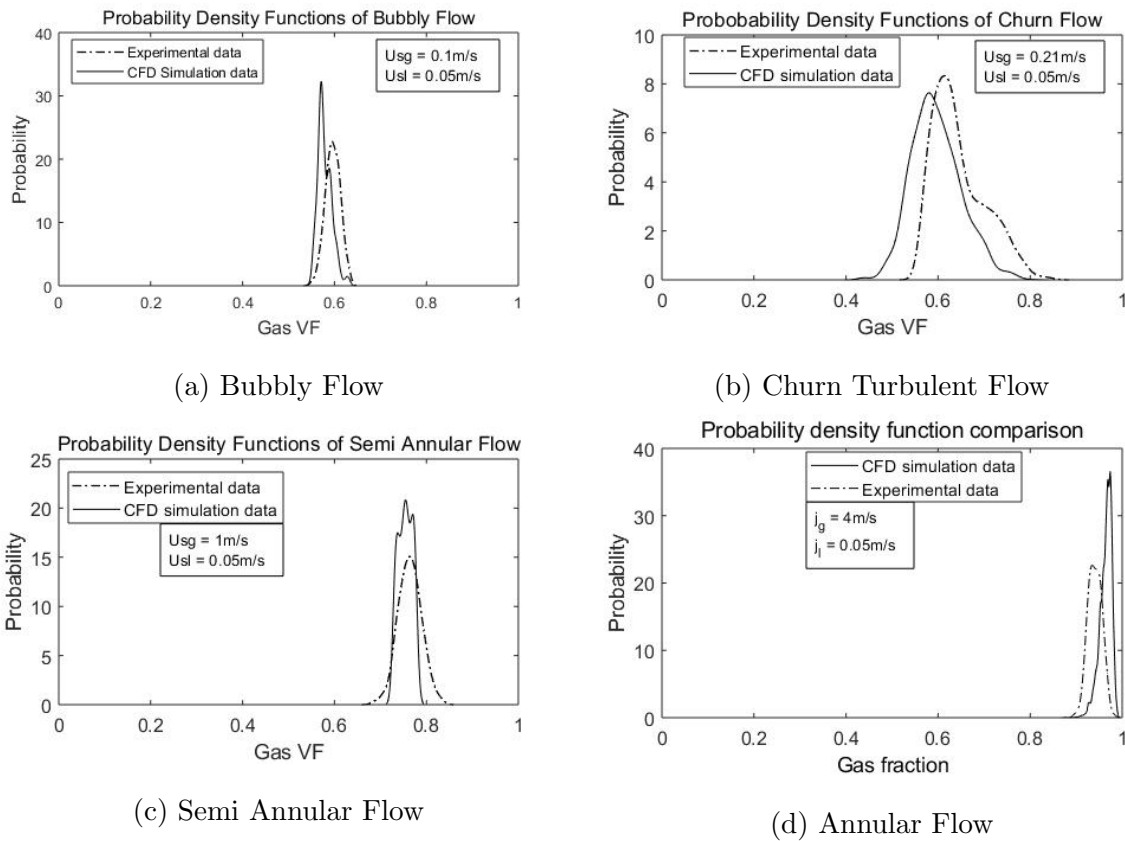
Figure 5.10: Probability Density Functions of Gas Volume Fractions Comparison

The graphical plot of the PDF traces of bubbly flow is shown in Figure 5.10a. The plot shows a narrow single modal peak at a volume fraction of 0.56, while the experimental modal peak void fraction is 0.6, which represent a close match to the published data. This trace shows the presence of group-2 bubbles discussed earlier, which means that the

bubbles are larger than the normal spherical bubbles seen in small diameter pipe.

Statistical analysis of the PDF traces of the churn flow time series gas volume fractions exhibited a peak that spiked at 0.58 while the experimental peak spike is 0.62. The tail end extended shortly to the high end of the scale as shown in Figure 5.10b. The histogram signature spreads out much wider than that of the bubbly flow which indicate a constant coalescence and breakup/destruction of the bubbles due to the swirl motion of the fluid system. The close match of the peak values of the bubbly and annular flow indicates the similarity between the group 2 bubble flow and the churn turbulent bubbles. The difference being that the churn flow has a wider spread which indicate larger bubbles than the bubbly counterpart even though the peak values are almost the same. In addition, the graphical plot shows that the traces of a bi-modal signature that characterises slug flow was not observed on the PDF graphical plot of the churn flow regime. Thus, the signatures that depict typical slug flow is not obtained in large diameter pipe. (Schlegel et al., 2009; Omebere-Iyari et al., 2007b; Prasser et al., 2005; Ohnuki and Akimoto, 2000, 1996). The PDF of the semi annular flow is shown in Figure 5.10c. The characteristic is similar to the churn bubbly flow but with the corresponding narrow peak occurring at the gas fraction of 0.75. The PDF exhibits a single peak with cone-like structure, similar to the histogram with the bubbly flow.

Similar statistical analysis was performed on the void fractions of the annular flow. The graphical plot is shown in Figure 5.10d. The PDF traces exhibit a single peak at a void fraction that is similar to the semi-annular flow. The single spike gas fractions magnitude is 0.95, while the experimental value is 0.92 which indicates a close match. The high gas fraction means that the liquid film is very thin and the gas core occupies almost the entire internal diameter of the pipe while the liquid flows along the wall. The gas superficial velocity has enough kinetic energy to carry the liquid droplets in the core without any fall back which ensures the momentum flux to maintain constant one directional upward flow.

5.3.3 Power Spectral Density of Field Variables

Statistical analysis of the time series void fraction signal $\alpha(t)$ into its power spectrum describes the distribution of power into discrete (spectrum) frequency components using Fourier analysis technique called Discrete Fourier Transform (DFT). A signal that would varies with time has a corresponding frequency spectrum which represent the power present in the signal. This is commonly expressed as watts per Hertz. The Power spectral density generally describes how power of time series signal is distributed over frequency. ANSYS CFD Post used and optimised algorithm called Fast Fourier transform (FFT) for the implementation of the DFT to obtain the PSD of a time series signal. In the FFT, two primary parameters to be made available are the sampling rate or sampling frequency (sampling per second) and the selected number of samples called the blocklength, often an integer to base 2.

The power spectral analysis of the gas volume fractions was obtained to further characterise the flow patterns. This was implemented using the Fast Fourier Transform (FFT) functionality which is built into the software libraries of ANSYS CFD Post. At the back-end, the Power Spectral Density (PSD) is obtained by Equation 5.7. The signatures of the frequency range for large diameter pipe is different from that obtained from small pipe but the interpretation of the regime follows the same logic.

$$PSD\left(x\right) = \left|F\left(x^2\right)\right| \tag{5.7}$$

where, $\left|F\left(x^2\right)\right|$ is the FFT of x.

As shown in Figure 5.11, the PSD traces from the bubbly churn to semi-annular flow follow similar trends. There is no one time single characteristic peak but most reasonable and equal sizes of bubbles that is characteristically decreasing to smaller bubbly frequencies. In the bubbly PSD traces shown in the graphical plot of Figure 5.11a, the power spectral peaked at a dominant frequency of 0.5Hz but ranges between 0-2Hz. The graphical plot of the churn flow PSD is shown in Figure 5.11b. The plot shows the bubbles are similarly packed with more bubbles, compares to the bubbly churn flow pattern. The PSD of churn flow is similar to that of churn bubbly flow. However, the frequency ranges from 0-4Hz which is widely spread than that of the bubbly flow. This wider frequency

(a) Bubbly Flow

(b) Churn Turbulent Flow

(c) Semi Annular Flow

(d) Annular Flow
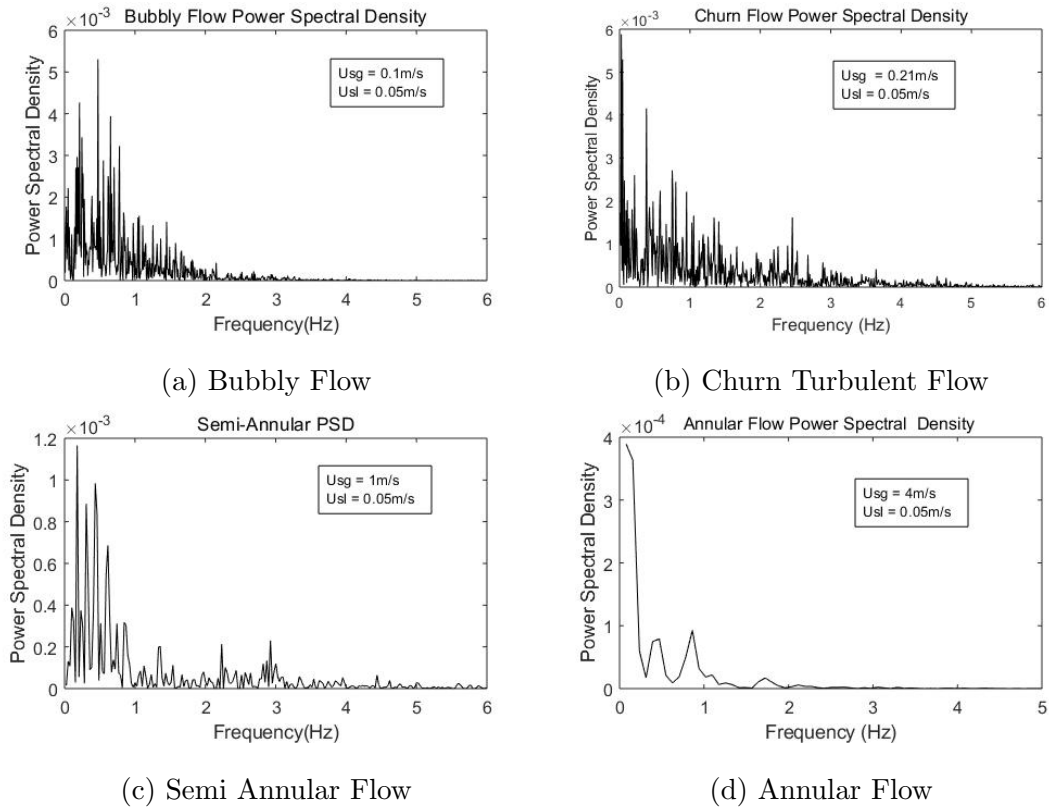
Figure 5.11: Power Spectral Density of Gas Volume Functions

distribution is synonymous to the gas fraction range seen in Figure 5.10b. This shows that there are larger bubbles and higher turbulence in the churn flow as a result of frequent coalescence and breakage of the bubbles. The PSD graphical plot of semi-annular flow is depicted in Figure 5.11c. The plot shows a continuous gas bubbles in the flow field which is loosely packed compared to the traces shown for the bubbly and turbulent churn flow. The PSD peaked between 0.1-0.7Hz (region of the centre core gas) but maintained low frequency upto 3Hz. This shows that there were liquids slug in the gas bubbles in the centre core. The annular flow PSD shows a continuous gas core peak with pocket of small bubbles entrained in the gas core. The PSD plot of the annular flow is shown in the graphical plot of Figure 5.11d.

5.3.4 Pressure Gradient and Turbulence Kinetic Energy

Further quantitative analysis was carried out to characterise the flow patterns. Pressure gradient and turbulent kinetic energy analysis were used to analyse the flow dynamics. Figure 5.12a and 5.12c show the pressure gradient comparison between this work and the

experimental work of Omebere-Iyari et al. (2007*b*) and Spedding et al. (1998) respectively. The pressure gradient result shown in the graphical plot of Figure 5.12a has an average of 2400Pa/m for the CFD and the experimental plot with similar perturbations. From Figure 5.6a and Figure 5.12a, the pressure gradient and the gas fraction traces of churn flow displayed similar perturbations. This suggests that there is a relationship between the gas fractions and the pressure gradient. Thus, pressure at any given point in the flow field is dependent on the gas fractions.

As the gas volume fraction increases at constant liquid rates, the pressure gradient continues to decrease from bubbly to annular flow but, with decreasing magnitude between semi annular and annular flow. Figure 5.12b shows the pressure gradient fluctuations obtained at 26.5 pipe diameter for each of the flow patterns observed in this research. The peaks and troughs displayed in the figure show higher liquid holdup and lower liquid holdup respectively. The frictional pressure drop due to high gas velocity is not obvious in the annular flow compares to the semi-annular flow. This may be due to the large internal surface area of the pipe. The perturbations in the bubbly flow pressure traces
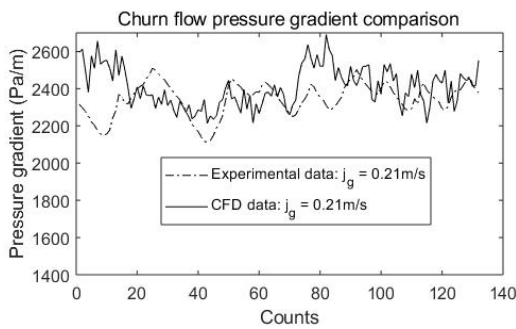
(a) Churn flow pressure gradient
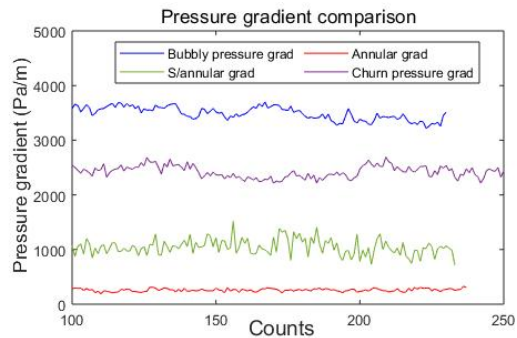
(b) CFD pressure gradient traces
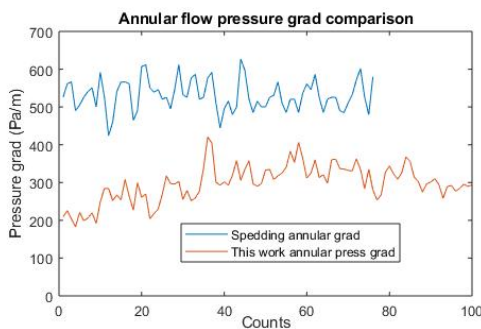
(c) Annular Pa/m comparison
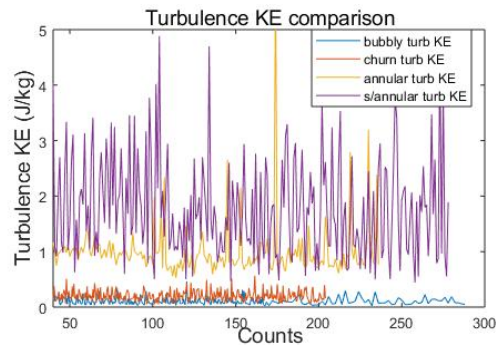
(d) Turbulent KE comparison

Figure 5.12: Pressure gradient and turbulence KE in large diameter pipe

has similar signature to the churn flow because the bubbles in the bubbly flow are typical of group-2 bubbles which are slightly smaller than the coalesced bubbles in the churn turbulent flow. The coalescence of the group-2 bubbles into churn turbulent and semi annular flow is exemplified in Figure 5.12b which shows a rather similar perturbation for these flow patterns. Thus, the semi annular flow field bears similarity to the churn flow though with higher gas fractions.

The turbulence kinetic energy, k or TKE in multi-phase flow is an important field variable that can provide useful information about the hydrodynamics of the flow field. As shown in Figure 5.12d, the turbulence kinetic energy in the semi annular flow pattern is slightly higher than that of the annular even though the gas superficial velocity of the latter is 4 magnitude higher than the former. The turbulence kinetic energy which is higher in semi-annular flow is as a result of the presence of more liquid particles entrained in the flow field. The intensity of the bubble induced turbulence is closely related to the TKE. This relationship is shown in Equation 5.8.

$$k = \frac{3}{2} \left(U_{avg} I \right)^2 \tag{5.8}$$

where the turbulent intensity I is given as:

$$I \equiv \frac{U'}{U_{avg}} = 0.16 \left(Re_{DH} \right)^{-1/8} \tag{5.9}$$

The turbulence length scale, l is related to the pipe diameter and the size of larger eddies available in the energy of the turbulent flows. The formulation of the length scale is given in Equation 5.10.

$$l = \frac{0.07 D}{C_\mu^{3/4}} \tag{5.10}$$

The specific turbulence dissipation rate within the length scale, ω can be described in Equation 5.11.

$$\omega = \frac{k^{1/2}}{C_\mu l} \tag{5.11}$$

Where, the reciprocal of $C_\mu^{3/4}$ is an empirical inverse proportionality constant that normalises the turbulence length scale for 1 and 2 equation turbulence model. I is the turbulence intensity, the RMS of the turbulent velocity to the average velocity, $Uavg$. In this work, the above formulations were invoked for the implicit computation by selecting

the intensity and hydraulic diameter in the turbulence specification model in the CFD code.

5.4 The Drift Flux Model

Two-phase flow involves some kind of relative flow between two fluids, hence the velocity field is important in solving two-phase flow problems. Two methodological approach to handling two-phase flow dynamics are the two-fluid model and the drift flux model. As stated earlier in the chapter 2, the most important factor in the drift flux formulation is the distribution parameter. This makes the difference between small and large diameter pipe. The CFD result from this research has been used to investigate how the distribution parameter changes in large diameter pipe across the flow regime spectrum based on the gas fraction changes and spread across the pipe cross-section.

5.4.1 Distribution Parameter in Larger Diameter Pipe

It is necessary to understand the physical meaning of the key terms used in relation to the drift flux model. The distribution parameter is related to the measure of the spread (concentration) of the gas fractions across the cross-section. Irrespective of wall peak and center peak ideology, it can be deduced that, for flows that have more liquid than gas concentration profile, the distribution parameter, C_o is less than 1, while for flows that have more gas than liquid concentration profile, the distribution parameter, C_o is greater than 1. Annular flow with gas fractions $\gg$ liquid fractions or approximate gas fraction of 1, the $C_o \approx 1$. The gas concentration profile plots obtained in this research for churn bubbly, churn turbulent, semi-annular and annular are shown in the graphical plot of Figure 5.13. The plot shows that there are more pronounce flatter profiles (wall peak profiles) from all the flow patterns which is similar to what is predicted in the experimental work of Omebere-Iyari et al. (2007b). Therefore, the distribution parameter, C_o obtained from this results should be close to 1, which is similar to the value obtained for churn flow from the benchmarked experimental results of Omebere-Iyari et al. (2007b).

The drift (rise) velocity depends on various parameters including the pipe diameter and the gas fractions. The rise velocity of the gas phase in a two phase flow system

(a) Bubbly flow gas vf profile

(b) Churn flow gas vf profile

(c) Semi annular flow gas vf profile

(d) Annular flow gas vf profile
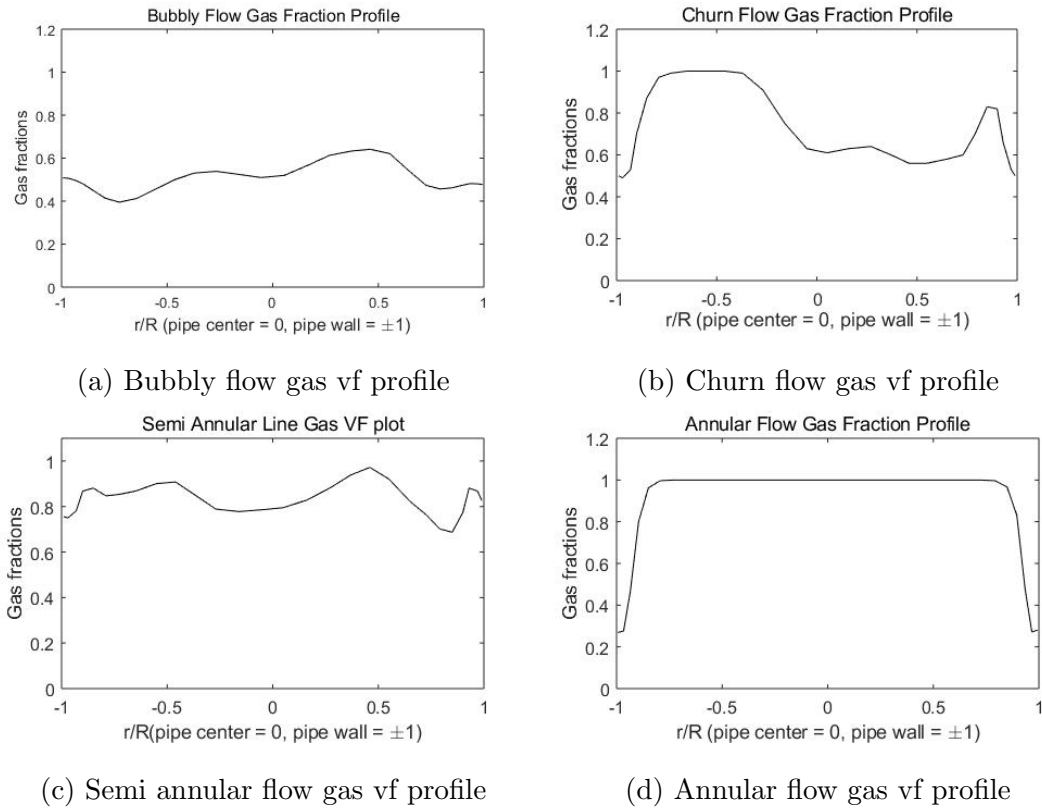
Figure 5.13: Instantaneous Gas vf Variation Across the Pipe Cross-Section

depends on the interaction between the buoyancy and interfacial drag as well as the pipe diameter, ie the interaction between gravity, buoyancy, surface tension and inertia force.

5.4.2 Drift Flux Correlation in Large Diameter Pipe

Two key unknown parameters that are required to develop a drift flux model are the distribution coefficient, C_o and the drift (rise) velocity, U_{gj} of the gas phase. These parameters are functions of the gas volume fractions. Hence, it becomes implicitly complex to develop a drift flux model from experimental data that suits all various conditions that respects the continuity criteria of C_o and U_{gj} in relation to the gas fraction. This has resulted in different values of C_o and U_{gj} that are proposed in literatures. Unlike the two-fluid model, the advantage of the drift flux model is due to the averaging of the variables which is easier to compute with a CFD code simulation.

From Equation 2.29, the distribution parameter can be calculated from the average gas volume fractions and the mixture superficial velocity while from Equation 2.30, the drift velocity can be calculated from the gas fractions and the local drift velocity. The CFD

code computation offers an advantage in calculating the mean values over a cross-sectional area (one dimensional values) and is therefore well suited for drift flux analysis.

Using the CFD post computational algorithm, the in-situ gas velocity was computed for the four test cases. Equation 2.31 was then used to evaluate the local drift velocity. The result of the four test cases is presented in Table 5.5. The results shown in the table

Table 5.5: Local Drift Velocity Values

Flow pattern	j_g(m/s)	U_g(m/s)	U_{gj}(m/s)	α_g
Bubbly flow	0.15	0.35	0.2	0.3-0.6
Churn	0.26	0.48	0.22	0.6-0.75
S/annular	1.05	1.5	0.45	0.8-0.9
Annular	4.05	4.06	0.01	0.9-0.99

indicates an interesting outcome. The local drift velocity increases until the semi-annular flow and then drop drastically at the annular flow. This snapshot result suggest that the annular flow could be treated differently from the other three flow patterns. The drift velocity for semi-annular is much higher than that of churn flow but lower than annular flow.

5.4.3 Flow Regime Map Development and Comparison

Determination of flow pattern is the central problem in two-phase flow hydrodynamics because almost all flow design variables are strongly dependent on the flow pattern. These design variables are, pressure drop, liquid hold up, heat and mass transfer coefficients, residence time and the rate of chemical reaction (Shoham, 2005). In this research, a flow regime map for large diameter pipe has been developed using results and data from the CFD simulation. Figure 5.14a shows the flow regime map developed in this research from the CFD results while the experimental flow map from Omebere-Iyari et al. (2007b) is shown in Figure 5.14b.

The nature of flow regime maps for large diameter pipe follows the exclusion of the classical slug flow and small spherical bubbles found in small diameter pipe flows. Using the same fluid superficial velocities, the CFD flow regime map appropriately matched

(a) CFD flow map

(b) Experimental flow map
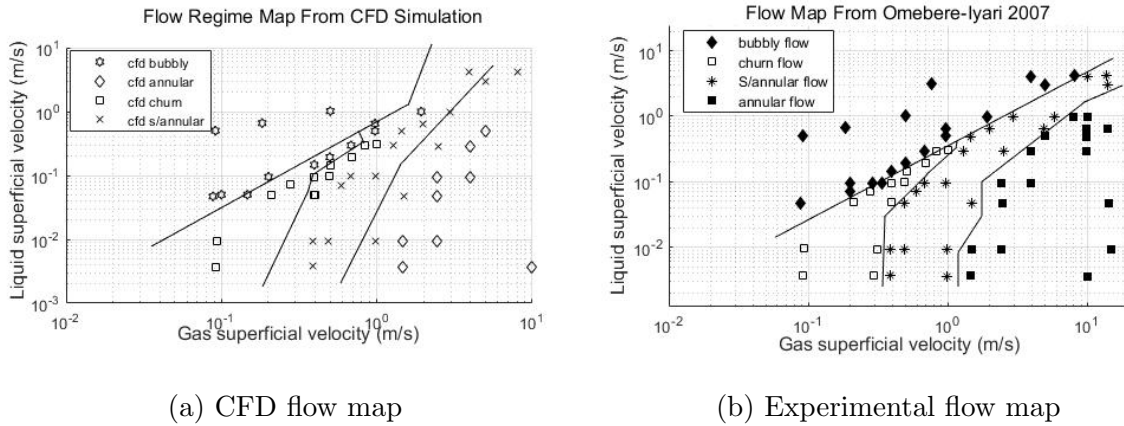
Figure 5.14: CFD and Omebere-Iyari et al. (2007b) Flow Map Comparison

the experimental flow regime map of Omebere-Iyari et al. (2007b). Although, some of the points at high gas and liquid superficial velocities that the authors have classified as churn bubbly flow produced semi annular flow in the CFD computation. This discrepancy may be due to measurement method or human error in the interpretation of the experimental results, instrumentation inaccuracy or calibration.

Ali and Yeung (2014a) performed experimental study with two-phase air-water flow in a 254mm diameter vertical pipe and developed a flow regime map from the results. The authors found that no slug flow regime was seen in their experiment. In addition, the description of the flow patterns is similar to the one described by other authors, though with some differences in the bubble description. Figure 5.15 shows the side by side comparison of the sketches of the authors flow pattern map and the flow pattern map & contour plots obtained from the present CFD simulation.

From Figure 5.15, it can be seen that there are similarities in the CFD churn bubbly and the experimental agitated bubbly as well as the CFD churn turbulent and the experimental churn/froth flow. The existence of the group-1 bubbles shown in experimental flow regime map, (Figure 5.15b) is not seen in the CFD flow regime map (Figure 5.15a). The CFD flow regime map confirms the characteristics of bubbles described by Schlegel and Hibiki (2015), that small spherical bubbles called group-1 bubbles are not seen in large diameter pipe flow structures. In this simulation, it was noticed that spherical and cap bubbles were not observed in the bubbly flow. This may be due to surface instability which accounts for the Rayleigh-Taylor instability in the upper

(a) CFD flow regime map

(b) Experimental flow regime map
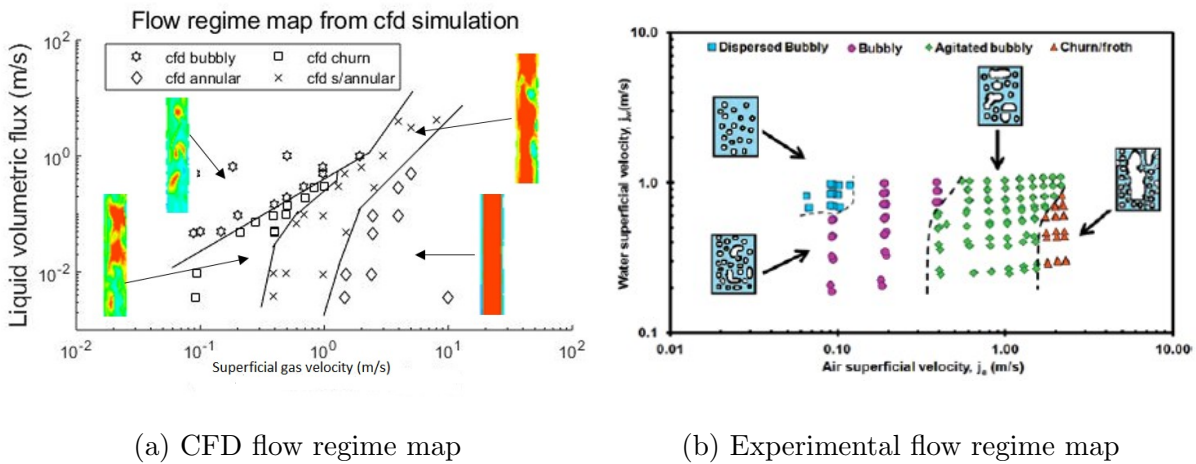
Figure 5.15: CFD and Ali and Yeung (2014a) Flow Regime Map Comparison

surface of the bubbles. Schlegel and Hibiki (2015) stated that this instability defines the maximum length scale in which a heavier fluid can rest upon a lighter fluid in a stable fashion. Depending on the radius of curvature of the bubbles, the surface tension and density differences plays major role in bubble stability. It is understood that the surface tension of a two-phase naphtha-nitrogen is less than half that of two-phase water-air flow. Hence, surface instability in oil and gas fluid is higher than that of water-air mixture.

(a) CFD flow map from this study

(b) Schlegel et al. (2009) flow map
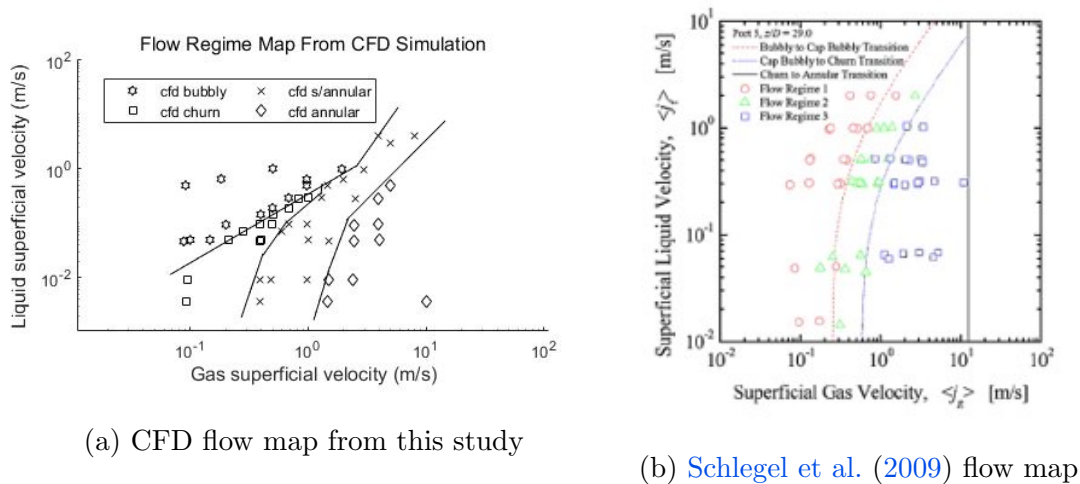
Figure 5.16: CFD and Schlegel et al. (2009) Flow Regime Maps

One of the most referenced large diameter pipe flow regime map is that of Schlegel et al. (2009). The author's experiment was performed in a 150mm diameter vertical pipe with data range of $0.01 \leq j_l \leq 1$m/s and $0.1 \leq j_g \leq 5.1$m/s for liquid and gas respectively. The gas fractions from the author's experiment were within $0.1 \leq \alpha_g \geq 0.83$ and the flow

structure description were bubbly, cap bubbly and churn turbulent flow patterns. There was no mention of semi-annular flow even at the gas fraction top end of 0.83. The major similarity here is that the author did not obtain slug flow even though their superficial velocities covered the range of slug flow seen in small diameter pipes. Schlegel et al. (2009) did not collect data for annular flow and recommended that further study should be performed for liquid superficial velocities greater than 1m/s to investigate the effect of increased turbulence on flow regime transitions. This increase turbulence is seen in this research in the semi annular flow which exhibited higher turbulence kinetic energy than any other flow pattern across the spectrum. Figure 5.16 shows the side by side flow pattern map comparison from this research work and that of Schlegel et al. (2009).

Comparison of flow regime maps is somewhat difficult because most regimes that were obtained in the past are not present in this work. Also, differences in fluid properties are often overlooked. Most importantly, personal and visual interpretation is important in the description of what is observed or not observed. In this study, attempt has been made to combine qualitative and quantitative analysis of the results to decide the name attributed to the flow pattern. Classical definition of flow patterns in large diameter pipe has been credited to Ohnuki and Akimoto (2000) who first gave the terminologies for large diameter flow patterns. The author's definition of flow patterns has been compared in this research from qualitative and quantitative point of view. Figure 5.17 shows this comparison.

From Figure 5.17, it can been seen that Ohnuki and Akimoto (2000) flow pattern contours is superimposed on the CFD flow map from this study. The authors' agitated and undisturbed bubbly were not found in most larger diameter pipes experiment as well as the CFD simulation results. However, the authors' churn bubbly and churn slug could well be described simply as churn bubbly and both fall within the churn bubbly regime of the CFD flow pattern. The authors' definition of churn-froth is also disputable. Depending on the length of the gas bubbles, though not shown, if much longer than the width of the pipe, it could be described as semi-annular flow because there is reasonable amount of liquid film flowing along the internal pipe wall.
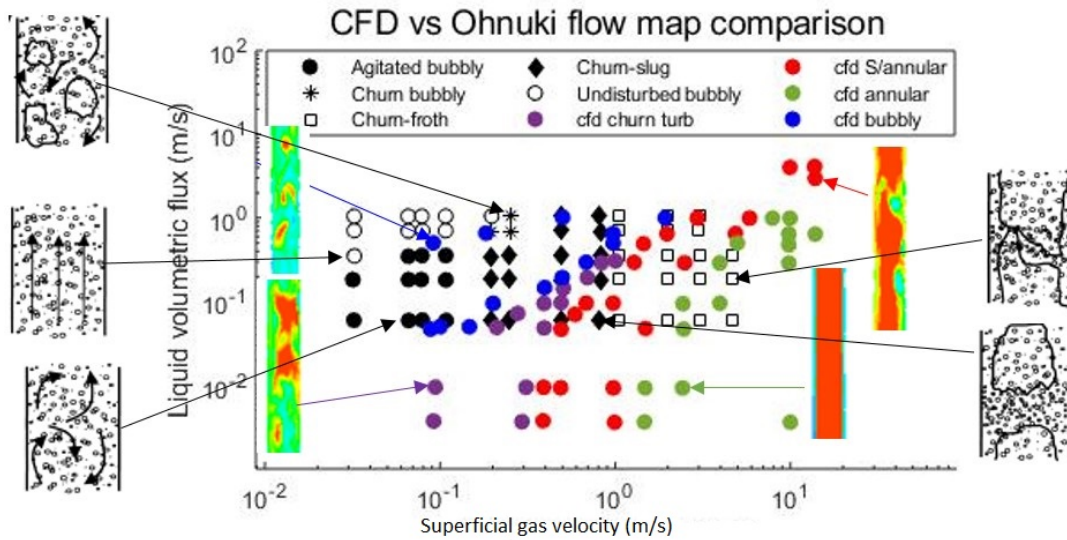
Figure 5.17: CFD Flow Regime Map vs Ohnuki and Akimoto (2000) Flow Regime Map

5.5 Summary of Two-Phase Flow Modelling

1. In this investigation, a CFD simulation was performed in the Eulerian framework for two-phase gas-liquid flows. The simulation data covers the full spectrum of the flow patterns seen in vertical pipe. Four distinct flow patterns were observed which are churn bubbly, churn turbulent, semi-annular and annular flow patterns. The outcome of the simulation was compared with the outcome of the experimental investigation of Omebere-Iyari et al. (2007b) and the match shows excellent agreement within the limit of acceptable root mean square error of 10%.

2. Qualitative and quantitative analysis were performed on all flow patterns identified and the field variables were analysed against experimental data set. The distinction of the bubbles were classified as group-2 bubbles inline with literatures using the classical void fraction analysis methodology.

3. The pressure gradients for all flow regimes were analysed and the changes and impact of bubbles and gas increase were obvious. The comparison of pressure gradient between experimental and CFD churn flow were appropriately matched. It was discovered that the impact of increase in gas flow on pressure gradient was not as aggressive as seen in small diameter pipe. The frictional pressure drop did not result

to a crossover of pressure drop between annular and churn/semi-annular flow. The reason for these findings may be as a result of large internal surface area of the large diameter pipe.

4. The turbulent kinetic energy comparison shows that the semi-annular flow exhibited the highest energy required for fluid transport in comparison to other flow patterns. Although, annular flow has a gas superficial velocity of 4X higher than the semi annular, the turbulence generated in the semi annular regime was higher than all flow regimes. This turbulence may be the reason for the higher turbulence kinetic energy observed. The effect of this turbulence is also seen at the drift velocity and kinetic energy which is also higher in semi-annular flow than other flow patterns.

5. The distribution parameter, C_o in large diameter pipe was analysed using the gas volume fraction sampling across the pipe cross-section in order to elucidate how this parameter is visualised across all flow spectrum. The result shows that the C_o can be $1 \leqslant C_o \geqslant 1$ between bubbly flow and semi annular flow but $C_o \approx 1$ for full annular flow regime. While the drift velocity increases up to maximum at the semi annular flow and then drops exponentially at the crossover to annular flow regime.

6. The critical gas volume fraction, and gas fraction range for large diameter pipe are different from those of small diameter pipe. Hence, correlations developed for small diameter pipes may not be suitable for design and analysis of larger diameter pipe flow properties and hydrodynamic predictions.

7. Finally, flow regime maps were generated for large diameter pipe and compared with experimental results. The findings indicate that the flow regime maps for small diameter pipe are also different from those of large diameter pipe. Comparison with other literatures reveal that the classification of the morphological definitions are sometimes subjective and based on the limitation of the data range and the methodology used in the analysis.

THREE-PHASE FLOW RESULT & ANALYSIS

In chapter 5, a two-phase gas-liquid flow CFD computational simulation was performed. Detailed two-phase flow analysis was carried out to determine various hydrodynamic field variables of multi-phase flow in large diameter vertical pipe. In this chapter, this investigation is extended to three-phase gas-liquid-solid flows in large diameter vertical pipe. The previously validated CFD model on two-phase flow is used to investigate the impact of sand presence in the flow hydrodynamics. This investigation is critical for the process and energy industries where fluid and particle flow takes place. While most researchers had investigated two-phase fluid flow only and developed models from their experimental investigations, there are little reports in the public domain that talk about three-phase gas-liquid-solid flows. This gap will be filled with this investigation.

In the previous chapter, the study of two-phase flow is extensively investigated across the flow pattern spectrum. In this chapter, only the churn turbulent flow has been investigated. The impact of sand presence in the flow scheme has been evaluated. This include impact on the bubble coalescence, fluid flow, mass flux effect, sand transportation and pressure drop in a typical vertical flow production system.

6.1   Gas-Liquid-Solid CFD Model

The mathematical modelling equations for three-phase gas-liquid-solid multi-phase flow is presented in subsection 3.4.1 and 3.4.2. The simulation model is implemented in ANSYS Fluent software in a manner similar to the framework depicted in option C of Figure 4.1 in chapter 4. In this framework, the three-phases are inter-penetrating and continuous. The initial stage is the simulation of two-phase nitrogen-naphtha fluid flow. The numerical

scheme has been validated with published experimental data set of Omebere-Iyari et al. (2007*b*). This model is then extended to include another Eulerian secondary phase which gave rise to the multi-fluid Euler-Euler-Euler approach in a manner similar to Li and Zhong (2015) three-phase gas-liquid-solid CFD simulation in a bubble column. Interaction between these three-phases is permitted through the interfacial forces according to model C of Figure 4.1. This triple Euler CFD model is used to numerically solve the sets of equations earlier described for three-phase flows. Appropriate numerical scheme and closure law models for the interface transfer forces and turbulent flow were selected to simulate the hydrodynamic parameters. These are gas volume fraction, solid holdup and in-situ axial velocities.

The study of turbulence models and interfacial forces are the main aspects for the investigation of three phase bubble column systems (Li and Zhong, 2015; Pourtousi et al., 2014), and proper solutions depends on the correct choice for these models. Hence the turbulence model chosen was first validated in chapter 4 and then extended to study the three-phase flow. For the purpose of clarity, the closure laws pertinent to this three-phase modelling are given below:

6.2 Solid Pressure and Shear Stress Closure Laws

There are two models used to model the solid pressure in the Eulerian multi-fluid VOF computation. The normal stress is as a result of particle-particle interaction and this account for the solid pressure. To model this solid pressure, two available methods are the constant volume model (CVM) where the dynamic viscosity is a constant value, and the kinetic theory of granular flow (KTGF) model. The KTGF model is mostly effective when considering particle-particle interaction. The CVM is simpler and less computationally intensive while the KTGF is more computationally involving. The solid pressure is prevalent when the solid volume fraction approaches packing limit. In this research, the solid volume fraction is low at low sand concentration and will not near the packing limit even at the high end of flow time and thus particle-particle interaction may not be significant. However, at higher sand concentration of $\geqslant 2.5\%$, the sand deposition at the bottom of the pipe is near the packing limit at the high end of the simulation time.

Therefore the KTGF model is deemed useful to capture the overall pressure gradient in the flow scheme and was used in the investigation. More importantly, it is necessary to compute the turbulent intensities which is expressed in the granular temperature.

In addition to the solid pressure described above, the kinetic theory of granular flow (KTGF) is also use to model the solid stress present in the solid momentum equation. A key parameter in the KTGF closure models for solids phase stress is a parameter known as granular temperature. The granular temperature provides a measure of the energy associated with solid particle fluctuations at isothermal conditions. The intensity of the random variable properties is manifested in the solid pressure and viscosity of the solids. In the research, the granular temperature is models algebraically rather resolving the full transport equation.

6.3 Closure Laws for Interfacial Force

The interfacial momentum exchange force is considered in this investigation for the transport and interaction of the three phases. The simulated model C of Figure 4.1 shows the interaction of the phases which are continuously inter-penetrating. The forces involve in the momentum transfer are represented as M_i in Equation 4.7 which are: virtual mass, lift force, drag force, turbulence dispersion and turbulence interaction forces. The wall lubrication force was ignored in the three-phase investigation as Fluent does not capture it in the flow dynamics for three-phase simulation. The virtual mass and the lift force contribution, though infinitesimal but, were computed. Critical forces considered are the drag force, turbulent dispersion and interaction force. The drag force is the main force that is responsible for the transport of the sand particles without which the sand will not be transported. The turbulence dispersion is responsible for the interaction of the dispersed phases with the continuous phase. Details of these forces and formulations are given in subsection 3.5.1 and subsection 3.5.2.

6.4 Turbulence Model

In order to investigate the impact of sand inclusion in the flow field, the validated model for the two-phase flow is used in this three-phase investigation. The turbulence model, k-ω initially used in the two-phase flow was retained in the three-phase flow computation. The mixture turbulence model is selected for the flow simulation. The effect of turbulent fluctuation of the velocity stream and other flow properties is captured. The interaction of the phases are three ways, gas-liquid, solid-liquid and gas-solid interactions.

6.5 Description of The Gas-Liquid-Solid Cases

The three-phase gas-liquid-solid flow investigation is conducted to evaluate the impact of sand particles on the multi-phase flow hydrodynamics in large diameter vertical pipe. The objective is to investigate the effect of solid on the flow pattern and the effect of solid concentration on sand transport and deposition in large diameter pipes while the superficial velocities of the phases are kept constant. The triple Euler model shown earlier on is used for this investigation. The domain and boundary conditions are similar to that used in two-phase flow model investigation in chapter 5. However, gas and solid phases were introduced into the domain through a single center inlet at the same velocity, while the liquid phase was introduced through the pipe annular circumference in a similar manner to the two-phase flow. Figure 6.1 shows the inlet cross sectional boundary for the three-phase flow geometry. The outlet boundary is a single pressure outlet at atmospheric pressure while the inlets are velocity controlled.

The case investigated for sand impact were those of churn flow which were already validated in the previous chapter. The physical properties of the fluid system is shown in Table 4.1, while the process parameters and cases investigated is shown in Table 6.1 Two approaches were used to test the validity of the strategy used in the computation. The first was the addition of sand particles through the gas inlet of completed and stabilised churn flow. While the second approach was to run a fresh three-phase gas-liquid-solid flow in a triple Euler framework. The results of the two approaches were the same. In order to obtain a stable and converged solution, the under relaxation factors were adjusted lower
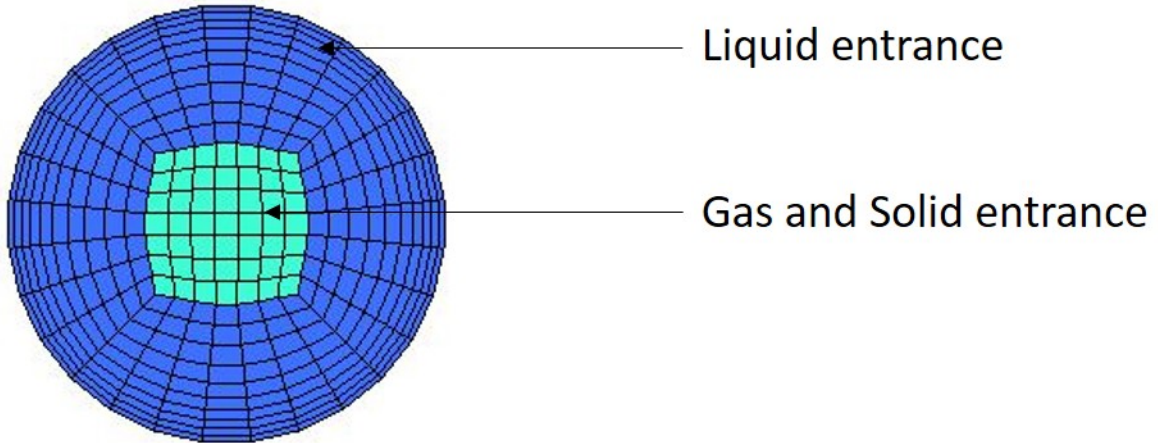
Figure 6.1: Three-Phase Inlet BD Conditions

Table 6.1: Three-Phase Cases and Process Parameters

.

churn-sand cases	U_l(m/s)	U_g(m/s)	U_s(m/s)	% sand	sand (kg/s)	%gas	% liquid
Case 1	0.0593	1.3359	1.3359	0.1	0.0146	99.9	100
Case 2	0.0593	1.3359	1.3359	2.5	0.365	97.5	100
Case 3	0.0593	1.3359	1.3359	5.0	0.73	95	100

than the Fluent default settings. The time step of 0.001s was used. The pressure based solver which is used for the computation requires under relaxation factors for all equations to be set. Five equations were solved which are flow, volume fraction, turbulence, energy and inter-facial area concentration (IAC). The under relaxation factors used are shown in Table 6.2.

Table 6.2: Three-Phase Under Relaxation Factor

press.	momentum	vol.frac	gran.tempt	TKE	spec diss.	turb.visc	iac
0.2	0.4	0.5	0.2	0.8	0.8	0.8	0.3

6.6 Three-Phase Results, Validation and Discussion

6.6.1 Basis of Validation of CFD Results

Earlier in the preceding chapters, appropriate numerical schemes and drag models were selected to simulate a two-phase gas-liquid flow in a larger diameter vertical pipe. The hybrid model was able to replicate all flow patterns and matched against published experimental results. In this chapter, this model is extended to investigate the flow dynamic of a gas-liquid-solid flow in a piping system similar to the one used in the gas-liquid flow simulation. However, few researchers have experimented gas-liquid-solid flow in a large diameter pipe, while others have performed CFD computation of gas-liquid-solid flow in bubble columns and fluidised bed similar to the three-phase flow investigated in this research.

Li and Zhong (2015) performed a CFD simulation of gas-liquid-solid flow to investigate the flow dynamics in bubble columns using the Triple Euler numerical scheme. The authors investigated different drag models and the impact of gas superficial velocity, solid volume fraction, particle size and density on the flow dynamics. The gas superficial velocity and the solid volume fraction used covers similar range used in the present work. Earlier on, Rampure et al. (2003) performed experimental and CFD investigation of gas-liquid and gas-liquid-solid flows in bubble columns in a 200mm diameter pipe. Li and Zhong (2015) had validated their CFD results against the experimental results of Rampure et al. (2003), hence both of these works are used to validate the results from this research.

The closure laws for gas-liquid-solid modelling depicted in Figure 4.1 was earlier validated by Xu et al. (2014) and later by Li and Zhong (2015). Closure Model option B and C were tested by the latter while option D was tested by the former using Euler-Euler approach with a population balance model. In this research closure model B and C were tested but C was used for the final simulation. It is important to note that Li and Zhong (2015) had used Zhang and Vanderheyden (2002) model for gas-liquid momentum exchange forces and Schiller and Naumann (1935) formulation for liquid-solid interface forces and none for the dispersed gas-solid interphase. In this research, Anisotropic drag

Table 6.3: Physical Properties and Parameters Compared

Parameters	Li and Zhong (2015) & Rampure (2003)	This work
pipe diameter (mm)	200	189
gas superficial velocity (m/s)	0.22, 0.2	0.21
gas phase	air	nitrogen
gas density (kg/m)	1.225	23.4
gas phase viscosity (Pa.s)	1.7894e-05	1.77e-05
liquid phase	water	naphtha
liquid phase density (kg/m)	998.2	702.3
liquid phase viscosity (Pa.s)	1.003e-03	3.59e-04
solid phase	glass powder	sand
solid phase density (kg/m)	2400, 2500	2500
solid phase avg size (μ m)	270, 450	250
solid phase vf	0.02, 0.03, 0.05	0.025, 0.05
liquid surface tension (n/m)	0.072	0.0185

law is used for gas-liquid momentum exchange force and Schiller and Naumann (1935) model is used for both liquid-solid and gas-solid interface force transfer. This selection produced stabilised and converged solution. On turbulence modelling, Li and Zhong (2015) used the RNG k-ε while Standard k-ω is used in this study. The k-ω is tested and validated in this research to be more suited for flow transitions across all flow patterns and is thus retained for the three-phase flow.

In addition, this research implemented the IATE model with the Eaulerian model instead of the complex population balance model proposed by Xu et al. (2014) to capture the bubbles coalescence and breakup. Recently, Kim et al. (2021) opined that the IATE is capable of modelling and predicting the IAC in a two fluid model and is thus suitable for closing the two-fluid model without flow regime dependent correlations. Although, the IATE was initially developed for bubbly flows, the authors also claimed that the IATE

can be extended beyond bubbly-churn to churn-annular transitions and annular flows. This IATE capability is tested in the present work and validated in the two-phase flow simulation.

6.6.2 Physical Properties and Parameters Comparison

Most of the experimental and computational work carried out by researchers were for convenience and safety reasons, performed with air-water-sand three phase flows. Due to the peculiarity of this research work, the fluid system used is three-phase Nitrogen-Naphtha-sand flows. However, the trend of the compared CFD results of Li and Zhong (2015) and the experimental results of Rampure et al. (2003) with this research outcome exhibited similar signatures and thus appropriately compared. While various parameters were investigated by the authors however, in this research, the comparison is only done on similar parameters to establish congruence and basis for further analysis, conclusion and recommendation from this research work. Table 6.3 shows the extracted matching physical properties of the fluid system and parameters used for the validation of this work.

6.6.3 Results Comparison

This chapter deals with the three-phase gas-liquid-solid flows in large diameter vertical pipes. But as earlier stated, the three-phase simulation is only done for the churn flow pattern, hence data relating to the gas superficial velocity that are capable of generating churn flow are used for this comparison and validation of the results. These data sets have been extracted and depicted in Table 6.3. The CFD work of Li and Zhong (2015) and the experimental work of Rampure et al. (2003) fell within this limits and is thus used for comparison.

6.6.3.1 Contour Plots Comparison for Similar Parameters

The graphical contour plots for gas, liquid and solids from the work of Li and Zhong (2015) was compared with the results of this research. Figure 6.2 and Figure 6.3 show the instantaneous static plots for the three-phases with approximately same gas superficial
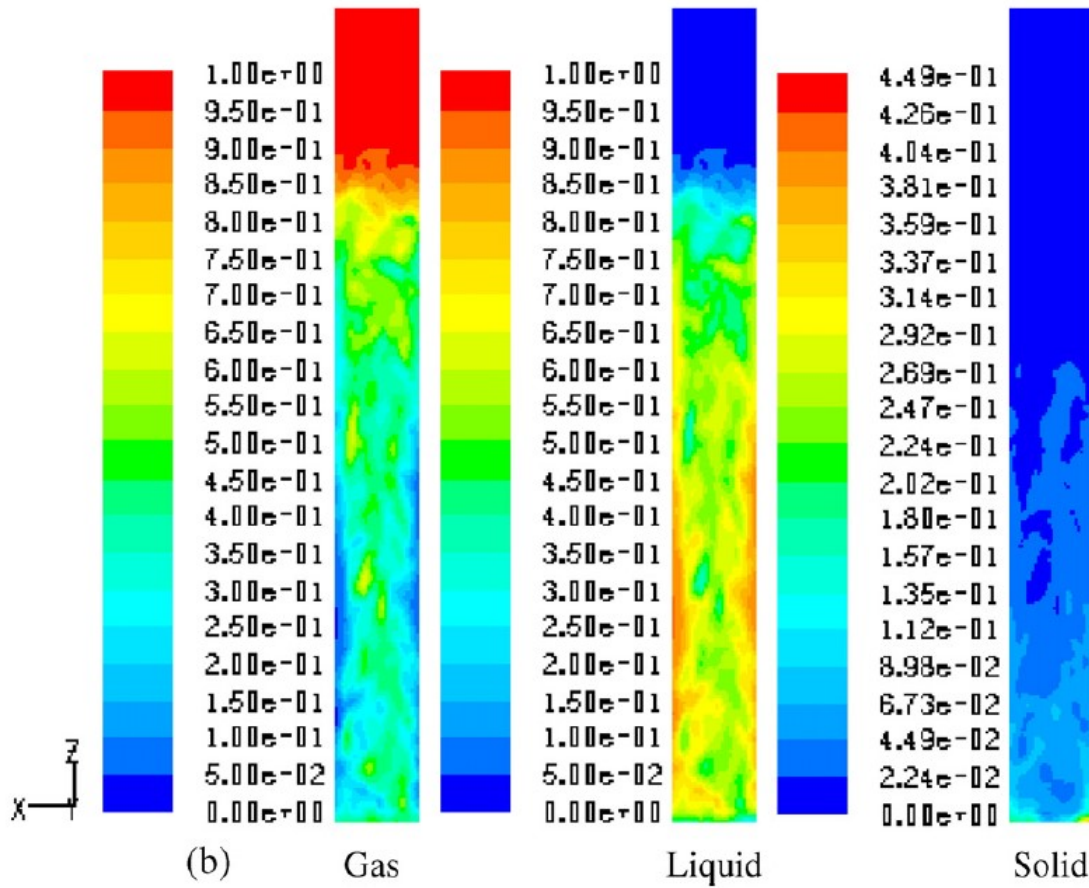
Figure 6.2: Li and Zhong (2015): sand vf = 5% and j_g =0.2m/s

velocity (0.20 and 0.21m/s) and sand volume fraction of 5%. From the plots, it can be seen that the gas bubbles displayed similar churn-like breakup bubbles for both work. The liquid contours also shows great resemblance. The key comparison is the sand volume fraction and the deposition. In both qualitative plots, it can be deduced that most of the sand particles were deposited at the bottom on the pipe and less were transported up the pipe.

Understanding the impact of sand loading in the distribution and deposition is important to estimate the quantity of sand that is transportable to the surface and determine if the carrier superficial velocity alone is enough to estimate sand transportation. In this simulation, sand concentration was increased in 3 steps of 0.1%, 2.5% and 5% in a churn turbulent flow scheme. Earlier on, Rampure et al. (2003) performed an experiment to determine the effect of solid loading on the solid volume fraction and deposition in a cylindrical bubble column for 1%, 5% and 10% inlet sand concentration. Figure 6.4 and Figure 6.5 show the qualitative plots for comparison of

126
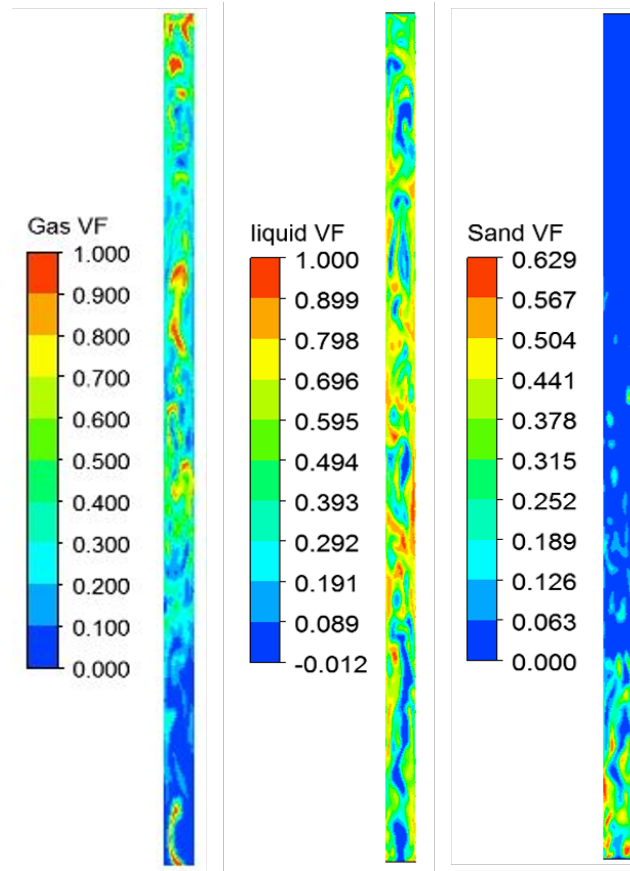
Figure 6.3: Present Study: sand vf = 5% and j_g =0.21m/s

the outcome of the CFD and experimental results. It can be deduced from these plots that as the inlet sand volume fraction increase, the sand transportation energy reduces. Thus, the sand deposition increases at the same fluid velocity. The CFD results from this research and the experimental work of Rampure et al. (2003) showed similar trend and it can therefore be concluded that the outcomes compared appropriately for further analysis. Sand loading or deposition thus increases with inlet sand intake.

6.6.3.2 Quantitative Solid Loading Comparison

Quantitative plots of three phase simulation involving sand either in experimental and CFD simulations outcomes shows that not all the sand particles are transported to the surface even at high velocities. Li and Zhong (2015) simulated various gas superficial velocities that covers up to the churn flow region. Similarly, Rampure et al. (2003) also investigated the three-phase flow dynamics behaviour for superficial velocities of up to 0.20m/s with 5% sand volume fraction in a 200mm diameter cylindrical column with
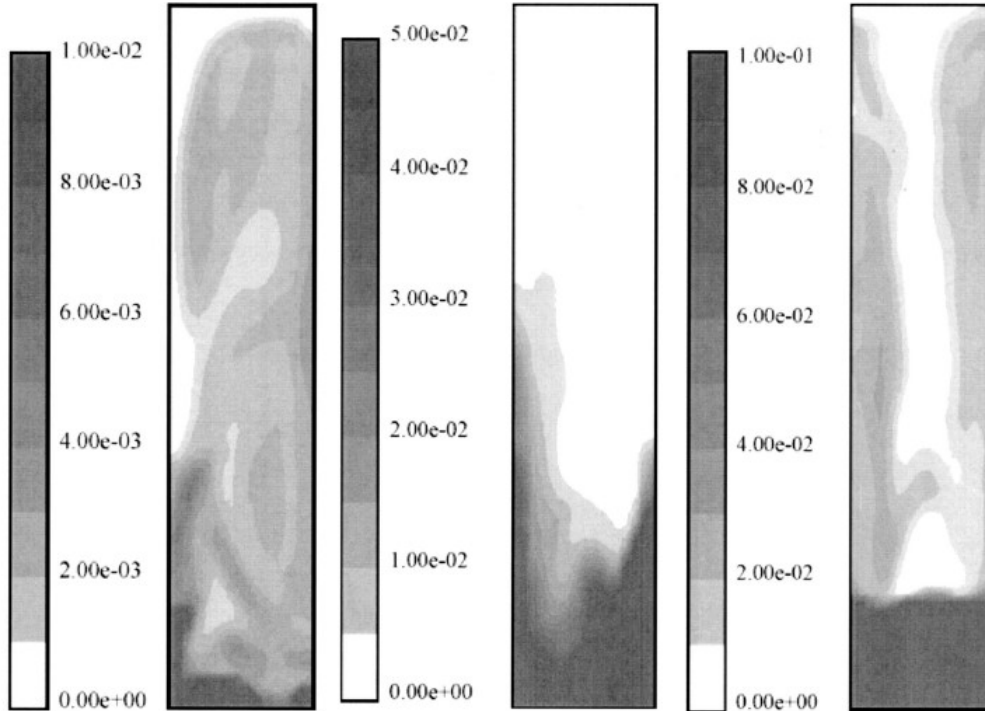
Figure 6.4: Rampure et al. (2003): Effect of Sand vf; 1%, 5% and 10% on Sand Deposition

a sparging inlet. The axial and radial profile of the sand volume fractions of both the CFDs and experimental outcomes are shown in the graphical plot of Figure 6.6. From Figure 6.6a, it can be seen that the CFD simulation of gas-liquid-solid fractions for the three cases investigated exhibited similar trend of sand deposition. Irrespective of the sand volume fraction, less sand reaches the outlet of the pipe. Earlier on, Rampure et al. (2003) performed similar experiment to investigate the impact of solid volume fraction loading on deposition and transport Figure 6.6b. The author also found out that irrespective of the inlet volume fraction, less of the solid particles actually arrived at the surface of the pipe. This is similar to what is obtained in this research simulation. This again establishes the validity of the results obtained from this work.

In addition, Li and Zhong (2015) performed a CFD study to investigate the effect of gas velocity at constant sand volume fraction of 5%. The authors discovered that although, the increase in the fluid superficial velocity leads to increase in sand transportation, the deposition of sand at the bottom still remains an issue. Figure 6.6c shows the sand deposition trend which indicates that increasing the velocity alone is not the only factor that helps to unload the sand.
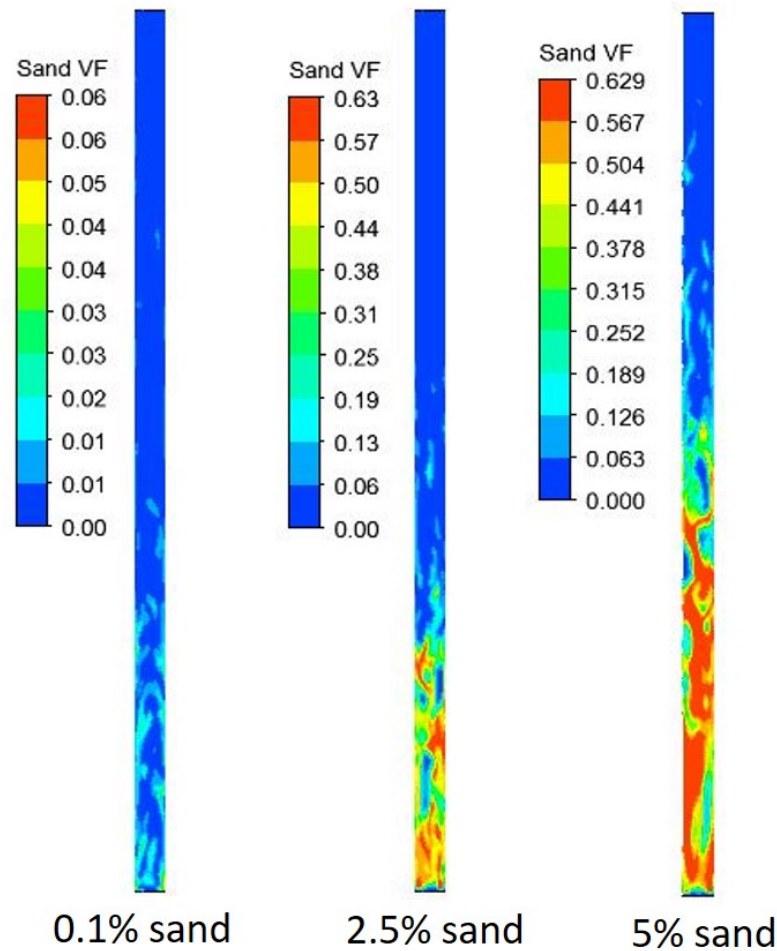
Figure 6.5: Research CFD: Effect of Sand vf; 0.1%, 2.5% and 5% on Sand Deposition

Figure 6.6d shows the non-dimensional radial sand profile at different axial height. The graphical plot confirms the fact that sand settlement is higher at the bottom of the pipe and decrease axially to the top of the pipe. The profile also indicates the turbulent nature of the sand particles in the flow field which is the expected profile of turbulence churn flow.

6.7   Effect of Solids on Dynamic Flow Properties

The three-phase gas-liquid-solid flow simulation was carried and validated with published CFD simulation and experimental data set of Li and Zhong (2015) and Rampure et al. (2003) on similar input data. This comparison gave credence to further investigation and analysis of the flow variables that are impacted by the presence of solid particles in the flow scheme. The following sections deal with the analysis of the changes on the dynamic

(a) Research CFD axial sand profile

(b) Rampure et al.(2003) axial sand profile

(c) Li and Zhong (2015) axial sand profile

(d) Research CFD radial sand profile
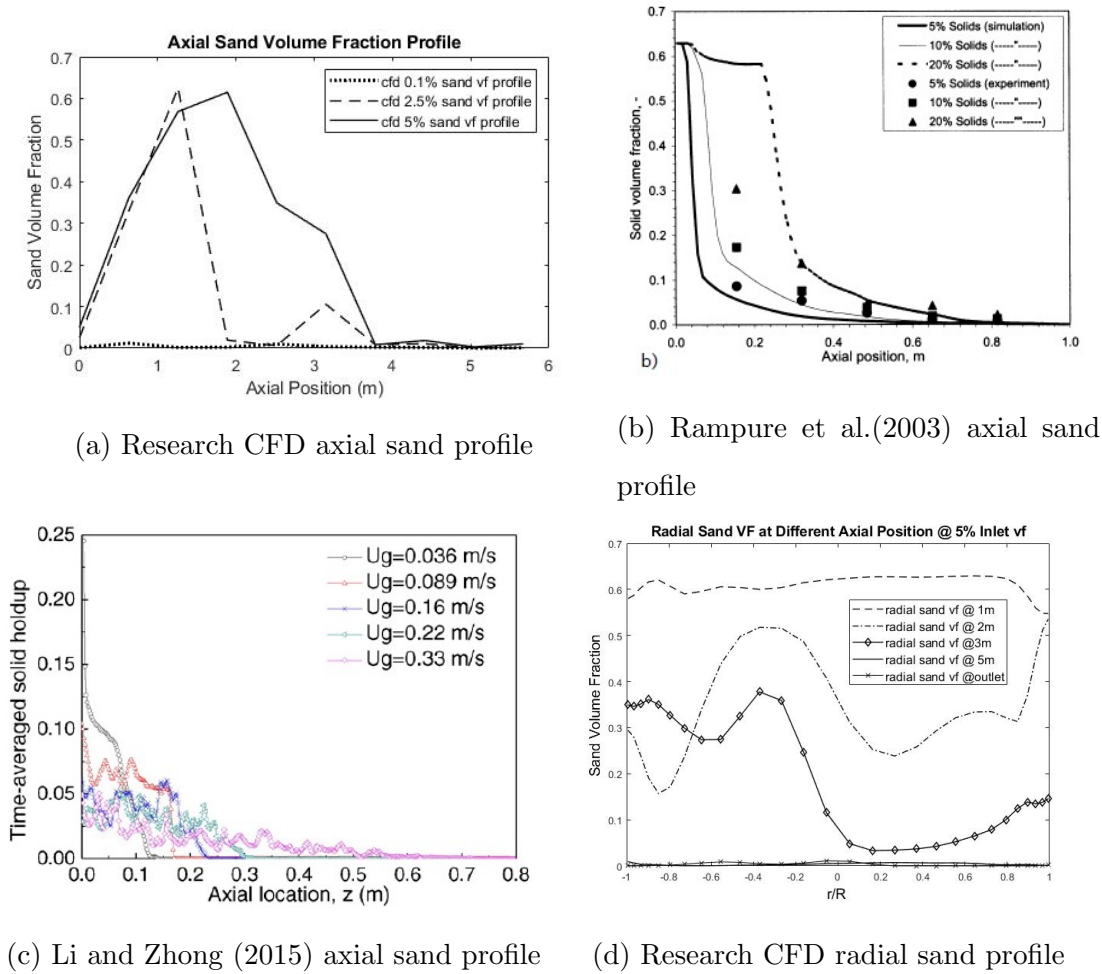
Figure 6.6: Axial/Radial Sand Profile Comparison

flow properties of three-phase flow with solid particles.

6.7.1 Qualitative Plot of Phase Fractions

The CFD methodology avails the opportunity to symmetrically view the internal topology of the phase arrangement in the flow field. The qualitative plot gives the instantaneous static view of the phase arrangements in the flow field similar to the camera view. While keeping the velocity constant, the sand concentration was varied in three different steps and the results were extracted and qualitatively analysed.

Although all the cases of the three-phase flow have the same inlet gas and sand velocity, the gas bubbles were affected by the presence of the sand particles in the flow field. With the presence of sand, bubbles were not close to one another in comparison to the flow field of cases without sand presence. Thus, the mass flux or concentration is an important

parameter to consider in the investigation of the hydrodynamics and transportation of sand in a three-phase gas-liquid-solid flows.

In this research, the solid (sand) velocity was kept constant while the concentration was varied in three steps of 0.1, 2.5 and 5% to study transportation of solid particles in the flow field. In the computation, the three phases were inter-penetrating and this heterogeneous mixture is possible by the turbulence dispersion and interaction forces. The formulation model of Simonin and Viollet (1990) is used to model the turbulence dispersion of the gas-solid and solid-liquid dispersion forces, while the formulation of Troshko and Hassan (2001) is used to compute the turbulence interaction forces between the gas and liquid. Table 6.1 shows the variability of the parameters investigated. The solid volume fractions were monitored and extracted at 6 axial locations of 1m, 2m, 3m, 4m, 5m and 5.5m. The qualitative results and discussion of the outcome are presented in the next sections.
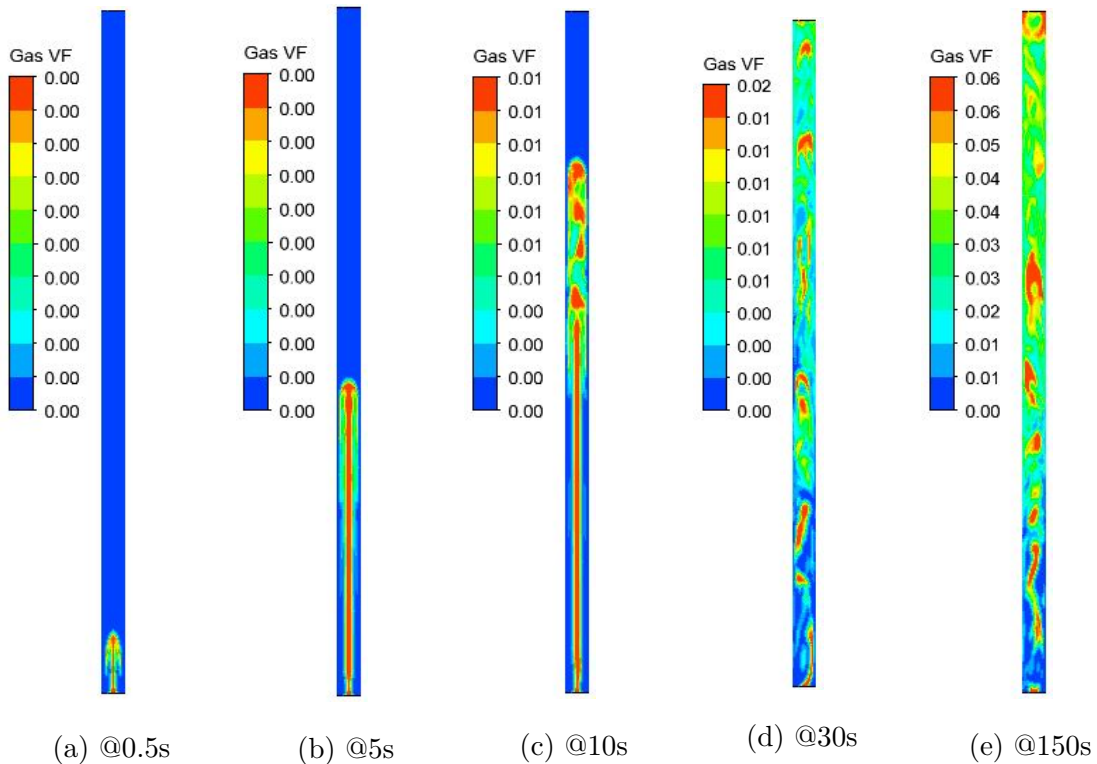
Figure 6.7: Instantaneous Gas VF in Presence of 0.1% Sand Concentration

6.7.1.1   Case 1 - 0.1% Sand Concentration

The first study of the three-phase gas-liquid-solid flow is carried out by introducing 0.1% sand concentration to the flow field of a two-phase gas-liquid flows. The result of the

computation is presented in this section. From Table 6.1, 0.1% sand concentration is equivalent to a mass flux of 0.0146kg/s. The entrance velocity for secondary sand and gas phase is 1.3359m/s. Qualitative plots for different flow time to investigate gas movement in a three-phase flows is presented in Figure 6.7. The plots show the geometrical topology of the gas fractions at various time steps. It can be seen from the plot that the gas volume fractions did not break up on time but continue to travel on a straight line up to half length of the pipe @ 10sec. At fully developed flow @150secs, the gas Taylor bubbles had sheared off and coalescence into large bubbles were rare. The simulation animation is shown in this video which shows the complete flow from developing to fully developed flow.

(a) @0.5s   (b) @5s   (c) @10s   (d) @30s   (e) @150s
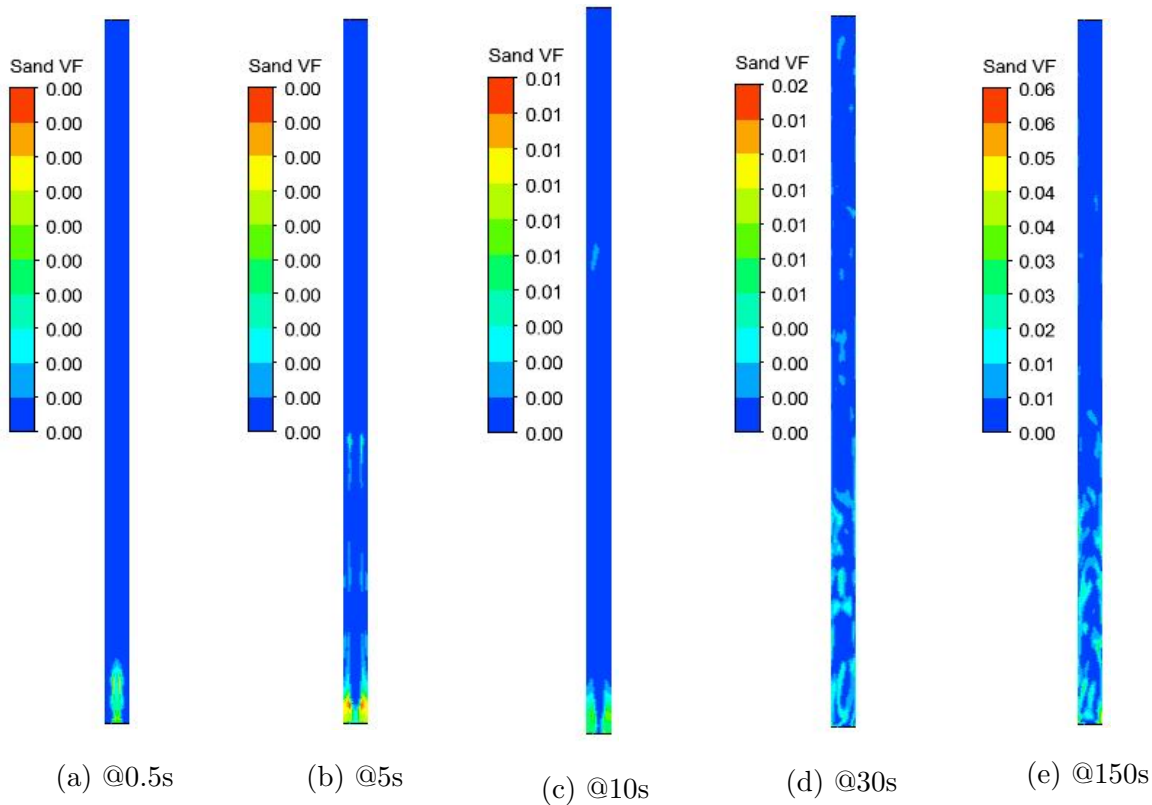
Figure 6.8: Instantaneous sand VF in presence of 0.1% sand concentration

Similarly, Figure 6.8 shows the solid flow qualitative plot which indicate how solid transport in vertical pipe takes place. From the figure, it can be seen that some sand particles were transported to the surface but majority of the solid articles were settled at the bottom even from the outset. At fully developed flow @150s, the particles could hardly move up to the surface. The result shows sand particles will settle at the bottom

of the pipe at any time when there is sand inflows to the wellbore. The amount of sand that gets to the surface is less than the total sand inflow into the pipe. The simulation animation of the sand flow is shown in this [image], which present the complete flow from developing to fully developed flow.

6.7.1.2   Case 2 - 2.5% Sand Concentration

Three-phase gas-liquid-solid flow with 2.5% sand concentration is also investigated. As shown in Table 6.1, the sand mass flux for this case is 0.365kg/s and the sand velocity is 1.3359m/s at the gas inlet. Liquid and gas velocities remain the same at 0.0593 and 1.3359m/s respectively.

Figure 6.9 shows the instantaneous sand volume fraction for 2.5% sand concentration in a typical churn flow simulation. The qualitative plots indicate that the gas particles travel at the pipe center of the pipe but slower and then breaks up into longer slug of gas bubbles from 30s. At fully developed flow, the gas bubbles were much smaller than that of the case for 0.1% and zero sand concentration. The simulation animation of the gas flow @2.5% sand concentration is shown in this [image], which present the complete flow from developing to fully developed flow.

Similarly, Figure 6.10 indicate sand flow for this case. It can be seen that the sand deposition is higher in the 2.5% sand concentration than the 0.1% sand concentration. The sand particles reaching the top of the pipe is lower than that for 0.1% sand even though the same velocity applies for both cases. At fully developed flow of 150s, the sand bed deposition is higher for 2.5% than that of the 0.1% sand concentration. The simulation animation of the sand flow @2.5% sand concentration is shown in this [image], which present the complete flow from developing to fully developed flow.

6.7.1.3   Case 3 - 5% Sand Concentration

In this final case, the sand volume fraction of 5% concentration was introduced into the flow scheme. The sand mass flow is equivalent to the flux of 0.73kg/s. The inlet sand and gas velocity is 1.3359m/s. The entrance orifice is through the pipe center. Thus, the dispersed phases, gas and sand were made to enter the flow field through the center.

(a) @0.5s (b) @5s (c) @10s (d) @30s (e) @150s
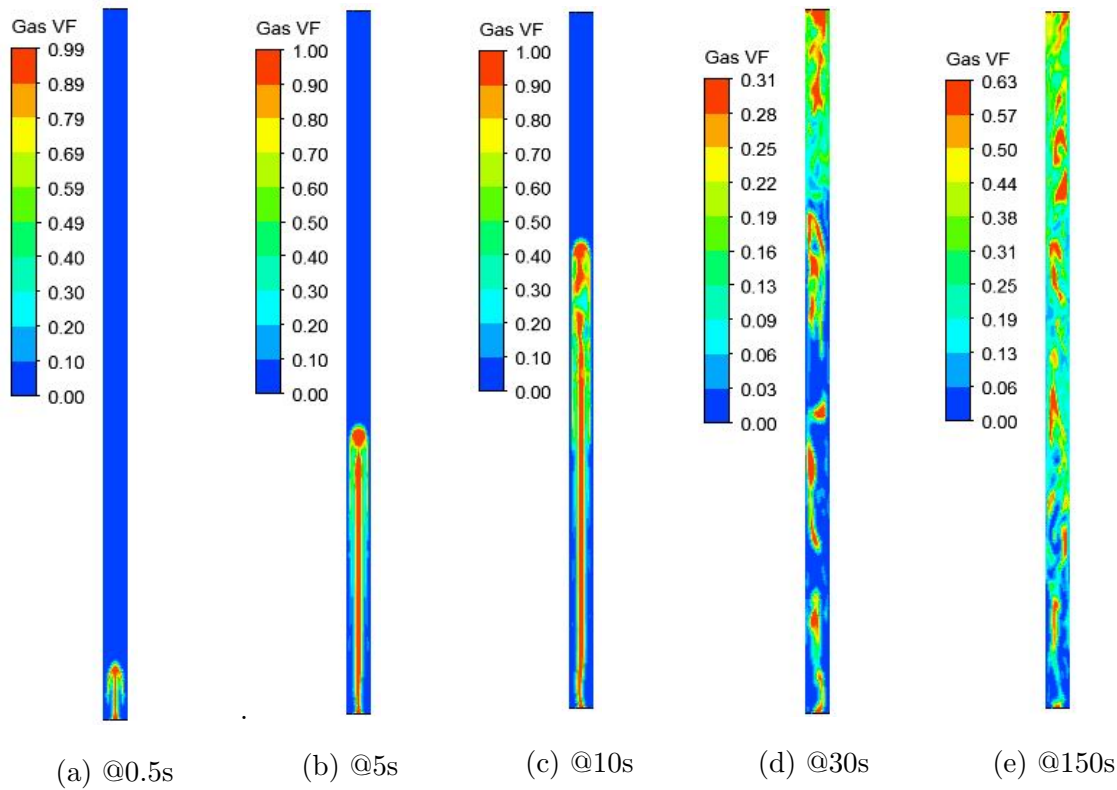
Figure 6.9: Instantaneous Gas VF in Presence of 2.5% Sand

Figure 6.11 shows the instantaneous static qualitative plot of the gas volume fraction flow at 5% sand concentration. The result is similar to that of the 2.5% sand concentration and at fully developed flow of 150s, where the gas bubbles were smaller than the counterpart for 0.1% sand concentration. It is obvious that as the sand concentration increases, the fluid volumetric flow reduces. The simulation animation of the gas flow in 5% sand concentration is shown in this [⬛]o, which present the complete flow from developing to fully developed flow.

In like manner, Figure 6.12 shows the sand flow volume fraction contour plot. From contour plot, it can be seen that the sand particles were deposited at the bottom of the pipe up to about half length of the pipe. The deposited sand bed is highly fluidised as the gas and liquid peculates through the sand bed with little restriction. Although the initial gas and liquid velocity were the same, but not much of the sand particles were able to flow to the top of the pipe unlike the two previous cases. Thus the higher the sand concentration, the higher the sand deposition at the bottom on the pipe. Hence, it can then be concluded that the sand deposition at the bottom of the pipe is a function of the

(a) @0.5s   (b) @5s   (c) @10s   (d) @30s   (e) @150s
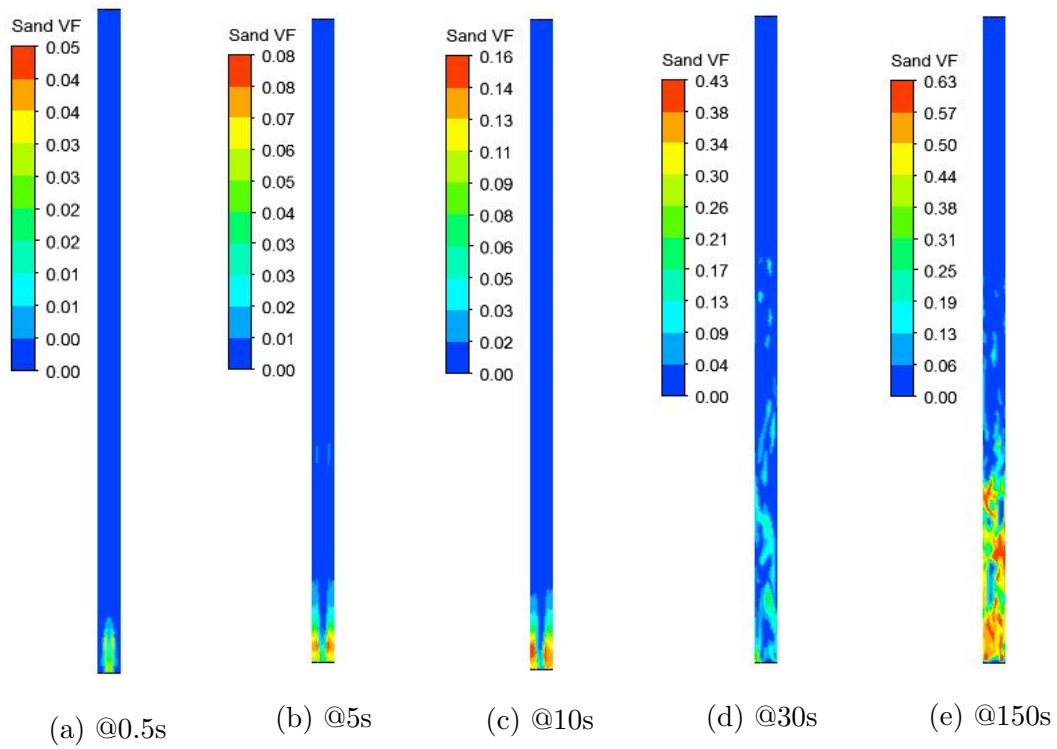
Figure 6.10: Instantaneous Sand VF in Presence of 2.5% Sand

(a) @0.5s   (b) @5s   (c) @10s   (d) @30s   (e) @150s
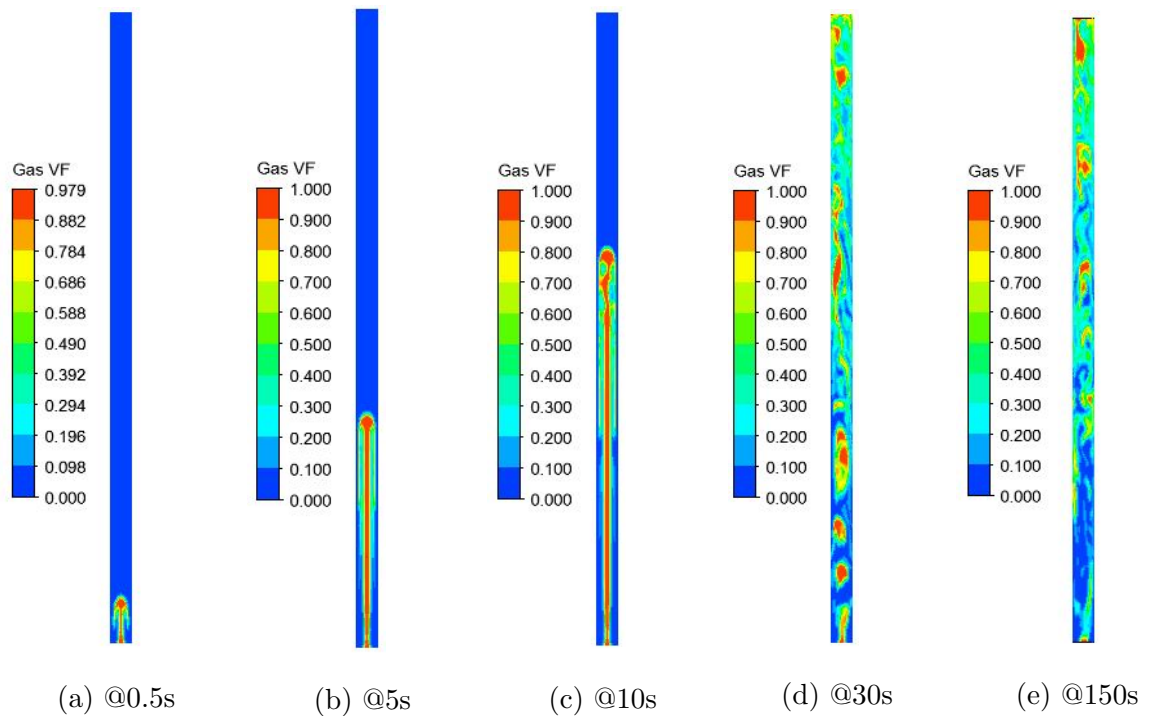
Figure 6.11: Instantaneous Gas VF in Presence of 5% Sand

sand inflows (sand concentration) and not only on the system velocity. The simulation animation of the sand flow in 5% sand concentration is shown in this ▶, which present

135

the complete flow from developing to fully developed flow. From the foregoing, it can also be observed that the gas particle coalescence was less and is inversely proportional to the sand concentration. This is due to the increase instability at the interface of the gas bubbles which leads to shearing off and destruction of the bubbles.

(a) @0.5s   (b) @5s   (c) @10s   (d) @30s   (e) @150s
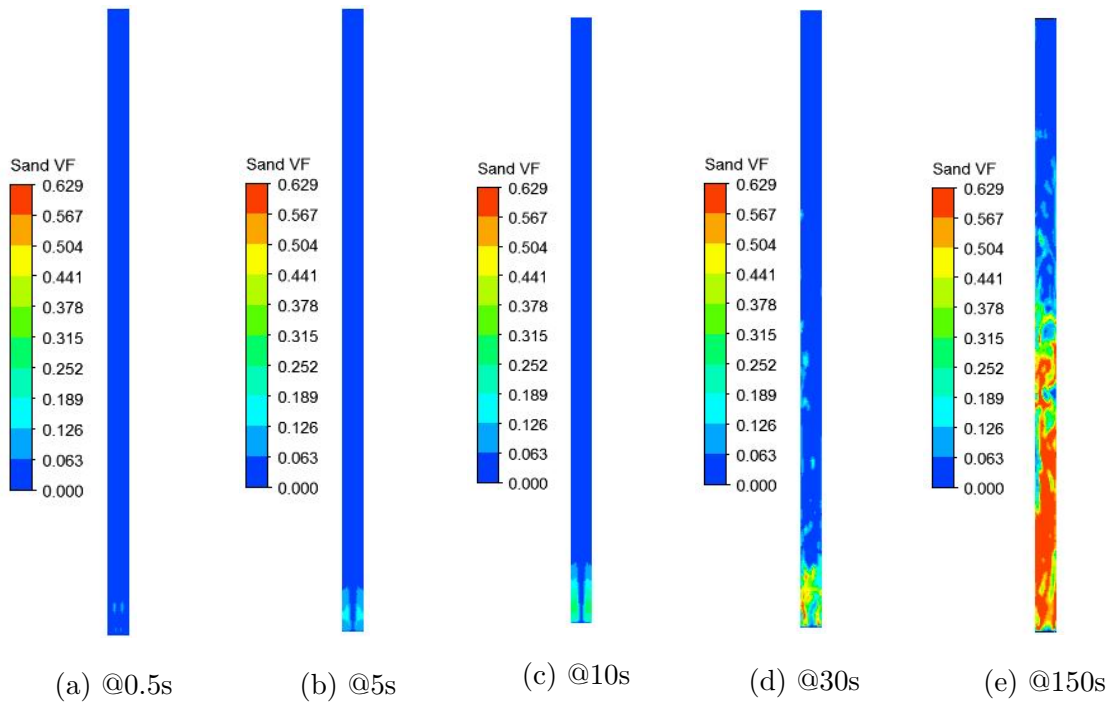
Figure 6.12: Instantaneous Sand VF in Presence of 5% Sand Concentration

6.7.2 Quantitative Analysis of Field Variables.

The impact of sand particles can also be understood with quantitative analysis of the different field variables. In this section, changes in the field variables are analysed and compared in a churn flow environment. Comparison with sand-free churn flow was also performed. The results exemplify the impact of sand particles in the flow field and overall sand transportation in the piping system. This is presented in the following subsections.

6.7.2.1 Gas Volume Fractions Traces

The typical instantaneous gas volume fraction traces were compared for 0%, 0.1%, 2.5% and 5% sand concentration flow scheme. The results are shown in the graphical plot of Figure 6.13. From the plot it can been seen that as the sand concentration increases,

(a) Sand-free churn flow gas vf profile

(b) 0.1% sand in churn flow gas vf profile

(c) 2.5% sand in churn flow gas vf profile

(d) 5% sand in churn flow gas vf profile
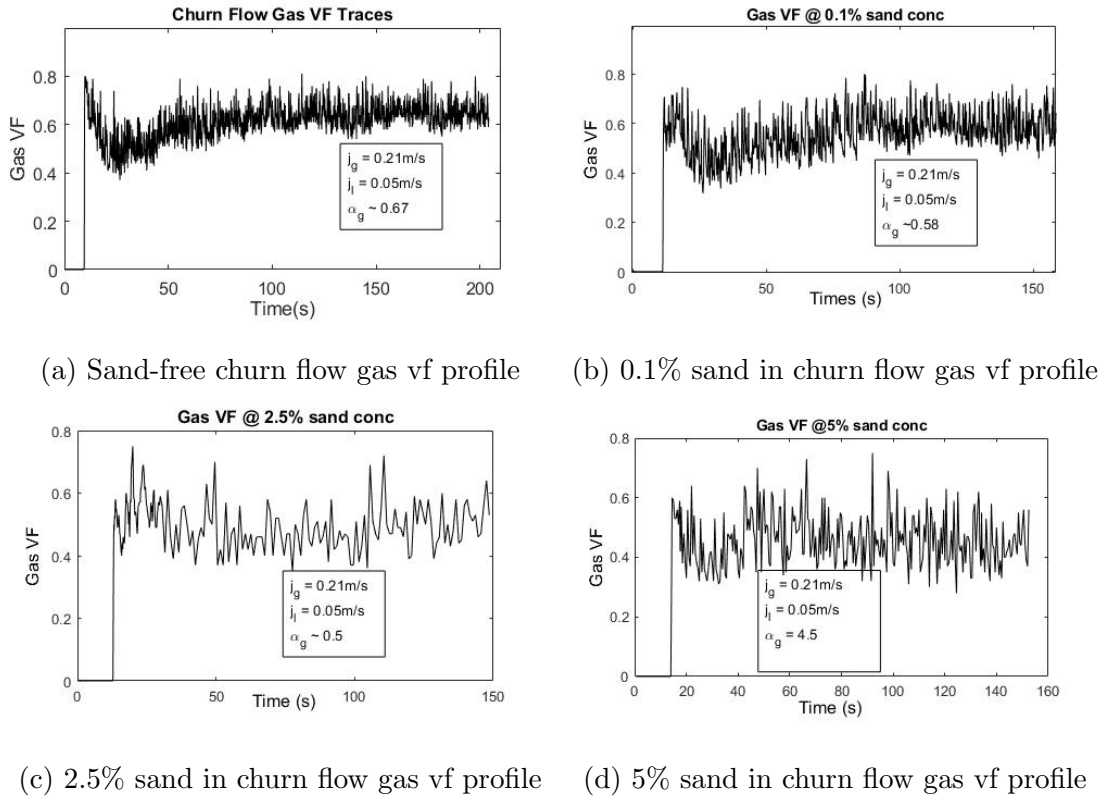
Figure 6.13: Gas Volume Fraction Comparison in Different Sand Regime

the gas volume fraction decreases but not proportionally. The time averaged gas volume fractions are 0.66 for no sand flow, 0.6 for 0.1% sand concentration, 0.5 for 2.5% sand concentration and 0.45 for 5% sand concentration. This decrease in gas volume fraction means that the gas flow is reduced. This confirms the assertion that when sand begins to flow into the pipe from the wellbore, the fluid production is cut back due to reduction in available area open for flow. This leads to production drop in a typical industrial production system in the petroleum industry.

6.7.2.2 Gas Phase Velocity Traces

The cross-sectional instantaneous in-situ gas velocity was computed at the height of 5m and compared with the two phase results. The graphical plot of Figure 6.14 shows that the in-situ gas velocity is ≈ 0.48m/s for sand free churn flow. This velocity is slightly increased to ≈ 0.57m/s at the high end of 5% sand concentration. The little change in the velocity indicates complete fluidisation at 5% sand concentration even at high packing limit experienced at fully develop flow. These little changes are amplified in the pressure

gradient as indicated in subsubsection 6.7.2.3.

(a) sand-free churn flow gas velocity profile

(b) 0.1%sand-in-churn flow gas velocity

(c) 2.5%sand-in-churn flow gas velocity

(d) 5%sand-in-churn flow gas velocity
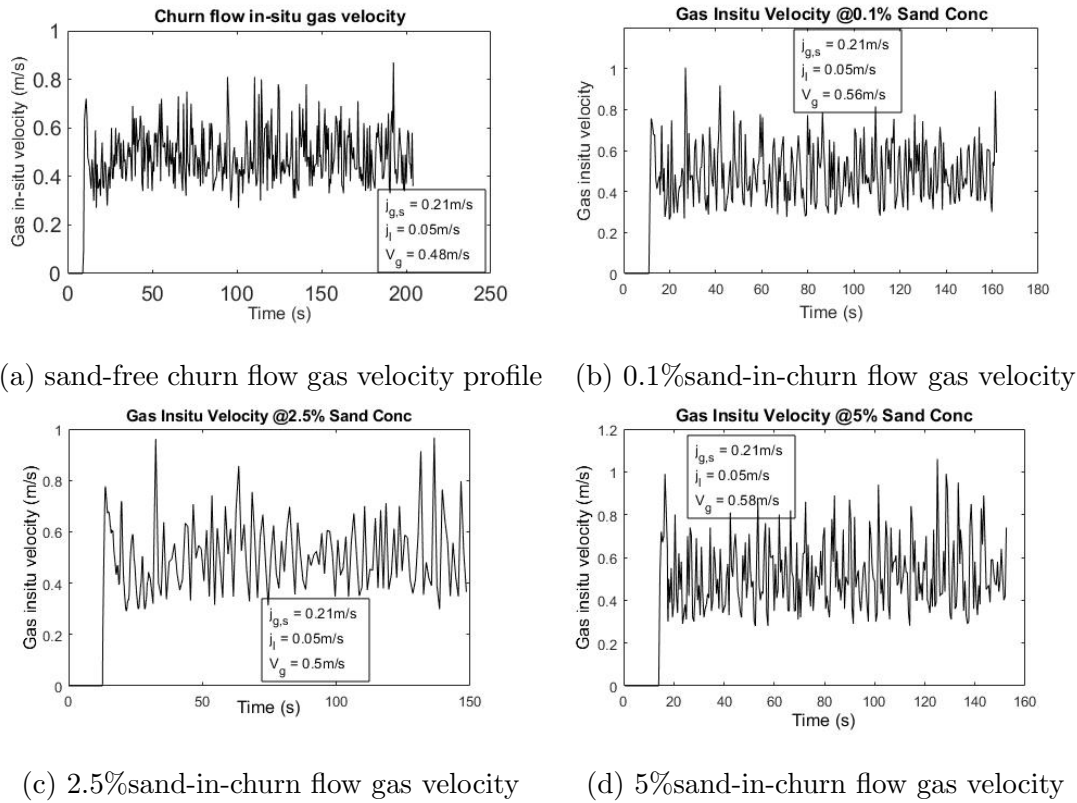
Figure 6.14: Gas Velocity Comparison in Different Sand Regime at 5m Height

6.7.2.3   Sand VF Impact on Pressure Gradient and Transportation

The impact of sand production is highly felt in the pressure gradient parameter, a significant factor that account for energy reduction in the system. The graphical plot of Figure 6.15a shows the pressure gradient variation. The plot shows the effect on pressure drop in the system due to the presence of sand particles. Effective sand and fluid transportation depends on available pressure to transport the fluids. It is observed that the pressure gradient begin to increase even as low as 0.1% of sand concentration from ≈ 2500Pa/m to ≈ 2900Pa/m. This difference in pressure gradient is equivalent to the energy lost due to solids particles and causes transportation problem and eventual deposition of solids particles.

Further investigation of the impact of sand on the flow scheme is shown in Figure 6.15b - 6.15d. The graphical plots show that the sand volume fraction seen at the pipe outlet are 0.0002 for 0.1% while that of 2.5% and 5% sand are equal by one magnitude higher than

(a) Impact of Sand on Pressure Gradient

(b) Outlet Sand VF @0.1% Sand

(c) Outlet Sand VF @2.5% Sand

(d) Outlet Sand VF @5% Sand
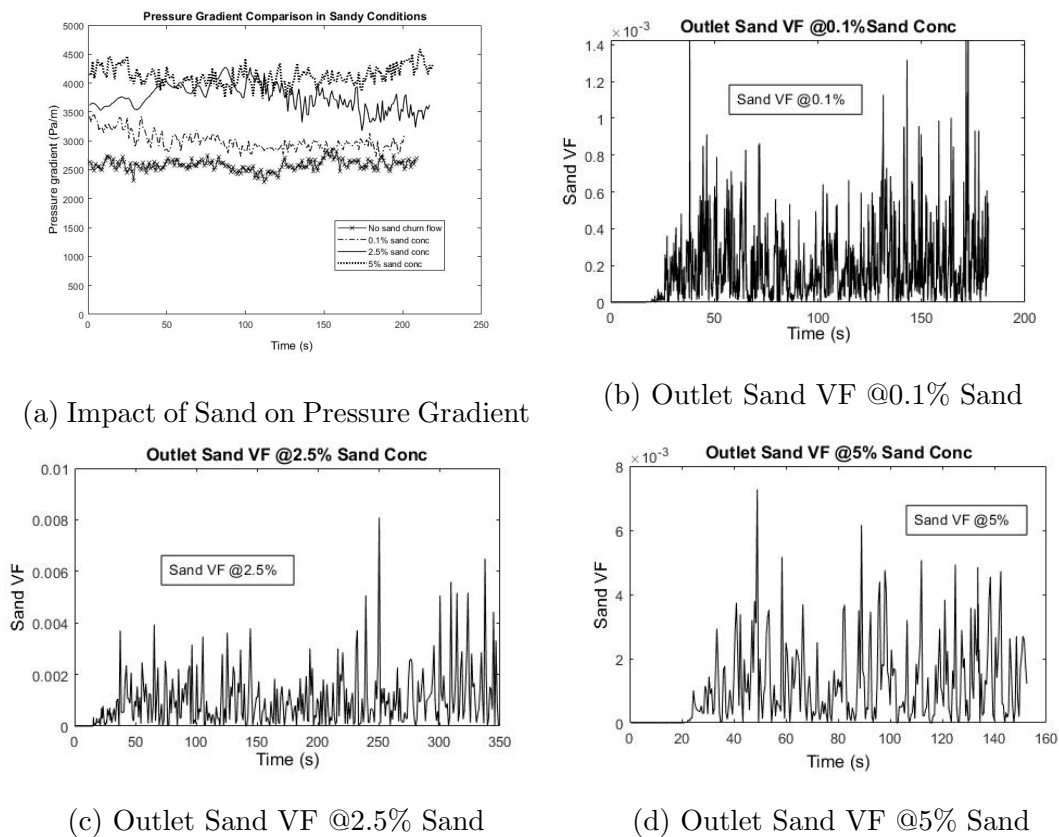
Figure 6.15: Sand VF Comparison and Impact on Pressure Gradient

the previous. This shows that the sand transported to the surface is not a representation of the sand produced into the pipe at the bottom. The difference in this value amount to the accumulation of the sand that is deposited at the bottom of the pipe. Hence, sand measurement at the platform is not a representation of sand production into the wellbore. At any point in time, the total sand produced does not get to the surface to be measured. Thus, surface sand measurement at the wellhead or manifold do not represent the actual sand produced.

6.7.2.4   Hydrodynamic Parameter Profiles

Parameter profiles of gas-liquid-solid flow was examined in this section. Radial profile of the phase velocities were taken at 5m height while the turbulent kinetic energy was profiled across the axial length to determine where the energy drop is most noticed. The three cases of sand volume fractions were analysed for phase velocity and the turbulent kinetic energy as depicted in Figure 6.16.

139

As shown on the plots of Figure 6.16a for 5% sand volume fraction, the sand flow is trailing the gas and liquid at a lower velocity even though the initial velocity of gas and sand particles were the same. This is due to the density difference and overall mass flux of the solid particles. It can also be seen that the velocity at the walls for all the phases is zero which represent a no-slip wall boundary conditions. Similarly, Figure 6.16b for 2.5% inlet sand volume fraction and Figure 6.16c for 0.1% inlet sand volume fraction also showed same profile. From the time averaged representation shown in the velocity plots, it can be concluded that the higher the inlet sand volume fraction, the higher the difference between the fluid and solid particle velocities. There tends to be an overlap between the fluid and particles at lower sand volume fraction. It can also be noticed in the velocity plots that both the gas and liquid are flowing at approximately same velocity. This is likely due to the mixture turbulence model chosen for the numerical scheme as the dispersed turbulence model was unable to produce converged solution. The reason for this is not immediately known.

Lastly, Figure 6.16d shows the axial turbulent kinetic energy profile for the three cases of sand volume fractions investigated in this research. The graphical plot profile were taken at fully developed flow and at established sand profile. The plot shows that the TKE was less at the bed where the sand settles, which is in the 5% sand concentration up to about 2.5m. The fluctuations in the profiles indicate fluidisation and movement of sand within the pipe.

6.7.2.5 Instantaneous Mass Flux Computation of Sand Flow

The mass flux calculation was carried out using ANSYS Fluent computational algorithm to determine sand transportation in vertical pipe. Table 6.4 shows the result for different sand regime. The tabulated results indicate that even as low as 0.1% sand concentration, not all produced sand is transported to the outlet of the pipe. The imbalance represents the quantity of sand particles that remained fluidised and floating within the pipe bore. The qualitative analysis earlier shown also confirmed the presence of this fluidised sand particles in the pipe bore. Further analysis of the results shows that up to 80-97% of the produced sand particle can actually be left in the pipe and never transported to the surface. The higher the percentage of sand produced, the higher the imbalance. For this

(a) Velocities @ 5% sand vf

(b) Velocities @ 2.5% sand vf

(c) Velocities @ 0.1% sand vf

(d) TKE @ Various Sand VF
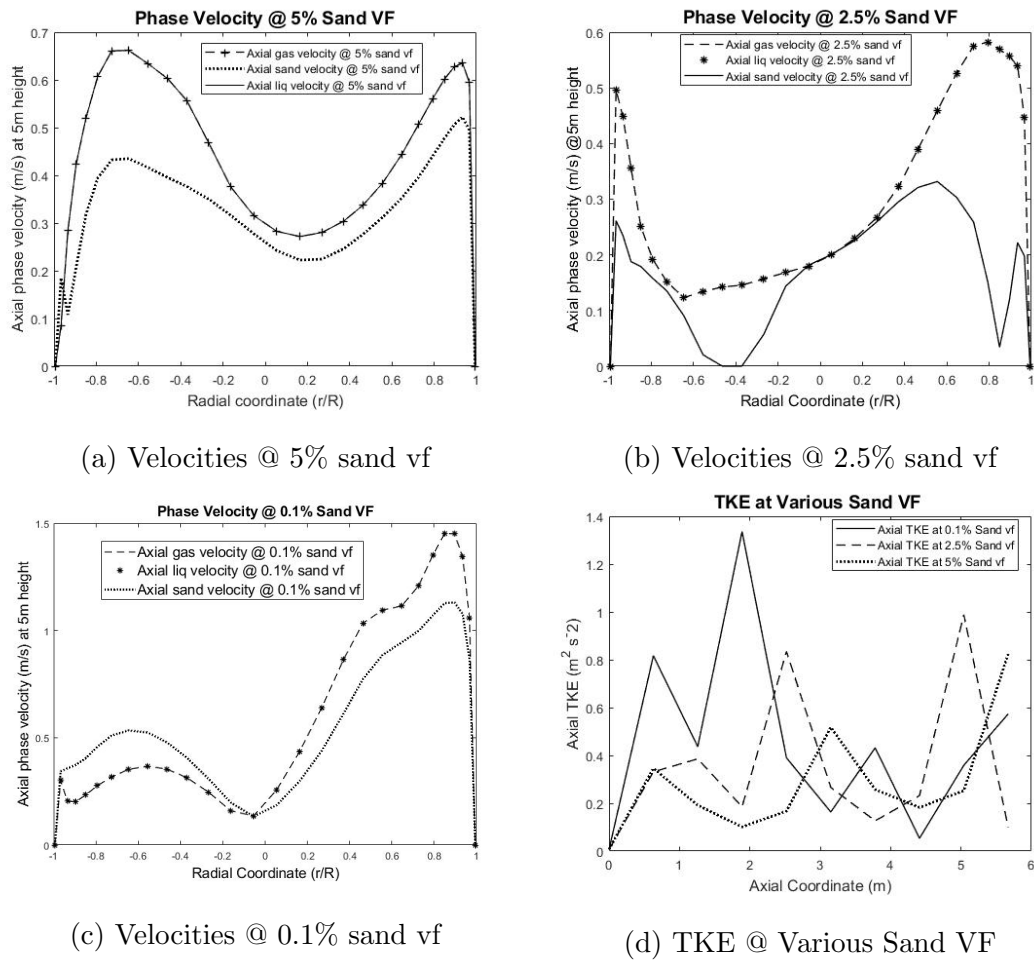
Figure 6.16: Parametric Study of Phase Transport in Sand Regime

reason, wellbore fill is a common occurrence in the oil and gas wells but, more common in gas wells due to density difference.

6.8 Summary of Three-Phase Gas-Liquid-Solid Flow

The validated two-phase flow model was extended to investigate three-phase gas-liquid-solid flow according to closure model C of Figure 4.1. The results have been qualitatively and quantitatively analysed. The impact of sand particles in a three-phase gas-liquid-solid flows has been discussed. In this investigation, it is discovered that:

1. Sand particles affect the bubbles agglomeration and hence small bubbles cannot coalesce to form large Taylor-like bubbles in comparison to the sand-free gas-liquid flows.

Table 6.4: Instantaneous Mass Flux Result

Mass Flux (kg/s)	0.1% sand	2.5% sand	5% sand
Inlet	0.01460	0.36508	0.73016
Outlet	0.00874	0.00902	0.03016
Imbalance	0.00586	0.35600	0.70000
% deposited	40	97	96

2. Not all sand particles produced into the pipe are transported to the surface. Higher percentage of the sand produced are left behind at the pipe bottom. When this happens, there would be substantial pressure loss and eventual fluid flow reduction which would lead to blockade due to sand deposition.

3. It is shown qualitatively and quantitatively that sand deposition and settling is proportional to the inlet sand volume fraction at constant fluid velocity. Therefore, increasing the velocity alone without taking into consideration the inflow volume fraction is not enough to determine transportation of sand particles in vertical pipes.

4. Pressure drop continues to increase as the mass flux of sand produced increases up to and above packing limit.

5. The inclusion of a third phase to any two phase flow system will lead to the reduction of the overall fluid flow as some spaces must be taken over by the new phase added.

<div align="right">Chapter 7</div>

CONCLUSIONS AND RECOMMENDATIONS

The first aim of this research was to perform a two-phase gas-liquid CFD simulations to capture the hydrodynamic properties in the flow field. The Eulerian multi-fluid VOF in conjunction with the Interfacial Area Transport Equations (IATE) model was used for this purpose in this research. The fluid system are Nitrogen gas and liquid Naphtha while the geometry is a large diameter vertical pipe. The model was validated against the published experimental results and data set of Omebere-Iyari et al. (2007b). The comparisons were appropriately matched. This validated CFD model was later used to compute the hydrodynamics of three-phase gas-liquid-solid flows in a large diameter vertical pipe with the introduction of the solid phase. The impact of the solid phase on the flow field was analysed. In addition, the transportation phenomenon in different sand regimes were also investigated and analysed. The outcome of these investigation are novel and is such that allows better understanding of the phenomenological dynamism in three-phase gas-liquid-sand churn flow regime. It is believe that churn flow is the most difficult flow regime to understand but, it is one of the most prevalent flow pattern in oil & gas production system. The churn flow pattern is chosen for the final investigation of the dynamic variables in a three-phase flow system. The conclusion of this research work are made of two parts which are gas-liquid and gas-liquid-solid flows. These are presented in subsections 7.1.1 & 7.1.2. Finally, the recommendations from the results and findings of this work is presented in section 7.2.

7.1 Conclusions

7.1.1 Gas-Liquid Flows

1. A CFD model that is capable of simulating all flow regimes spectrum found in larger diameter pipe was developed and validated against published experimental data. This CFD framework couples the Euler-Euler model with Interfacial Area Concentration formulation of Hibiki and Ishii (2000). The model was able to predict all flow regime spectrum from bubbly to annular flow without prior knowledge of the flow pattern.

2. Further analysis of the flow hydrodynamics in two-phase flow was carried out. The result of the simulation indicates that larger Taylor bubbles found in small diameter pipe flow were not seen in large diameter pipe flow simulation. Hence it can be deduced that such large bubbles do not exist in two-phase flow in larger diameter pipe. This finding is similar to the previously published findings by notable researchers.

3. For small diameter pipe, many experimental and theoretical studies has been carried out and the database is extensive. But data set for large diameter pipe flow is still very sparse. This study has added to the database of large diameter vertical pipe. Studies by Ohnuki and Akimoto (2000) and Schlegel et al. (2009) which are most referenced in literature for larger diameter pipe experiments did not cover regimes with higher gas superficial velocities above churn flow. The transition from churn to annular flow has not been exhaustively studied. Only few researchers such as Spedding et al. (1998), Omebere-Iyari et al. (2007b) and others had acknowledged that semi annular flow exist between churn and annular flow. In this investigation, the semi annular flow is proven to be an important desirable flow pattern in fluid flow system. The semi-annular flow has the highest kinetic energy required for fluid/solid particle movement in vertical fluid flow system. This investigation also shows that the difference in the turbulence kinetic energy between the churn and semi annular flow suggests that the later could be categorised differently as a separate

flow pattern.

4. The structure of bubbles have been described as either spherical small group-1 bubbles and irregular shaped group-2 bubbles. But the surface instability and the resultant shape has been exclusively described relative to the fluid properties. CFD post contour visualisation algorithm was used to plot the internal symmetry of the pipe. The results show that round shaped and cap bubbles were not obtained in this investigation. This is likely due to the surface instability effect on the Taylor bubbles as a result of the low surface tension at the liquid-gas interface. Surface tension is important in determining the interfacial or geometrical morphology of the gas-liquid interface which determines the shape of the bubbles.

5. The drift flux model for two-phase flow has been used in the study of multi-phase flow for decades. However, there has been various modification by different researchers and the variations between small and large diameter pipe has been considered. The models proposed by most researchers did not account for different flow patterns. In this research work, there is a clear distinction between the different flow patterns and the in-situ drift velocities have different magnitudes. Hence each flow pattern should have its own distribution parameter figure.

6. Two approaches used for the generation of flow regime map are by experimental and theoretical means. In this research, CFD computational model has been used to compute full multi-phase two phase flow hydrodynamics. A CFD flow regime map for two-phase flow was generated and compared with the experimental flow regime map of Omebere-Iyari et al. (2007b). The comparison was appropriate. The flow regime map and its contour plot were also compared with the flow regime map of Ali and Yeung (2014a) and the flow regime map of Schlegel et al. (2009). The flow regime maps of these two authors did not include flow patterns beyond churn flow. However, reasonable comparison was noticed within common regimes but, there are differences in the terminology and description given to some of the flow morphology observed.

Thus, a CFD investigation of two phase flow has been developed, validated and further

analysis of the flow hydrodynamics has been carried out successfully.

7.1.2 Gas-Liquid-Solid Flows

1. A CFD simulation of three-phase gas-liquid-solid flow was performed and the results were analysed according to established methods. Appropriate closure laws and interfacial interaction forces were considered to achieve a stabilised flow in the Euler-Euler model validated for two-phase flow. The KTGF was used to compute the solid pressure and stress up to packing limit when the sand deposition in the pipe increases at fully stabilised flow. Three of sand flow cases were considered at 0.1%, 2.5% and 5% sand concentration. The introduction of the sand was through the center gas inlet while the liquid was introduced through the annular circumference.

2. Qualitative analysis of the gas and solid flows were performed for the three cases. The result shows that the gas bubbles coalescence can be distorted with the presence of sand particles hence the larger gas bubbles that were comparatively found in the two-phase flow counterpart were smaller and more dispersed in the three-phase flow. On the other hand, sand transportation and deposition were dependent on the sand concentration presence in the flow scheme.

3. Further quantitative analysis of the fluids volume fractions indicate that the fluids flow is reduced when the third-phase is introduced to the flow scheme. The volume fractions of other fluids were reduced at the onset of sand flow. Thus, the introduction of sand into the flow scheme could impact the fluid flow in different ways.

4. Sand or solid phase presence in the flow field increases the pressure gradient. It was shown in the analysis that the pressure gradient increases as the sand volume fraction is increased. This leads to pressure energy reduction and eventual fluid flow reduction. Besides, the sand transported to the surface of the pipe is not a measure of the total sand produce into the pipe. This research shows that as high as 70-90% of sand produced can eventually be left at the bottom of the pipe. It can be deduced from the findings that sand rate measurement at the surface or at

wellhead does not represent the total sand produced into the well. More of the sand particles produced are left at the bottom of the process pipe during production.

7.2   Recommendations

This research was carried out within the limitation of available computing resources and availability of validating experimental data set. While the outcome of the investigation are novel, there is still work to be done in the future with respect to large diameter vertical pipe flow analysis in two and three phase flow scheme. The following recommendations are hereby put forward for consideration.

1. The two-phase flow simulation analysis indicated that the semi annular flow regime produces the highest turbulent kinetic energy required for fluid and particle transportation. Therefore, it is recommended that production and pipeline engineers should design pipe to enable this flow pattern in the production and pipeline system for efficient transportation of fluids to the surface.

2. This investigation only considered the mono-dispersed sand transport in a typical churn flow regime. While other flow patterns were not investigated in this research, it is recommended that semi-annular and annular flow transport should be investigated for further validation of sand transport and deposition at high gas and liquid superficial velocities.

3. In this research, the interfacial area concentration equation was used to simulate the bubble coalescence and breakup of gas particles. While this is an approximate method for the purpose, and though yielded expected result, it is worthwhile to consider modelling this with population balance model (PBM). The PBM can model different particle size distribution of the bubble particles effectively. The PBM is a more computational intensive model but, it could produce more accurate outcome.

4. As the kinetic energy required to transport fluid from the well is highest at the semi-annular regime, it is recommended that production operators should aim to achieve semi-annular flow scheme through gas lift system. This option will be useful

in the optimisation of productions from low and deep wells where lifting is a setback to productions.

5. This research only considered mono-dispersed sand particles in the flow field. It is recommended that poly-dispersed particles be simulated using the Euler-Euler-Euler framework with PBM method to study the effect of sand particle sizes in the hydrodynamics of three-phase gas-liquid-solid flows in large diameter vertical pipe system. The PBM is effective in simulating different sand particle sizes in the flow system.

Finally, two-phase and three-phase flow simulations have been successfully modelled, simulated and the results were analysed qualitatively and quantitatively. Appropriate conclusions and recommendation have been put forward for consideration and implementation by engineers and field operators in the energy industries. Further investigation and validation of the findings of this research work is not excluded.

REFERENCES

Adeyanju, O., Oyekunle, L. et al. (2012), Hydrodynamics of sand-oil-gas multiphase flow in a near vertical well, *in* 'Nigeria Annual International Conference and Exhibition', Society of Petroleum Engineers.

Ahmadi, G. and Ma, D. (1990), 'A thermodynamical formulation for dispersed multiphase turbulent flows—1: Basic theory', *International Journal of Multiphase Flow* **16**(2), 323–340.

Ali Farman, S. and Yeung, H. (2015), 'Experimental study of two-phase air–water flow in large-diameter vertical pipes', *Chemical Engineering Communications* **202**(6), 823–842.

Ali, S. F. and Yeung, H. (2014*a*), 'Two-phase flow patterns in large diameter vertical pipes', *Asia-Pacific Journal of Chemical Engineering* **9**(1), 105–116.

Ali, S. F. and Yeung, H. (2014*b*), 'Two-phase flow patterns in large diameter vertical pipes', *Asia-Pacific Journal of Chemical Engineering* **9**(1), 105–116.

Anglart, H. and Nylund, O. (1996), 'Cfd application to prediction of void distribution in two-phase bubbly flows in rod bundles', *Nuclear Engineering and Design* **163**(1-2), 81–98.

Ansari, A., Sylvester, N., Shoham, O., Brill, J. et al. (1990), A comprehensive mechanistic model for upward two-phase flow in wellbores, *in* 'SPE Annual Technical Conference and Exhibition', Society of Petroleum Engineers, Texas, USA.

Asheim, H. et al. (1986), 'Mona, an accurate two-phase well flow model based on phase slippage', *SPE Production Engineering* **1**(03), 221–230.

Aziz, K., Govier, G. W. et al. (1972), 'Pressure drop in wells producing oil and gas', *Journal of Canadian Petroleum Technology* **11**(03).

REFERENCES

Barnea, D. (1987), 'A unified model for predicting flow-pattern transitions for the whole range of pipe inclinations', *International Journal of Multiphase Flow* **13**(1), 1–12.

Barnea, D. and Shemer, L. (1989), 'Void fraction measurements in vertical slug flow: applications to slug characteristics and transition', *International Journal of Multiphase Flow* **15**(4), 495–504.

Barnea, D., Shoham, O., Taitel, Y. and Dukler, A. (1985), 'Gas-liquid flow in inclined tubes: flow pattern transitions for upward flow', *Chemical Engineering Science* **40**(1), 131–136.

Baxendell, P., Thomas, R. et al. (1961), 'The calculation of pressure gradients in high-rate flowing wells', *Journal of Petroleum Technology* **13**(10), 1–023.

Beggs, D. H., Brill, J. P. et al. (1973), 'A study of two-phase flow in inclined pipes', *Journal of Petroleum technology* **25**(05), 607–617.

Bhagwat, S. M. and Ghajar, A. J. (2014), 'A flow pattern independent drift flux model based void fraction correlation for a wide range of gas–liquid two phase flow', *International Journal of Multiphase Flow* **59**, 186–205.

Brauner, N. and Barnea, D. (1986), 'Slug/churn transition in upward gas-liquid flow', *Chemical engineering science* **41**(1), 159–163.

Brill, J. P. et al. (1987), 'Multiphase flow in wells', *Journal of petroleum technology* **39**(01), 15–21.

Brill, J. P. et al. (2010), 'Modeling multiphase flow in pipes', *The Way Ahead* **6**(02), 16–17.

Cai, S., Toral, H., Qiu, J. and Archer, J. S. (1994), 'Neural network based objective flow regime identification in air-water two phase flow', *The Canadian Journal of Chemical Engineering* **72**(3), 440–445.

Chen, X. and Brill, J. (1997), 'Slug to churn transition in upward vertical two-phase flow', *Chemical Engineering Science* **52**(23), 4269–4272.

REFERENCES

Cheng, H., Hills, J. and Azzorpardi, B. (1998), 'A study of the bubble-to-slug transition in vertical gas-liquid flow in columns of different diameter', *International Journal of Multiphase Flow* **24**(3), 431–452.

Cheng, L., Ribatski, G. and Thome, J. R. (2008), 'Two-phase flow patterns and flow-pattern maps: fundamentals and applications', *Applied Mechanics Reviews* **61**(5), 050802.

Cheung, S. C., Yeoh, G. and Tu, J. (2007), 'On the modelling of population balance in isothermal vertical bubbly flows—average bubble number density approach', *Chemical Engineering and Processing: Process Intensification* **46**(8), 742–756.

Chierici, G., Ciucci, G., Sclocchi, G. et al. (1974), 'Two-phase vertical flow in oil wells-prediction of pressure drop', *Journal of Petroleum Technology* **26**(08), 927–938.

Costigan, G. and Whalley, P. (1997), 'Slug flow regime identification from dynamic void fraction measurements in vertical air-water flows', *International Journal of Multiphase Flow* **23**(2), 263–282.

Cox, S. A., Sutton, R. P., Blasingame, T. A. et al. (2006), Errors introduced by multiphase flow correlations on production analysis, *in* 'SPE Annual Technical Conference and Exhibition', Society of Petroleum Engineers.

Da Riva, E. and Del Col, D. (2009), 'Numerical simulation of churn flow in a vertical pipe', *Chemical Engineering Science* **64**(17), 3753–3765.

Dai, Y., Dakshinammorthy, D., Agrawal, M. et al. (2013), Cfd modeling of bubbly, slug and annular flow regimes in vertical pipelines, *in* 'Offshore Technology Conference', Offshore Technology Conference.

Ding, J. and Gidaspow, D. (1990), 'A bubbling fluidization model using kinetic theory of granular flow', *AIChE journal* **36**(4), 523–538.

Drew, D. and Lahey, R. (1993), 'In particulate two-phase flow', *ButterworthL Heinemann, Boston* **509**(0), 566.

REFERENCES

Duns Jr, H., Ros, N. et al. (1963), Vertical flow of gas and liquid mixtures in wells, *in* '6th world petroleum congress', World Petroleum Congress.

Fancher Jr, G. H., Brown, K. E. et al. (1962), Prediction of pressure gradients for multiphase flow in tubing, *in* 'Fall Meeting of the Society of Petroleum Engineers of AIME', Society of Petroleum Engineers.

Ferziger, J. H., Perić, M. and Street, R. L. (2002), *Computational methods for fluid dynamics*, Vol. 3, Springer.

Fluent, A. (2018), 'Ansys fluent theory guide', *ANSYS Inc., USA* **15317**.

Frank, T., Shi, J. and Burns, A. D. (2004), Validation of eulerian multiphase flow models for nuclear safety application, *in* 'Proceeding of the Third International Symposium on Two-Phase Modelling and Experimentation, Pisa, Italy', Citeseer.

Gharaibah, E., Read, A., Scheuerer, G. et al. (2015), Overview of cfd multiphase flow simulation tools for subsea oil and gas system design, optimization and operation, *in* 'OTC Brasil', Offshore Technology Conference.

Ghosh, S., Pratihar, D., Maiti, B. and Das, P. (2012), 'Identification of flow regimes using conductivity probe signals and neural networks for counter-current gas–liquid two-phase flow', *Chemical Engineering Science* **84**, 417–436.

Gidaspow, D., Bezburuah, R. and Ding, J. (1991), Hydrodynamics of circulating fluidized beds: kinetic theory approach, Technical report, Illinois Inst. of Tech., Chicago, IL (United States). Dept. of Chemical Engineering.

Gilbert, W. et al. (1954), Flowing and gas-lift well performance, *in* 'Drilling and production practice', American Petroleum Institute.

Grace, J., Crift, R. and Weber, M. (1978), 'Bubbles, drops, and particles'.

Griffith, P. and Wallis, G. B. (1961), 'Two-phase slug flow', *Journal of Heat Transfer* **83**(3), 307–318.

REFERENCES

Hagedorn, A. R., Brown, K. E. et al. (1965), 'Experimental study of pressure gradients occurring during continuous two-phase flow in small-diameter vertical conduits', *Journal of Petroleum Technology* **17**(04), 475–484.

Hamidipour, M., Chen, J. and Larachi, F. (2012), 'Cfd study on hydrodynamics in three-phase fluidized beds—application of turbulence models and experimental validation', *Chemical engineering science* **78**, 167–180.

Harmathy, T. Z. (1960), 'Velocity of large drops and bubbles in media of infinite or restricted extent', *AIChE Journal* **6**(2), 281–288.

Hasan, A. R., Kabir, C. S. et al. (1988), 'A study of multiphase flow behavior in vertical wells', *SPE Production Engineering* **3**(02), 263–272.

Hewitt, G. F. (2012), 'Churn and wispy annular flow regimes in vertical gas–liquid flows', *Energy & Fuels* **26**(7), 4067–4077.

Hewitt, G. F. and Roberts, D. (1969), Studies of two-phase flow patterns by simultaneous x-ray and flast photography, Technical report, Atomic Energy Research Establishment, Harwell, England (United Kingdom).

Hewitt, G. and Jayanti, S. (1993), 'To churn or not to churn', *International Journal of Multiphase Flow* **19**(3), 527–529.

Hibiki, T. and Ishii, M. (2000), 'One-group interfacial area transport of bubbly flows in vertical round tubes', *International Journal of Heat and Mass Transfer* **43**(15), 2711–2726.

Hibiki, T. and Ishii, M. (2003), 'One-dimensional drift-flux model and constitutive equations for relative motion between phases in various two-phase flow regimes', *International Journal of Heat and Mass Transfer* **46**(25), 4935–4948.

Hills, J. (1976), 'The operation of a bubble column at high throughputs: I. gas holdup measurements', *The Chemical Engineering Journal* **12**(2), 89–99.

Hinze, J. (1955), 'Fundamentals of the hydrodynamic mechanism of splitting in dispersion processes', *AIChE Journal* **1**(3), 289–295.

REFERENCES

Huilin, L. and Gidaspow, D. (2003), 'Hydrodynamics of binary fluidization in a riser: Cfd simulation using two granular temperatures', *Chemical Engineering Science* **58**(16), 3777–3792.

Ishii, M. (1977), One-dimensional drift-flux model and constitutive equations for relative motion between phases in various two-phase flow regimes, Technical report, Argonne National Lab., Ill.(USA).

Ishii, M. and Hibiki, T. (2011), *Thermo-fluid dynamics of two-phase flow*, Springer Science & Business Media.

Ishii, M. and Kim, S. (2001), 'Micro four-sensor probe measurement of interfacial area transport for bubbly flow in round pipes', *Nuclear engineering and design* **205**(1-2), 123–131.

Jayanti, S. and Hewitt, G. (1992a), 'Prediction of the slug-to-churn flow transition in vertical two-phase flow', *International Journal of Multiphase Flow* **18**(6), 847–860.

Jayanti, S. and Hewitt, G. (1992b), 'Prediction of the slug-to-churn flow transition in vertical two-phase flow', *International Journal of Multiphase Flow* **18**(6), 847–860.

Johansen, S., Mo, S., Meese, E., Oliveira, J., Reyes, J., Carneiro, J. et al. (2015), Cfd simulations of multiphase flows containing large scale interfaces and dispersed phases with selected production technology applications, *in* 'OTC Brasil', Offshore Technology Conference.

Jones Jr, O. C. and Zuber, N. (1975a), 'The interrelation between void fraction fluctuations and flow patterns in two-phase flow', *International Journal of Multiphase Flow* **2**(3), 273–306.

Jones Jr, O. C. and Zuber, N. (1975b), 'The interrelation between void fraction fluctuations and flow patterns in two-phase flow', *International Journal of Multiphase Flow* **2**(3), 273–306.

Kaji, R. and Azzopardi, B. (2010), 'The effect of pipe diameter on the structure

of gas/liquid flow in vertical pipes', *International Journal of Multiphase Flow* **36**(4), 303–313.

Kataoka, I. and Ishii, M. (1987), 'Drift flux model for large diameter pipe and new correlation for pool void fraction', *International Journal of Heat and Mass Transfer* **30**(9), 1927–1939.

Khrabry, A. I., Smirnov, E. M. and Zaytsev, D. K. (2011), Solving the convective transport equation with several high-resolution finite volume schemes: Test computations, *in* 'Computational Fluid Dynamics 2010', Springer, pp. 535–540.

Kim, S., Ishii, M., Kong, R. and Wang, G. (2021), 'Progress in two-phase flow modeling: Interfacial area transport', *Nuclear Engineering and Design* **373**, 111019.

Kocamustafaogullari, G. and Ishii, M. (1995), 'Foundation of the interfacial area transport equation and its closure relations', *International Journal of Heat and Mass Transfer* **38**(3), 481–493.

Kolev, N. I. and Kolev, N. (2005), *Multiphase flow dynamics*, Vol. 1, Springer.

Krepper, E., Lucas, D. and Prasser, H.-M. (2005), 'On the modelling of bubbly flow in vertical pipes', *Nuclear engineering and design* **235**(5), 597–611.

Kundu, P. K. and Cohen, I. M. (2002), 'Fluid mechanics'.

Lakehal, D. (2013), 'Advanced simulation of transient multiphase flow & flow assurance in the oil & gas industry', *The Canadian Journal of Chemical Engineering* **91**(7), 1201–1214.

Launder, B. E. and Spalding, D. B. (1972), 'Lectures in mathematical models of turbulence', *Academic press* .

Lawson, J. D., Brill, J. P. et al. (1974), 'A statistical evaluation of methods used to predict pressure losses for multiphase flow in vertical oilwell tubing', *Journal of Petroleum Technology* **26**(08), 903–914.

Lee, J. Y., Ishii, M. and Kim, N. S. (2008), 'Instantaneous and objective flow regime identification method for the vertical upward and downward co-current two-phase flow', *International Journal of Heat and Mass Transfer* **51**(13-14), 3442–3459.

Legendre, D. and Magnaudet, J. (1998), 'The lift force on a spherical bubble in a viscous linear shear flow', *Journal of Fluid Mechanics* **368**, 81–126.

Li, W. and Zhong, W. (2015), 'Cfd simulation of hydrodynamics of gas–liquid–solid three-phase bubble column', *Powder Technology* **286**, 766–788.

Liu, Y., Cui, J. and Li, W. (2011), 'A two-phase, two-component model for vertical upward gas–liquid annular flow', *International Journal of Heat and Fluid Flow* **32**(4), 796–804.

Lowe, D. and Rezkallah, K. (1999), 'Flow regime identification in microgravity two-phase flows using void fraction signals', *International Journal of Multiphase Flow* **25**(3), 433–457.

Lun, C., Savage, S. B., Jeffrey, D. and Chepurniy, N. (1984), 'Kinetic theories for granular flow: inelastic particles in couette flow and slightly inelastic particles in a general flowfield', *Journal of fluid mechanics* **140**, 223–256.

Matsui, G. (1984), 'Identification of flow regimes in vertical gas-liquid two-phase flow using differential pressure fluctuations', *International journal of multiphase flow* **10**(6), 711–719.

McQuillan, K. and Whalley, P. (1985), 'Flow patterns in vertical two-phase flow', *International Journal of Multiphase Flow* **11**(2), 161–175.

Mi, Y., Ishii, M. and Tsoukalas, L. (1998), 'Vertical two-phase flow identification using advanced instrumentation and neural networks', *Nuclear Engineering and Design* **184**(2-3), 409–420.

Mi, Y., Ishii, M. and Tsoukalas, L. (2001), 'Flow regime identification methodology with neural networks and two-phase flow models', *Nuclear engineering and design* **204**(1-3), 87–100.

REFERENCES

Mishima, K. and Ishii, M. (1984), 'Flow regime transition criteria for upward two-phase flow in vertical tubes', *International Journal of Heat and Mass Transfer* **27**(5), 723–737.

Montoya, G., Lucas, D., Baglietto, E. and Liao, Y. (2016), 'A review on mechanisms and models for the churn-turbulent flow regime', *Chemical Engineering Science* **141**, 86–103.

Moraga, F., Bonetto, F. and Lahey, R. (1999), 'Lateral forces on spheres in turbulent uniform shear flow', *International Journal of Multiphase Flow* **25**(6), 1321–1372.

Morsi, S. and Alexander, A. (1972), 'An investigation of particle trajectories in two-phase flow systems', *Journal of Fluid mechanics* **55**(2), 193–208.

Nicklin, D. and Davidson, J. (1962), The onset of instability in two-phase slug flow, *in* 'Proceedings of the Symposium on Two-phase Fluid'.

Oddie, G., Shi, H., Durlofsky, L., Aziz, K., Pfeffer, B. and Holmes, J. (2003), 'Experimental study of two and three phase flows in large diameter inclined pipes', *International Journal of Multiphase Flow* **29**(4), 527–558.

Ogawa, S., Umemura, A. and Oshima, N. (1980), 'On the equations of fully fluidized granular materials', *Zeitschrift für angewandte Mathematik und Physik ZAMP* **31**(4), 483–493.

Ohnuki, A. and Akimoto, H. (1996), 'An experimental study on developing air-water two-phase flow along a large vertical pipe: effect of air injection method', *International journal of multiphase flow* **22**(6), 1143–1154.

Ohnuki, A. and Akimoto, H. (2000), 'Experimental study on transition of flow pattern and phase distribution in upward air–water two-phase flow along a large vertical pipe', *International journal of multiphase flow* **26**(3), 367–386.

Olufemi, A., Olalekan, O. and Eyituoyo, B. (2011), 'An improved version of calculating the pressure traverse in multiphase flow vertical pipe', *Petroleum & Coal* **53**(1), 56–64.

Omebere-Iyari, N., Azzopardi, B. and Ladam, Y. (2007*a*), Gas/liquid flow in a large riser: effect of upstream configurations, *in* '13th International Conference on Multiphase Production Technology', BHR Group.

Omebere-Iyari, N., Azzopardi, B. and Ladam, Y. (2007*b*), 'Two-phase flow patterns in large diameter vertical pipes at high pressures', *AIChE journal* **53**(10), 2493–2504.

Omebere-Iyari, N., Azzopardi, B., Lucas, D., Beyer, M. and Prasser, H. (2008), 'The characteristics of gas/liquid flow in large risers at high pressures', *International journal of multiphase flow* **34**(5), 461–476.

Orkiszewski, J. et al. (1967), 'Predicting two-phase pressure drops in vertical pipe', *Journal of Petroleum Technology* **19**(06), 829–838.

Ozon, P., Ferschneider, G., Chwetzoff, A. et al. (1987), A new multiphase flow model predicts pressure and temperature profiles in wells, *in* 'Offshore Europe', Society of Petroleum Engineers.

Pagan, E., Williams, W., Kam, S., Waltrich, P. et al. (2016*a*), Modeling vertical flows in churn and annular flow regimes in small-and large-diameter pipes, *in* '10th North American Conference on Multiphase Technology', BHR Group.

Pagan, E., Williams, W., Kam, S., Waltrich, P. et al. (2016*b*), Modeling vertical flows in churn and annular flow regimes in small-and large-diameter pipes, *in* '10th North American Conference on Multiphase Technology', BHR Group.

Pang, M., Wei, J. and Yu, B. (2010), 'Numerical study of bubbly upflows in a vertical channel using the euler–lagrange two-way model', *Chemical Engineering Science* **65**(23), 6215–6228.

Panneerselvam, R., Savithri, S. and Surender, G. (2009), 'Cfd simulation of hydrodynamics of gas–liquid–solid fluidised bed reactor', *Chemical Engineering Science* **64**(6), 1119–1135.

Parsi, M., Vieira, R., Torres, C., Kesana, N., McLaury, B., Shirazi, S., Hampel, U. and Schleicher, E. (2014), Characterizing slug/churn flow using wire mesh sensor, *in* 'ASME 2014 4th Joint US-European Fluids Engineering Division Summer Meeting collocated with the ASME 2014 12th International Conference on Nanochannels, Microchannels, and Minichannels', American Society of Mechanical Engineers, pp. V01DT32A009–V01DT32A009.

Pietrzak, M., Płaczek, M. and Witczak, S. (2017), 'Upward flow of air-oil-water mixture in vertical pipe', *Experimental Thermal and Fluid Science* **81**, 175–186.

Poettman, F. H., Carpenter, P. G. et al. (1952), The multiphase flow of gas, oil, and water through vertical flow strings with application to the design of gas-lift installations, *in* 'Drilling and Production Practice', American Petroleum Institute.

Pope, S. B. (2001), 'Turbulent flows'.

Pourtousi, M., Sahu, J. and Ganesan, P. (2014), 'Effect of interfacial forces and turbulence models on predicting flow pattern inside the bubble column', *Chemical Engineering and Processing: Process Intensification* **75**, 38–47.

Prasser, H., Beyer, M., Carl, H., Manera, A., Pietruske, H. and Schütz, P. (2007), 'Experiments on upwards gas/liquid flow in vertical pipes', *FZD-482 TOPFLOW Wissenschaftlich-Technische Berichte* .

Prasser, H.-M., Beyer, M., Böttger, A., Carl, H., Lucas, D., Schaffrath, A., Schütz, P., Weiss, F.-P. and Zschau, J. (2005), 'Influence of the pipe diameter on the structure of the gas-liquid interface in a vertical two-phase pipe flow', *Nuclear Technology* **152**(1), 3–22.

Ramkrishna, D. and Mahoney, A. W. (2002), 'Population balance modeling. promise for the future', *Chemical Engineering Science* **57**(4), 595–606.

Rampure, M. R., Buwa, V. V. and Ranade, V. V. (2003), 'Modelling of gas-liquid/gas-liquid-solid flows in bubble columns: Experiments and cfd simulations', *The Canadian Journal of Chemical Engineering* **81**(3-4), 692–706.

Rocha, M. d. S. and Simões-Moreira, J. (2008), 'Void fraction measurement and signal analysis from multiple-electrode impedance sensors', *Heat transfer engineering* **29**(11), 924–935.

Ruiz, R., Brito, A., Marquez, J. G. et al. (2014), Evaluation of multiphase flow models to predict pressure gradient in vertical pipes with highly viscous liquids, *in* 'SPE Latin America and Caribbean Petroleum Engineering Conference', Society of Petroleum Engineers.

REFERENCES

Rzehak, R. and Krepper, E. (2013), 'Closure models for turbulent bubbly flows: A cfd study', *Nuclear Engineering and Design* **265**, 701–711.

Saffman, P. (1965), 'The lift on a small sphere in a slow shear flow', *Journal of fluid mechanics* **22**(02), 385–400.

Schaeffer, D. G. (1987), 'Instability in the evolution equations describing incompressible granular flow', *Journal of differential equations* **66**(1), 19–50.

Schetz, J. A. and Fuhs, A. E. (1999), *Fundamentals of fluid mechanics*, John Wiley & Sons.

Schiller, L. and Naumann, Z. (1935), 'Z. ver. deutsch. ing'.

Schlegel, J., Hibiki, T. and Ishii, M. (2010), 'Development of a comprehensive set of drift-flux constitutive models for pipes of various hydraulic diameters', *Progress in Nuclear Energy* **52**(7), 666–677.

Schlegel, J. P. and Hibiki, T. (2015), 'A correlation for interfacial area concentration in high void fraction flows in large diameter channels', *Chemical Engineering Science* **131**, 172–186.

Schlegel, J. P., Hibiki, T. and Ishii, M. (2016), 'Characteristics of two-phase flows in large diameter channels', *Nuclear Engineering and Design* **310**, 544–551.

Schlegel, J. P., Miwa, S., Chen, S., Hibiki, T. and Ishii, M. (2012), 'Experimental study of two-phase flow structure in large diameter pipes', *Experimental Thermal and Fluid Science* **41**, 12–22.

Schlegel, J. P., Sawant, P., Paranjape, S., Ozar, B., Hibiki, T. and Ishii, M. (2009), 'Void fraction and flow regime in adiabatic upward two-phase flow in large diameter vertical pipes', *Nuclear Engineering and Design* **239**(12), 2864–2874.

Sharma, S. L., Ishii, M., Hibiki, T., Schlegel, J. P., Liu, Y. and Buchanan Jr, J. R. (2019), 'Beyond bubbly two-phase flow investigation using a cfd three-field two-fluid model', *International Journal of Multiphase Flow* **113**, 1–15.

Shen, X., Mishima, K. and Nakamura, H. (2004), Two-phase phase distribution effect on drift–flux parameters in a vertical large diameter pipe, *in* 'Proc. 3rd Int. Symp. on Two-Phase Flow Modeling and Experimentation', pp. 22–24.

Shen, X., Mishima, K. and Nakamura, H. (2005), 'Two-phase phase distribution in a vertical large diameter pipe', *International Journal of Heat and Mass Transfer* **48**(1), 211–225.

Shen, X., Schlegel, J. P., Chen, S., Rassame, S., Griffiths, M. J., Hibiki, T. and Ishii, M. (2014), Flow characteristics and void fraction prediction in large diameter pipes, *in* 'Frontiers and Progress in Multiphase Flow I', Springer, pp. 55–103.

Shi, H., Holmes, J., Diaz, L., Durlofsky, L. J., Aziz, K. et al. (2005), 'Drift-flux parameters for three-phase steady-state flow in wellbores', *SPE Journal* **10**(02), 130–137.

Shoham, O. (2005), *Mechanistic Modeling of Gas/liquid Two-phase Flow in Pipes*, Spe.

Simonin, O. and Viollet, P. (1990), 'Modelling of turbulent two-phase jets loaded with discrete particles', *Phenomena in multiphase flows* pp. 259–269.

Smith, T., Schlegel, J. P., Hibiki, T. and Ishii, M. (2012), 'Two-phase flow structure in large diameter pipes', *International Journal of Heat and Fluid Flow* **33**(1), 156–167.

Sokolichin, A., Eigenberger, G., Lapin, A. and Lübert, A. (1997), 'Dynamic numerical simulation of gas-liquid two-phase flows euler/euler versus euler/lagrange', *Chemical engineering science* **52**(4), 611–626.

Song, C. H., No, H. C. and Chung, M. K. (1995), 'Investigation of bubble flow developments and its transition based on the instability of void fraction waves', *International journal of multiphase flow* **21**(3), 381–404.

Spedding, P., Woods, G., Raghunathan, R. and Watterson, J. (1998), 'Vertical two-phase flow: part ii: experimental semi-annular flow and hold-up', *Chemical Engineering Research and Design* **76**(5), 620–627.

Sun, X., Smith, T., Kim, S., Ishii, M. and Uhle, J. (2003), 'Interfacial structure of air-water two-phase flow in a relatively large pipe', *Experiments in fluids* **34**(2), 206–219.

Syamlal, M., Rogers, W. and OBrien, T. J. (1993*a*), Mfix documentation theory guide, Technical report, USDOE Morgantown Energy Technology Center, WV (United States).

Syamlal, M., Rogers, W. and O'Brien, T. J. (1993*b*), 'Mfix documentation: Theory guide', *National Energy Technology Laboratory, Department of Energy, Technical Note DOE/METC-95/1013 and NTIS/DE95000031* .

Taha, T. and Cui, Z. (2006), 'Cfd modelling of slug flow in vertical tubes', *Chemical Engineering Science* **61**(2), 676–687.

Taitel, Y. (1986), 'Stability of severe slugging', *International journal of multiphase flow* **12**(2), 203–217.

Taitel, Y., Bornea, D. and Dukler, A. (1980), 'Modelling flow pattern transitions for steady upward gas-liquid flow in vertical tubes', *AIChE Journal* **26**(3), 345–354.

Tebowei, R. (2016), 'Computational fluid dynamics (cfd) modelling of critical velocity for sand transport flow regimes in multiphase pipe bends.', *PhD Thesis* .

Tomiyama, A. (1998), 'Struggle with computational bubble dynamics', *Multiphase Science and Technology* **10**(4), 369–405.

Tomiyama, A. and Takamasa, T. (1999), Three-dimensional gas–liquid two-phase bubbly flow in a c-shaped tube, *in* 'Proceedings of the 1999 NURETH-9 Conference', pp. 1–17.

Tomiyama, A., Zun, I., Sou, A. and Sakaguchi, T. (1993), 'Numerical analysis of bubble motion with the VOF method', *Nuclear Engineering and Design* **141**(1-2), 69–82.

Troshko, A. and Hassan, Y. (2001), 'A two-equation turbulence model of turbulent bubbly flows', *International Journal of Multiphase Flow* **27**(11), 1965–2000.

Tutu, N. K. (1982), 'Pressure fluctuations and flow pattern recognition in vertical two phase gas-liquid flows', *International Journal of Multiphase Flow* **8**(4), 443–447.

Van Hout, R., Shemer, L. and Barnea, D. (1992), 'Spatial distribution of void fraction within a liquid slug and some other related slug parameters', *International Journal of Multiphase Flow* **18**(6), 831–845.

REFERENCES

Van Wachem, B. and Almstedt, A.-E. (2003), 'Methods for multiphase computational fluid dynamics', *Chemical Engineering Journal* **96**(1-3), 81–98.

Versluys, J. et al. (1930), 'Mathematical development of the theory of flowing oil wells', *Transactions of the AIME* **86**(01), 192–208.

Versteeg, H. K. and Malalasekera, W. (2007), *An introduction to computational fluid dynamics: the finite volume method*, Pearson education.

Wacławczyk, T. and Koronowicz, T. (2008), 'Comparison of cicsam and hric high-resolution schemes for interface capturing', *Journal of theoretical and applied mechanics* **46**, 325–345.

Wallis, G. B. (1969), 'One-dimensional two-phase flow'.

Wilcox, D. C. et al. (1998), *Turbulence modeling for CFD*, Vol. 2, DCW industries La Canada, CA.

Wu, B., Firouzi, M., Mitchell, T., Rufford, T. E., Leonardi, C. and Towler, B. (2017), 'A critical review of flow maps for gas-liquid flows in vertical pipes and annuli', *Chemical Engineering Journal* **326**, 350–377.

Wu, P.-K., Tseng, L.-K. and Faeth, G. (1992), 'Primary breakup in gas/liquid mixing layers for turbulent liquids', *Atomization and Sprays* **2**(3).

Wu, Q., Kim, S., Ishii, M. and Beus, S. (1998), 'One-group interfacial area transport in vertical bubbly flow', *International Journal of Heat and Mass Transfer* **41**(8-9), 1103–1112.

Xu, L., Xia, Z., Guo, X. and Chen, C. (2014), 'Application of population balance model in the simulation of slurry bubble column', *Industrial & Engineering Chemistry Research* **53**(12), 4922–4930.

Yamoah, S., Martínez-Cuenca, R., Monrós, G., Chiva, S. and Macián-Juan, R. (2015), 'Numerical investigation of models for drag, lift, wall lubrication and turbulent dispersion forces for the simulation of gas–liquid two-phase flow', *Chemical Engineering Research and Design* **98**, 17–35.

Yao, W. and Morel, C. (2004), 'Volumetric interfacial area prediction in upward bubbly two-phase flow', *International Journal of Heat and Mass Transfer* **47**(2), 307–328.

Yeoh, G. and Tu, J. (2004), 'Population balance modelling for bubbly flows with heat and mass transfer', *Chemical engineering science* **59**(15), 3125–3139.

Yeoh, G. and Tu, J. (2005), 'Thermal-hydrodynamic modeling of bubbly flows with heat and mass transfer', *AIChE journal* **51**(1), 8–27.

Yunus, A. C. (2010), *Fluid Mechanics: Fundamentals And Applications (Si Units).*, Tata McGraw Hill Education Private Limited.

Zhang, D. and Vanderheyden, W. (2002), 'The effects of mesoscale structures on the disperse two-phase flows and their closures for dilute suspensions', *Int. J. Multiph. Flow* **28**, 805–822.

Zuber, N. and Findlay, J. (1965), 'Average volumetric concentration in two-phase flow systems', *Journal of heat transfer* **87**(4), 453–468.